In Quest of Devising Tools of Probing Cosmology and Gravity using Galaxy Clusters

by

Vitali Halenka

A dissertation submitted in partial fulfillment
of the requirements for the degree of
Doctor of Philosophy
(Physics)
in The University of Michigan
2019

Doctoral Committee:

Associate Professor Christopher J. Miller, Chair
Professor August E. Evrard
Professor Dragan Huterer
Professor Mario Mateo

Vitali Halenka

vithal@umich.edu

ORCID iD: 0000-0001-7483-0945

ACKNOWLEDGEMENTS

I would like to thank my adviser Christopher Miller for the countless advises and support during my graduate school. A little over three years has passed since our first conversation, starting from which a big potential in our work together was realized. It was an incredible journey full of invaluable lessons. I thank my collaborators Alejo Stark and Wentao Luo for the fruitful discussions and productive collaboration. I want to thank physics department facilities for providing great office space and comfortable working environment. Last but not least, I would like to thank my friends and family.

TABLE OF CONTENTS

LIST OF FIGURES

Figure

LIST OF TABLES

Table

ABSTRACT

Galaxy clusters are the biggest gravitationally bound objects in the Universe with various properties which allow us to test gravitational and cosmological models. One such way of testing theoretical models is by directly measuring density profiles of different matter components (i.e. weak lensing and X-ray provide information about baryon and dark matter mass distributions). A recent version of Emergent Gravity (EG) (*Verlinde*, 2017) predicts a specific connection between baryonic and dark matter which can be directly tested using galaxy clusters. By using a sample of 23 galaxy clusters, we find that the EG predictions (based on no dark matter) are acceptable fits only near the virial radius. In the cores and in the outskirts, the mass profile shape differences allow us to rule out EG at $> 5\sigma$. However, when we account for systematic uncertainties in the observed weak-lensing and X-ray profiles, we conclude that we cannot formally rule our EG as an alternative to dark matter on the cluster scale and that we require better constraints on the weak-lensing and gas mass profile shapes in the region $0.3 \leq r/r_{200} \leq 1$. We also show that EG itself allows flexibility in its predictions, which can allow for good agreement between the observations and the predictions. The second way, which is address in current manuscript, to probe theory is based on escape velocity profiles of galaxy clusters, which has been shown to be a competitive probe of cosmology in an accelerating universe. Projection onto the sky is a dominant systematic uncertainty for statistical inference, since line-of-sight projection of the galaxy positions and velocities can suppress the underlying 3D escape-velocity edge. In this work, we develop the approach based on idea of creating N galaxies with positions and velocities on Keplerian orbits, given richness and the line-of-sight ve-

locity dispersion. We then compare the analytical escape edge to those from N-body simulations. We show that given high enough sampling, the 3D escape velocity edge is in fact observable without systematic bias or suppression with $< 1\%$ accuracy over the range $0 \leq r/r_{200} \leq 1$. We show that the approach model the amount of the edge suppression (Z_v) with $\sim 2\%$ accuracy and $\sim 5\%$ precision for massive ($> 10^{14} M_{\odot}$) systems over the range $0.4 \leq r/r_{200} \leq 1$. We show that the numerically modeled suppression is independent of velocity anisotropy over the range $-2.5 \leq \beta \leq 0.5$. Finally, we show that suppression is mass and cosmology independent and can be successfully modeled by inverse power-law $Z_v = 1 + (N_0/N)^{\lambda}$ with best-fit parameters $N_0 = 14.205, \lambda = 0.467$ (the bottom error bar line: $N_0 = 3.213, \lambda = 0.392$, the top error bar line: $N_0 = 35.822, \lambda = 0.454$). We conclude that the 3D cluster escape velocity profile can be inferred from projected phase-space data without knowledge of cosmology or the use of simulations. We applied this suppression function to test cosmology and our preliminary results produced a tight constraints on cosmological parameters. By statistically analyzing the set of 38 galaxy clusters, we were able to constraint $\Omega_{m,0} = 0.325^{+0.014(stat)+0.003(sys)}_{-0.021(stat)-0.001(sys)}$ and the Hubble constant $h_0 = 0.733^{+0.007(stat)+0.035(sys)}_{-0.006(stat)-0.029(sys)}$ in the framework of flat universe and fixed equation of state of dark energy ($w = -1$). The systematic error budget includes $\pm 5\%$ uncertainties on the weak lensing mass calibration and $\pm 5\%$ uncertainties in the density model differences between the NFW and the Einasto functions. This result is in a good agreement with other probes, while in general favor CMB observations of $\Omega_{m,0}$ by *Planck Collaboration et al.* (2018) and h_0 by using Cepheids (*Riess et al.*, 2019).

CHAPTER I

Introduction

The general perception of escaping gravitational potential of a massive body such our Earth or stars, which is familiar to everyone either from physics textbooks or from sci-fi movies, is that one needs to have high enough velocity, so he or she has kinetic energy higher than potential energy due to the Earth's or star's gravitational field. At the same time, it was shown that Universe expands with acceleration (*Riess et al.*, 1998), which can be interpreted as existence of effective gravitational pull. This effect helps any body to escape massive objects or, in other words, reduces the speed one needs to have to leave the state of gravitational bounding with the massive object. However, this effect is negligible in a vicinity of planets and stars and starts to be noticeable only at very large, *megaparsecs* (Mpc), scale. Additionally, if at some point the gravitational potential created by the massive objects falls under some upper limit, it starts to be smaller than gravitational pull due to acceleration expansion and any object above this threshold is not gravitationally bound to the massive object. This mechanism effectively creates a limit of how big massive objects can be. In general, the most massive and the biggest gravitationally bound objects of the Universe are called galaxy clusters. As we have just seen, these objects exhibit the highest effect from cosmological background on their gravitational field out of all massive objects in the Universe and that makes galaxy clusters to be one of the

most sensitive tools of probing cosmology by analyzing their gravitational field and potential.

1.1 Basic cosmology

The whole cosmology is based upon Einstein's equation,

$$R_{\mu\nu} - \frac{1}{2} g_{\mu\nu} R = 8\pi G T_{\mu\nu}. \tag{1.1}$$

The second basic idea is introduction of homogeneous and isotropic metric of our Universe (FRLW metric),

$$g_{\mu\nu} dx^\mu dx^\nu = -dt^2 + a^2(t)\Big[\frac{dr^2}{1-kr^2} + r^2(d\theta^2 + \sin^2\theta d\phi^2)\Big], \tag{1.2}$$

where k is the curvature parameter: 0 - flat, -1 - open and $+1$ - closed Universes correspondingly. $a(t)$ is a scalar factor - function of time which describes relative expansion of the Universe. This function could be rewritten in terms of the redshift: $z = \frac{a_0}{a(t)} + 1$, where a_0 is the present value of the scale factor.

The conservation of the energy-momentum tensor ($T_{\mu\nu} = (\rho + p)u_\mu u_\nu - p g_{\mu\nu}$) in FRLW metric implies

$$\dot{\rho} + 3H(\rho + p) = 0, \tag{1.3}$$

where we introduced Hubble parameter $H = \frac{\dot{a}}{a}$, ρ energy density and p isotropic pressure.

Using (1.2), Einstein's equation (1.1) implies the first and the second Friedmann equations

$$H^2 = \frac{8\pi G}{3}\rho - \frac{k}{a^2} \tag{1.4}$$

$$\frac{\ddot{a}}{a} = -\frac{4\pi G}{3}(\rho + 3p) \tag{1.5}$$

The total energy-density of the Universe consists of contributions from ordinary baryonic matter ρ_b, dark matter (DM) ρ_{DM}, radiation ρ_r, curvature ρ_k and dark energy (DE) ρ_Λ

$$\rho_{tot} = \rho_b + \rho_{DM} + \rho_r + \rho_k + \rho_\Lambda. \tag{1.6}$$

Each of these contribution are the functions of the scale factor $a(t)$ and all of them could be written in common form

$$\rho \propto a^{-3(1+\omega)}, \tag{1.7}$$

where $\omega = \frac{p}{\rho}$ is the equation of state (EOS) and it is different for different types of energy-densities, i.e. $\frac{1}{3}$ for radiation, 0 for baryonic matter and DM, $-\frac{1}{3}$ for curvature and -1 for DE. We can rewrite the total energy-density (1.6)

$$\rho_{tot} = (\rho_{b,0} + \rho_{DM,0})\Big(\frac{a_0}{a}\Big)^3 + \rho_{r,0}\Big(\frac{a_0}{a}\Big)^4 + \rho_{k,0}\Big(\frac{a_0}{a}\Big)^2 + \rho_{\Lambda,0}, \tag{1.8}$$

where energy-densities with the subscript 0 correspond to the present values of energy-densities.

The final step is to introduce density parameters

$$\Omega_i = \frac{\rho_{i,0}}{\rho_{c,0}}, \tag{1.9}$$

where $\rho_{c,0} = \frac{3H_0^2}{8\pi G} \sim (10^{-12}\text{Gev})^4$ is critical energy-density today - the total energy-density of the flat Universe, i.e. $\sum\limits_i \Omega_i = 1$ if $\Omega_k \approx 0$.

Throughout current work we treat curvature energy-density of being equal to zero $\Omega_k \approx 0$ and we neglect radiation contribution as it is small at late stages of the evolution of the Universe (*Planck Collaboration et al.*, 2018), which allows us to

express first Friedmann equation through energy-density parameters

$$H^2(z) = H_0^2\Big(\Omega_m(1+z)^3 + (1-\Omega_m)(1+z)^{-3(1+\omega)}\Big), \tag{1.10}$$

where $\omega = -1$ for the rest of the work unless explicitly mentioned otherwise and $\Omega_\Lambda = 1 - \Omega_m$, where the total energy-density of matter is $\Omega_m = \Omega_b + \Omega_{DM}$.

Throughout this work, we extensively use quantities R_{200} and M_{200} which are the radius and the mass of the clusters at the point when the density drops to $200\rho_{c,z}$, where $\rho_{c,z} = \frac{3H^2(z)}{8\pi G}$ is the critical density of the universe at redshift z. The connection between R_{200} and M_{200} is by definition the following: $M_{200} = \frac{4\pi}{3}(200\rho_{c,z})R_{200}^3$.

1.2 Cosmological motivation

Dark matter (DM) and dark energy (DE) are the two main component of the energy-density of the Universe which together account for $\sim 95\%$ of it (*Planck Collaboration et al.*, 2018).

The first ever introduction of DE was done by Einstein in 1917. After his discovery of General Relativity (GR), Einstein introduced cosmological constant Λ in order to have static Universe. Unfortunately for him, in 1928 E. Hubble discovered that our Universe is expanding and Einstein admitted that Λ was the biggest blinder of his lifetime. However, *Riess et al.* (1998) and *Perlmutter et al.* (1999) discovered using Supernova Type Ia (SN Ia) that our Universe expands with acceleration and one of possible explanations of this phenomena could be introduction of cosmological constant into Einstein's equation. In general, the source of this acceleration is called DE and the existence of this phenomena was also proved using Cosmic Microwave Background (CMB) and Baryon Acoustic Oscillations (BAO). A broad introduction to these cosmological probes is presented in the next section 1.3.

Jacobus Kapteyn was the first one who by using stellar velocities suggested ex-

istence of dark matter (DM) (*Kapteyn*, 1922). The first to observe signs of dark matter on a galaxy clusters scale was Fritz Zwicky (*Zwicky*, 1933), who introduced it to explain deviations from virial theorem in observations of Coma cluster. Later works only increased confidence of DM existence as it was needed to explain the deviation from Newtonian dynamics for galaxy rotation curves (*Rubin and Ford*, 1970). In addition to requiring need for DE, cosmological probes SNIa, CMB and BAO all support DM existence as well as observations of individual systems such as Bullet Cluster (*Clowe et al.*, 2006) and analyzing gravitational lensing of galaxy clusters (*Natarajan et al.*, 2017).

As we can see, there are plenty of probes which imply that DE and DM exist and expands with acceleration (*Riess et al.*, 1998; *Perlmutter et al.*, 1999; *Amanullah et al.*, 2010; *Betoule et al.*, 2014b; *Ade et al.*, 2016; *Planck Collaboration et al.*, 2018; *Hinshaw et al.*, 2013). However, we still do not know the origin of dark matter and dark energy, neither the theory of these phenomena. Dark matter observations mostly favor particle models such weakly interacting massive particles (WIMPs) and axions (we refer reader to *Freese* (2017) for a review of this topic), while DE require some extension to general relativity either simple explanation based on the idea of cosmological constant or non-trivial theories, which involve additional tensor fields or change Einstein's equation adding terms with infinite number of derivatives or extra dimensions (for a briefly review of a few possible theoretical ways to explain DE see section 1.4). Emergent Gravity (EG) is one of the recent theories that tightly connects both of these "dark" components (*Verlinde*, 2011, 2017). This theory is quite unique as it does not modify Einstein's equation directly, but rather describes gravity as an emergent phenomenon from a spacetime quantum entanglement. EG predicts direct connection between DM and baryonic matter

$$M_b(r) = \frac{6}{a_0 r} \int_0^r \frac{G M_{DM}^2(r')}{r'^2} dr', \tag{1.11}$$

where $M(r)$ in the total mass inside some radius r, index $_b$ corresponds to baryons and index $_{DM}$ to dark matter. For a broader introduction to the EG model see chapter II.

1.3 Cosmological probes of dark energy

This work focuses primarily on the utilization of galaxy clusters to test gravitational and cosmological models. In addition to galaxy clusters, there are various type of cosmological evidences of DE and DM. In this section we are going to discuss main of them, which are SN Ia, CMB and BAO. Moreover, we will briefly talk about pie picture of the Universe.

1.3.1 Standard candles - SN Ia

The first ever evidence of DE was discovered in works *Riess et al.* (1998); *Perlmutter et al.* (1999). They discovered that the luminosity of the SN Ia are lower than it should be if the Universe would be decelerating and would not have contribution from DE.

The SN Ia are standard candles, i.e. objects which have the same luminosity. Nowadays, there are various projects which have discovered hundreds of SN Ia. The biggest samples are Union 2 (*Amanullah et al.*, 2010) with 557 SNIa by the Supernova Cosmology Project and JLA sample *Betoule et al.* (2014b) with 740 SN Ia by SDSS-II and SNLS collaborations.

In order to use SN Ia, their distance modulus μ is employed on assumption that supernova with identical color, lightcurve shape and galactic environment have on average the same intrinsic luminosity for all redshifts

$$\mu = m - M + \alpha X - \gamma Y, \tag{1.12}$$

where m is the observed peak magnitude in the restframe B band, X describes the time stretching of light curves, Y describes the color at the maximum brightness and M, α, γ are nuisance parameters in the distance estimates.

From theoretical point of view the luminosity distance is related to the difference of apparent and absolute magnitude M

$$\mu = m - M = 5\log_{10}(d_L) + 25, \tag{1.13}$$

where d_L is measured luminosity distance in megaparsecs

$$d_L(z) = \frac{1}{H_0}(1+z)r(z), \tag{1.14}$$

where the "comoving transverse distance" in the flat Universe is

$$r(z) = \int_0^z \frac{H_0}{H(z')}dz'. \tag{1.15}$$

It could be seen that our Universe expands with acceleration and we can find different cosmological parameters comparing sample data from *Amanullah et al.* (2010); *Betoule et al.* (2014b) and theoretical models from equations (1.12), (1.13). This comparison is represented on the fig. 1.1.

1.3.2 CMB

The CMB tells us how the Universe looked like at the redshift of decoupling $z_d \approx 1100$. By looking at the CMB we can see the history of the Universe from the decoupling epoch to the present one. Before the decoupling, baryons were strongly coupled to the photons. However, after recombination baryons started to be free from scattering with photons and they stayed at a fixed radius. This radius is called sound horizon and it determines the first acoustic peak of the CMB (see fig. (1.2)). The

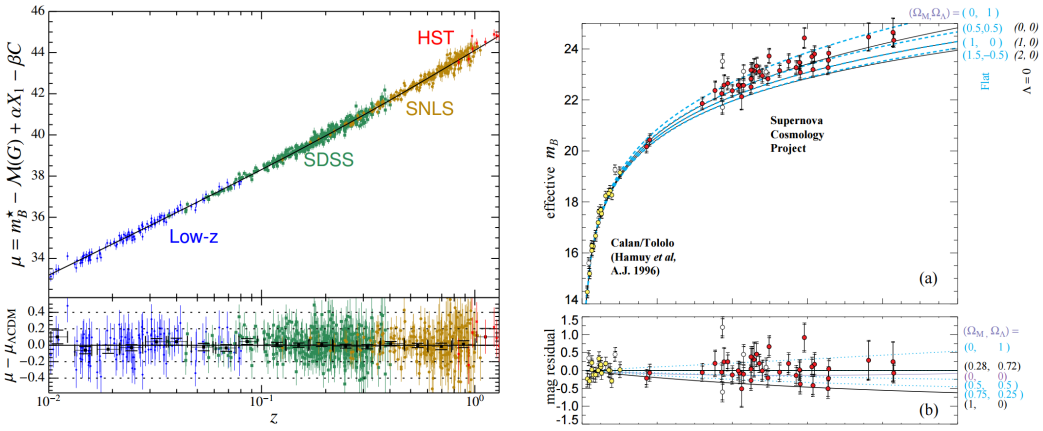

Figure 1.1: *Top left*: the distance modulus redshift relation of the best-fit ΛCDM cosmology for a fixed $H_0 = 70$ km $s^{-1}Mpc^{-1}$ is shown as the black line. *Bottom left*: Residuals from the best fit ΛCDM cosmology as a function of redshift. *Top and bottom right*: best-fit ΛCDM cosmology and their residuals. Various lines correspond to different sets of parameters. (Left figure is adopted from *Betoule et al.* (2014b), right figure from *Perlmutter et al.* (1999)).

sound horizon can be observed directly. This radius is predicted from the theory and it could be served as a standard ruler by measuring the angular scale of the acoustic peak.

The best measurement of the angular power spectrum of the CMB (fig. (1.2)) was done by WMAP collaboration (*Hinshaw et al.*, 2013) and Plank collaboration (*Planck Collaboration et al.*, 2018).

Moreover, we can use Sunyaev-Zel'dovich (SZ) effect as the standard ruler (*Cooray et al.*, 2001). The SZ effect is the effect of distortion CMB photons by scattering with the high energy electrons from galaxy clusters.

1.3.3 BAO

As was discussed in the previous subsection, the baryons stayed at the sound horizon distance after decoupling while DM stayed at the center of overdensity. They attracted matter and later this led to the formation of galaxies. From this argument, we expect that some galaxies should be separated by the specific distance, i.e. the

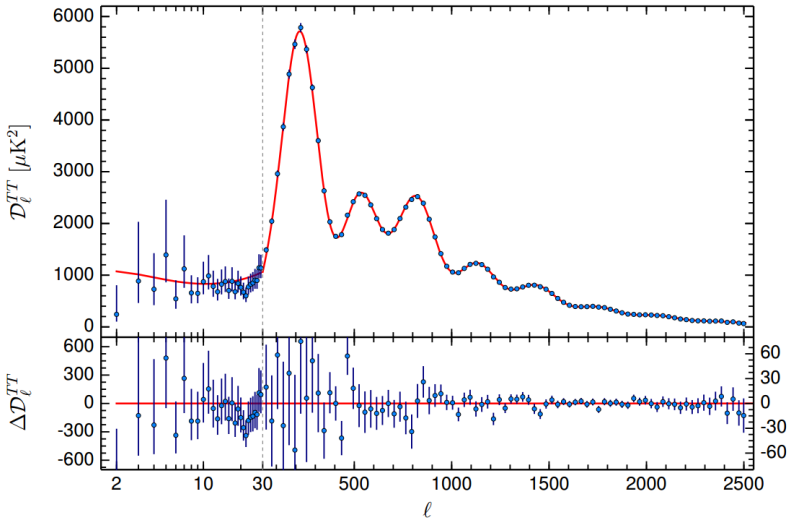

Figure 1.2: The Plank 2015 [*Ade et al.* (2016)] temperature power spectrum. The best-fit base ΛCDM theoretical spectrum fitted to the Plank TT+lowP likelihood is plotted in the upper panel. Residuals with respect to this model are shown in the lower panel. The error bars show $\pm 1\sigma$ uncertainties (The figure is adopted from Plank 2015 [*Ade et al.* (2016)]).

sound horizon. This phenomena is called BAO signal.

In order to measure the sound horizon, it is enough to measure only three-dimensional position of each galaxy. Since one do not need to care about galaxy images and magnitudes, it is one of the rare methods of probing DE which is clear from astronomical uncertainties.

By using two-point correlation function, we can analyze the data. The main data set is provided by the Sloan Digital Sky Survey (SDSS) (*Blanton et al.*, 2017). We can actually observe the bump in the observations of BAO. Both CMB and BAO imply that the sound horizon is approximately 150 Mpc.

1.3.4 Pie chart of the Universe and the equation of state (EOS)

In addition to three discussed above, there are other types of observational probes such as galaxy clusters, weak gravitational lensing, gamma ray bursts (GRB), etc. All of them imply the fact that our Universe expands with acceleration. Moreover,

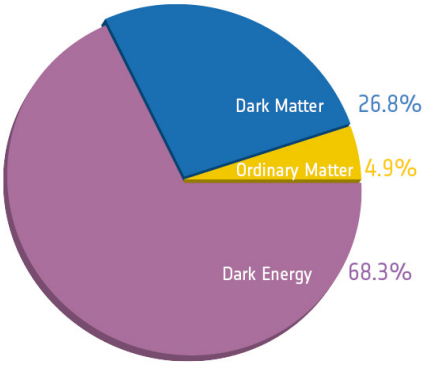

Figure 1.3: Pie chart shows relative energy-densities of different constituents of the Universe.

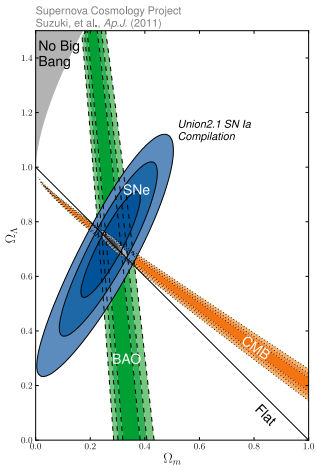

Figure 1.4: Ω_m - Ω_Λ fit of CMB, BAO and Union 2 with the contours constraint 68.3%, 95.5% and 99.7% regions. (The figure is adopted from *Amanullah et al.* (2010).)

DE component plays a huge role since its contribution to the total energy-density is the biggest. Energy-density of DE is more than twice higher than the matter one and orders of magnitude higher than energy-densities of radiation and curvature. One of the most informative ways to show this fact is to use pie chart of the Universe (1.3).

More accurate results of the combine fit (*Ade et al.*, 2016) gives following numbers: $\Omega_\Lambda = 0.6911 \pm 0.0062$, $\Omega_m = 0.3089 \pm 0.0062$ and $H_0 = 67.74 \pm 0.46$ km/s/Mpc. The results of fitting Union 2 (*Amanullah et al.*, 2010) together with CMB and BAO presented at the fig. 1.4.

One of the main characteristics of DE is its EOS

$$\omega = \frac{p}{\rho} \tag{1.16}$$

We can expand EOS

$$\omega = \omega_0 + (1 - a)\omega_a \tag{1.17}$$

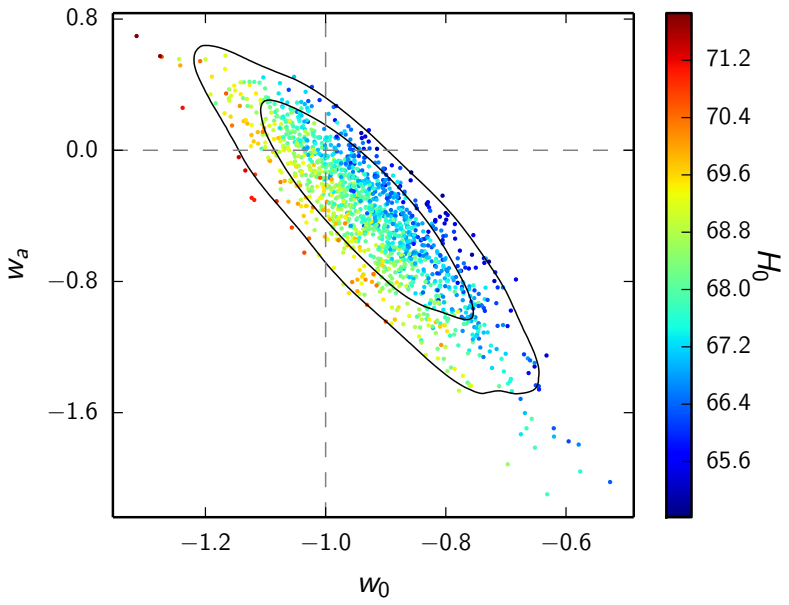

Figure 1.5: Samples from the distribution of the DE parameters ω_0 and ω_a using Plank TT+lowP+BAO+JLA data, colour-coded by the value of the Hubble parameter H_0. Contours show the corresponding 68% and 95% limits. (The figure is adopted from *Ade et al.* (2016)).

where ω_0 corresponds to the present value of the EOS of DE, a is a scale factor and ω_a is a first term in expansion in time of the EOS.

EOS of cosmological constant (CC) is equal to $\omega_0 = -1$ and $\omega_a = 0$. The observational results of Plank 2015 (*Ade et al.*, 2016) are presented on the fig. (1.5). These results favor $\omega_0 \approx -1$ and $\omega_a \approx 0$.

Frieman et al. (2008) provides a broad review on the topic of DE probes.

1.4 Alternative theories of gravity

1.4.1 Cosmological constant

The most easy way to explain DE is to use cosmological constant (CC), the same idea which was originally proposed by Einstein. CC modifies Einstein's equation (1.1)

$$R_{\mu\nu} - \frac{1}{2} g_{\mu\nu} R = 8\pi G T_{\mu\nu} + \Lambda g_{\mu\nu}. \tag{1.18}$$

Therefore, the Friedmann equations (1.4), (1.5) must be also changed by introduction new constant term $\frac{\Lambda}{3}$ on the right hand side of both equations.

In general, CC is not only the easiest possible model of DE, but also it fits observational data very nicely (fig. 1.1 and 1.4). Unfortunately, there are two problems related to CC: fine-tuning problem (1.4.1.1) and coincidence problem (1.4.1.2).

1.4.1.1 Cosmological constant problem

CC problem arises from treating CC as a vacuum energy. We can look at our quantum vacuum field as a set of harmonic oscillators and each of them has the lowest energy state. Since we trust our theory only up to some scale which is characterized by the Plank mass M_{pl}, we could get energy-density of the vacuum

$$\rho_\Lambda \sim \hbar M_{pl}^4 \sim 10^{72} \text{ Gev}^4. \tag{1.19}$$

From observations we know that

$$\rho_{c,obs} \sim 10^{-48} \text{ Gev}^4. \tag{1.20}$$

Comparing these two number we see that theoretical value is approximately 120 orders of magnitude higher than the observational one. There were introduced many different explanation to this problem, but non of them is successful enough to clearly explain this discrepancy.

1.4.1.2 Cosmic coincidence problem

If we look at the evolution of energy-densities of different constituents (fig. (1.6) we can see that energy-densities of matter and DE are approximately equal today. Moreover, the transmission to acceleration expansion (the intersection of red and blue dashed lines) happens in a very narrow region and it happened almost "yesterday"

on a cosmological scale.

In order to find the exact redshift of transmission from deceleration to acceleration, we write Friedmann equation (1.4) through the density parameters (1.9)

$$\Big(\frac{\dot{a}}{a}\Big)^2 = \frac{8\pi G}{3}\rho_{c,0}\Big(\Omega_{m,0}\Big(\frac{a_0}{a}\Big)^3 + \Omega_{\Lambda,0}\Big(\frac{a_0}{a}\Big)^{3(1+\omega)}\Big). \tag{1.21}$$

Imposing $\omega \to -1$, we find 2nd Friedmann equation (1.5) in this case

$$\ddot{a} = \frac{4\pi G}{3}\rho_{c,0}a\Big(2\Omega_{\Lambda,0} - \Omega_{m,0}\Big(\frac{a_0}{a}\Big)^3\Big). \tag{1.22}$$

Applying latest observational results of Plank 2015 [*Ade et al.* (2016)], we get redshift of this transmission

$$z_{acc} = \Big(\frac{2\Omega_{\Lambda,0}}{\Omega_{m,0}}\Big)^{1/3} - 1 \approx 0.63. \tag{1.23}$$

Cosmic coincidence problem states following question: why are we so lucky to life in such a unique time? Why did the transition to acceleration is happening now and not at different time? This is a problem, because if this transition happened earlier there would be not enough time to form the gravitationally bounded objects like stars, galaxies etc.

Of course, one of the possible solutions could be anthropic principle. However, a lot of scientists do not accept this idea as a valid explanation. For review about cosmological constant we refer reader to *Carroll* (2001); *Martin* (2012).

1.4.2 Modified gravity theories

The Lovelock's theorem (*Lovelock*, 1971; *Lovelock*, 1972) claims that there are limited amount of ways to modify Einstein's equation (1.1). We are going to present the list of the types of these modifications with the examples of the theories.

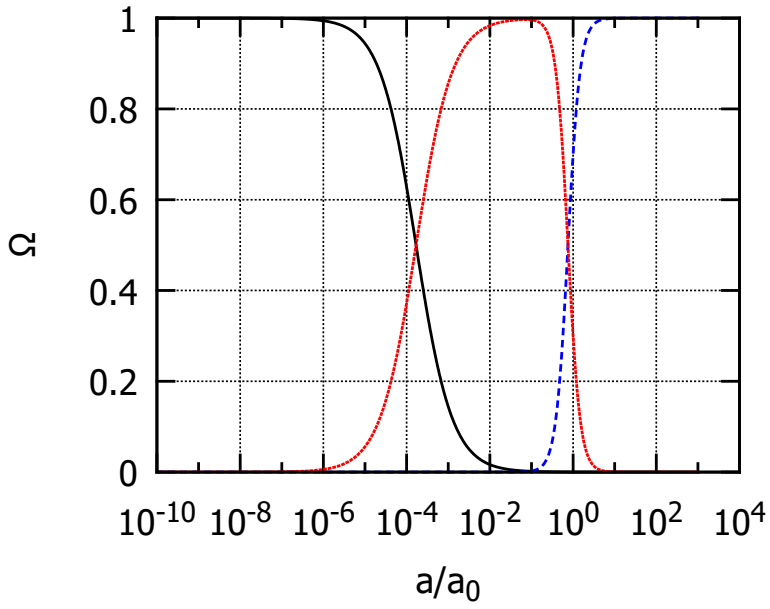

Figure 1.6: Density parameters Ω_i (1.9) as a function of scale factor are plotted. Blue dashed line corresponds to DE, red dashed (with small increments) line corresponds to matter and black line to radiation. $a_0 = 1$ is chosen as a present value of the scale factor.

1.4.2.1 Extra fields

In addition to the ordinary tensor field which is metric, we can add extra fields. By doing that, we modify the right hand side of the Einstein's equation (1.1). We can call these models as modified matter models. The main idea is that energy-momentum tensor has some additional matter component which creates accelerated expansion, i.e. it has negative pressure.

1). *Scalar-Tensor*: Quintessence; Brans-Dicke theory; Horndeski's theory; coupled DE and matter; unified DE and matter - Chaplygin gas.

2). *Vector-Tensor or Einstein-Æther theories*: Milgrom's Modified Dynamics (MOND) (*Milgrom*, 1983).

3). *Bimetric theories*: Drummond's theory; Massive gravity (*Hassan and Rosen*, 2012a) - assumes additional non-dynamical tensor field; Bigravity (*Hassan and Rosen*,

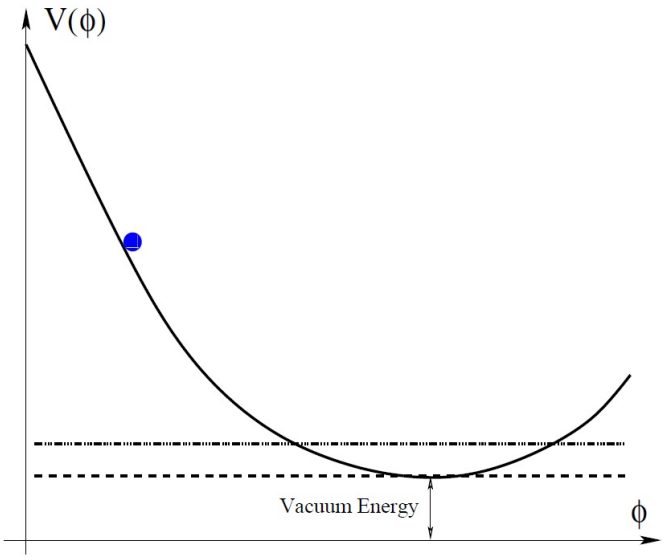

Figure 1.7: Generic scalar potential $V(\phi)$. The scalar field rolls down the potential eventually settling at its minimum, which corresponds to the vacuum. The energy associated with the vacuum can be positive, negative, or zero. (Adopted from *Frieman et al.* (2008).)

2012b) - assumes additional dynamical tensor field which works as extra metric; Multimetric gravity; Bimetric MOND (*Milgrom*, 2009).

4). *Tensor-Vector-Scalar theories*: TeVeS; Scalar-Vector-Tensor theory of gravity (STVG).

5). *Other theories*: the Einstein-Cartan-Sciama-Kibble (ECSK) theory - equivalent to GR, but at least one matter field has intrinsic spin.

Now, we are going to make a bit more precise look at a couple extra field theories.

Quintessence. The main idea of the quintessence model is that DE has the form of a scalar field which is going slowly to the potential minimum (fig. 1.7). The Einstein-Hilbert action in this case

$$S = \int d^4x\sqrt{-g}\Big(- \frac{1}{16\pi G}R + \frac{1}{2}g^{\mu\nu}\partial_\mu\phi\partial_\nu\phi - V(\phi)\Big) + S_M, \tag{1.24}$$

where S_M denotes usual matter action and ϕ is a scalar field.

Equation of the evolution of the ϕ-field

$$\ddot{\phi} + 3H\dot{\phi} + V'(\phi) = 0 \tag{1.25}$$

The pressure and energy-density of the ϕ-field are

$$\rho_\phi = \frac{1}{2}\dot{\phi}^2 + V(\phi) \tag{1.26}$$

$$p_\phi = \frac{1}{2}\dot{\phi}^2 - V(\phi) \tag{1.27}$$

Using definition of the EOS (1.16), we can write

$$\omega_\phi = \frac{p_\phi}{\rho_\phi} = \frac{\frac{1}{2}\dot{\phi}^2 - V(\phi)}{\frac{1}{2}\dot{\phi}^2 + V(\phi)} \tag{1.28}$$

In the case when the kinetic term $\frac{1}{2}\dot{\phi}^2$ is much smaller than the potential energy term $V(\phi)$, the EOS ω is close to -1 and it behave like CC and it agrees with observational data (see fig. 1.5).

Chaplygin gas. We can assume that the energy-density of the background fluid changes with time. This fluid is called Chaplygin gas and the relation between pressure and energy-density has the form

$$p = -\frac{A}{\rho^\alpha} \tag{1.29}$$

where A is a positive constant. Using conservation equation (1.3), we get

$$p(t) = \Big(A + \frac{B}{a^{3(1+\alpha)}}\Big)^{\frac{1}{1+\alpha}}. \tag{1.30}$$

In the early epoch, i.e. when scale factor is small, it behaves like $\rho \propto a^{-3}$ and corresponds to matter dominant Universe. In the late epoch, i.e. for the big scale

factors, $\rho \approx A^{\frac{1}{\alpha+\alpha}} = const$, which corresponds to the de Sitter Universe. We see that Chaplygin gas behaves as matter at the early stage and as DE at the late epoch. This is the reason why we call it unified DE and matter.

1.4.2.2 Higher derivatives

We can modify the left hand side of the Einstein's equation (1.1). In the previous section, we were adding extra fields. In this section we are going to modify gravity itself.

1). *Time derivatives*: $f(R)$ theories - adding extra Ricci scalars R to the action; theories with extra Ricci and Riemann curvature tensors $R_{\mu\nu}R^{\mu\nu}$ and $R_{\mu\nu\rho\lambda}R^{\mu\nu\rho\lambda}$.

2). *Space derivatives*: Horava-Lifschitz gravity - space and time are not equivalent at the high energy limit.

3). *Infinite derivatives*: occurs in string theory.

4). *Galileons*: 2nd order in derivatives, but it has non-trivial derivative interaction term. Scalar field, the galileon, has derivative self-interactions. Graviton and galileon are coupled only trough matter fields.

f(R) gravity. We are going to briefly review the simplest f(R) gravity and its cosmological consequences.

In general relativity Lagrangian has the from $\mathcal{L} = \sqrt{-g}R$, which is changed in f(R) gravity

$$\mathcal{L} = \sqrt{-g}f(R). \tag{1.31}$$

Varying action with respect to metric $g_{\mu\nu}$ we can get modified Einstein's equation

$$f_R R_{\mu\nu} - \frac{1}{2}f g_{\mu\nu} - f_{R;\mu\nu} + g_{\mu\nu}\Box f_R = \frac{\chi}{2}T_{\mu\nu}, \tag{1.32}$$

where subscript $_R$ denotes partial derivative with respect to R, χ is a constant and

" ; " represents covariant derivative. We can see that this equation is 4th order in derivatives, but it has special case $f(R) = R$ which reproduces usual Einstein's equation (1.1).

It should be noted that f(R) could be conformally transformed into a frame in which the field equations (1.32) become those of GR with minimally coupled scalar field. This is the statement of so-called Bicknell's theorem. Since we saw in (1.4.2.1) that the EOS is compatible with data, we can conclude that this model as well can potentially explain DE.

Unfortunately, f(R) gravity does not survive Solar system tests. However, this problem could be resolved using so-called Chameleon mechanism [*Khoury and Weltman* (2004)]. The idea is that in the presence of other matter fields the scalars can acquire an effective mass parameter that is environmentally dependent: it hides extra degrees of freedom where GR works perfectly - dense regions, but it has interesting behavior in the less dense regions. One of the examples could be the following potential

$$V_{eff} = V(\phi) + \rho e^{\beta\phi}, \tag{1.33}$$

where the mass of the scalar field is $m_\phi = \frac{d^2 V_{eff}}{d\phi^2}$.

Similar problem appears in the massive gravity and in the bigravity. The solution to this problem was found by Vainshtein (*Vainshtein*, 1972) and it is called Vainshtein mechanism.

1.4.2.3 Higher dimensions

General relativity is based on the assumption that the space and time form 3+1 dimensional manifold. However, usual Riemannian geometry is not restricted just to these 4 dimensions and we are free to study gravity in higher dimensions. One of the motivation to do that is supersting theory, which is formulated in 10 dimensions.

1). *Kaluza-Klein theories (KK)*: the basic idea is to formulate GR in 4+1 dimen-

sions and the one additional dimension is small and compact.

2). *The Braneworld paradigm*: extra dimensions can be larger than in KK theory and even infinite.

3). *Randall-Sundrum gravity (RS)*: in the braneworld the bulk (higher dimensional space-time) is flat. However, in RS gravity the bulk is an anti-de Sitter space.

4). *Cardassian model (Freese and Lewis, 2002)*: introduction of a new energy-density term into Friedmann equation, which contains only matter and radiation.

5). *Dvali-Gabadadze-Porrati gravity (DGP)* (*Dvali et al.*, 2000): the model assumes that ordinary 3+1 dimensional space is embedded inside 4+1 dimensional space. There are two terms in the Einstein-Hilbert action: one of them involves only 4 dimensional space and it dominates at short distances, while the second term is extended to all the 5 dimensions and it dominates at large scales.

Cardassian model. Cardassian model was proposed by *Freese and Lewis* (2002). The main idea is to add an extra energy-density term into Friedmann equation, which contains only matter and radiation (this term could be explained using extra dimensions *Chung and Freese* (2000)). In this case the Universe is flat and matter dominant. However, this second term dominates at a late stage of the evolution of the Universe and during its domination epoch, Universe accelerates.

Friedmann equation (1.4) could be rewritten as

$$H^2 = A\rho + B\rho^n. \tag{1.34}$$

During domination of the first term, we observe usual stages of the evolution of the Universe, i.e. radiation dominant epoch and matter dominant epoch. When the second term starts to dominate we observe accelerated expansion. In order to have accelerated expansion, the power of the second term must be $n < 2/3$. It should be noted that if $n < 1/3$ the Universe acceleration increases, for $n > 1/3$ the acceleration

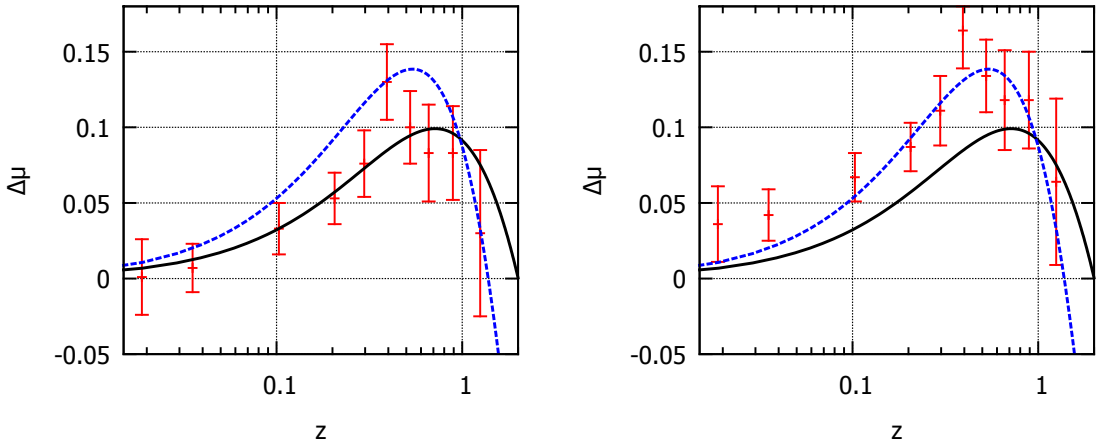

Figure 1.8: Magnitude-redshift relation. Binned data for SNIa are shown in red. Blue dashed line corresponds to ΛCDM model with $\Omega_\Lambda = 0.721$, black solid line describes the best fit power law cosmology, $\beta = 1.52$. Left panel is plotted using the best-fit value of the Hubble parameter for the power-law cosmology, $h_0 = 0.69$, while right panel is plotted using the best-fit value of the Hubble parameter for the ΛCDM model, $h_0 = 0.70$. Note that h_0 enters only into data representation, while theoretical curves are h_0-independent here. (Adopted from *Dolgov et al.* (2014)).

decreases, $n = 1/3$ - constant acceleration and for $n = 2/3$ we get term $H^2 \propto a^{-2}$, which behaves as curvature term.

1.4.3 Inhomogeneous LTB model

The main idea of the inhomogeneous Lemaitre-Tolman-Bondi (LTB) (*Enqvist*, 2008) is that there are inhomogeneities in the distribution of matter on a large scale → we live in an underdense region of the Universe and describe its behavior, a faster expansion compares to the outside, as an apparent cosmic acceleration.

In a homogeneous Universe the expansion rate is a function of time only, but in an inhomogeneous Universe the expansion rate varies both with time and space.

1.4.4 Power-law cosmology

On the purely phenomenological basis, we can write power-law model. It is based upon assumption of power-law dependence of the scale factor as a function of time

$$a(t) \propto t^{\beta}. \tag{1.35}$$

By fitting Union 2 (*Amanullah et al.*, 2010), JLA (*Betoule et al.*, 2014b) and BAO, it was shown by *Dolgov et al.* (2014) that power-law and ΛCDM are both equally good fits to the data (fig. 1.8). The best-fit value is $\beta \approx 1.5$, which means that scale factor behaves as $a(t) \propto t^{1.5}$.

Overall, broad range of reviews are available on the topic of alternative theories of gravity. *Clifton et al.* (2012) is a great and very complete review about modified gravity theories. *Yoo and Watanabe* (2012) is a good review of the basic models of DE. Reviews about theory of DE: *Copeland et al.* (2006); *Tsujikawa* (2011); *Tsujikawa* (2010).

1.5 Galaxy clusters as a cosmology probe

Galaxy clusters are one of the most fascinating objects in our Universe. These are the biggest gravitationally bound objects which contain up to thousands of galaxies or up to $\sim 10^{15}$ stars. While having these huge number of stars, galaxy clusters mainly consist of intergalactic gas ($\sim 10 - 15\%$) and dark matter ($\sim 85 - 90\%$) (*Planck Collaboration et al.*, 2013) leaving only $\sim 0.5 - 5\%$ to stars (*Andreon*, 2010) (the lowest stars contribution is observed in the most massive galaxy clusters with $M_{200} \approx 10^{15} M_{\odot}$). Moreover, galaxy clusters can be used as a cosmological and gravitational probe in addition to other probes such as SNIa, CMB and BAO (see section 1.3). To start with, we need to be able to describe matter distribution of galaxy cluster.

1.5.1 Models of galaxy clusters matter density

Galaxy clusters total density is usually measured by weak lensing and it can be described by several models. Navarro-Frenk-White (NFW) model (*Navarro et al.*, 1996, 1997) is the most broadly used

$$\rho_{NFW} = \frac{\rho_s}{\frac{r}{r_s}(1+\frac{r}{r_s})^2}, \tag{1.36}$$

where ρ_s and r_s are two parameters of the model and we can define concentration parameter $c_{200} = r_{200}/r_s$ which describes the overall shapes of the density profiles. Generally speaking, relationship between M_{200} and c_{200} is clearly defined (*Diemer and Kravtsov*, 2015). The observed weak lensing data used in this work were taken from *Sereno* (2015) who uses the following m-c relationship

$$c_{200} = A\Big(\frac{M_{200}}{M_{pivot}}\Big)^B (1+z)^C, \tag{1.37}$$

where $A = 5.71 \pm 0.12, B = -0.084 \pm 0.006, C = -0.47 \pm 0.04, M_{pivot} = 2 \times 10^{12} M_\odot/h$ (*Duffy et al.*, 2008).

The first introduction of the Einasto model was made by *Einasto* (1965)

$$\rho(r) = \rho_0 \exp(-s^{1/n}) \tag{1.38}$$

where $s \equiv \frac{r_0}{r}$, r_0 is the scale radius, ρ_0 is the normalization and n is the power index. Einasto and NFW are the two models of the total mass of galaxy clusters which are used throughout this work. Other models include gamma model (*Dehnen*, 1993) and the model proposed by *Rasia et al.* (2004).

It should be noted that weak lensing data provide us with the total mass distri-

bution, so to find DM mass we need to subtract baryon mass from it

$$M_{DM} = M_{tot} - M_b, \tag{1.39}$$

where M_{tot}, M_{DM} and M_b are the total mass, the dark matter mass and the baryon matter mass of a cluster.

X-ray is used as a source of intergalactic gas mass estimation. To describe M_b and baryon density distribution different types of models which are based on beta model (*Cavaliere and Fusco-Femiano*, 1978) are used. It should be noted, that for the heavy systems used in current work (i.e. $M_{200} \approx 10^{15} M_{\odot}$), stellar mass contribution is on the order of $0.5 - 1\%$ (*Andreon*, 2010), which allows us to safely use X-ray data as a description of the total baryon mass distribution. However, we do explore stellar mass contribution effect on our results as an additional source of uncertainty.

1.5.2 Matter density profiles as a gravity probe

One basic way to test some gravity models is to use matter distribution of different massive components of galaxy clusters. As we have seen, EG is a powerful theory which predicts direct connection between baryonic and dark matter (1.11), i.e. simply by knowing baryon mass distribution one can predict DM mass distribution. This could be directly tested by utilizing baryon matter distribution measured by using X-ray data (*Vikhlinin et al.*, 2006) and total mass profiles from weak lensing (*Sereno et al.*, 2016). As we can see on the figure 1.9, while direct measurement of $M_{DM}(r)$ diverges from EG prediction (i.e. $M_{DM,EG}(r)$), both results agree at $\sim 0.7 - 0.8 R_{200}$. More thorough analysis of the EG model based on 23 galaxy clusters is done in chapter II.

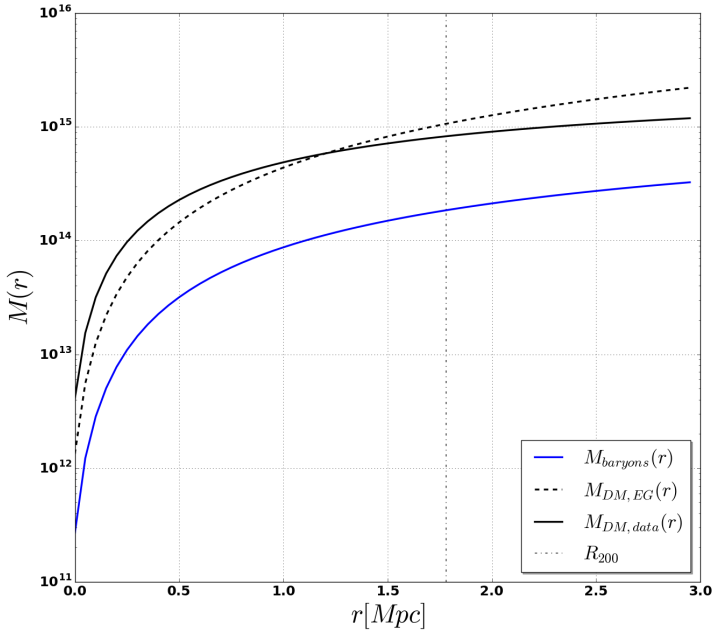

Figure 1.9: $M(r)$ is the total mass inside spherical shell with radius r. Baryonic (blue), DM (black solid) and DM predicted by EG model (see formula 1.11) based on baryonic mass distribution $M_{baryons}(r)$ (black dashed). Vertical dot-dashed line corresponds to $r = R_{200}$. It could be seen that $M_{DM}(r)$ diverges from $M_{DM,EG}(r)$ at all radii except $r \sim 0.7 - 0.8R_{200}$.

1.5.3 Models of gravitational potential

In addition to the static test of gravity using matter distribution only, we can use dynamical properties of galaxy clusters. Poisson equation

$$\nabla^2\phi = 4\pi G\rho \tag{1.40}$$

allows us to describe gravitational potential ϕ by knowing a spherical matter density distribution ρ. After integration, one finds an explicit expression for ϕ as a function of density

$$\phi(r) = -4\pi G\Big(\frac{1}{r}\int_0^r \rho(r')(r')^2 dr' + \int_r^\infty \rho(r')r'dr'\Big). \tag{1.41}$$

Applying Poisson equation to the total mass distribution models, we find potential

in terms of NFW model (1.36)

$$\phi_{NFW}(r) = -g(c_{200}) \ln\Big(\frac{r}{r_s} + 1\Big) \frac{GM_{200}}{r}, \tag{1.42}$$

where $g(c_{200}) = \Big(\ln(1 + c_{200}) - \frac{c_{200}}{1+c_{200}} \Big)^{-1}$.

Similarly, Einasto model predicts ϕ, but in slightly more bulky expression (*Retana-Montenegro et al.*, 2012)

$$\phi(r) = -\frac{GM}{r} \Big(1 - \frac{\Gamma\Big(3n, s^{1/n}\Big)}{\Gamma(3n)} + \frac{s\Gamma\Big(2n, s^{1/n}\Big)}{\Gamma(3n)} \Big). \tag{1.43}$$

where $\Gamma(a, b) = \int_b^\infty t^{a-1} e^{-t} dt$ is an incomplete gamma function.

1.5.4 Escape velocity profiles

To escape gravitational potential of a massive body, an object needs to have kinetic energy (K) higher than potential energy (U). Kinetic energy is $K = \frac{mv^2}{2}$, where m is a mass of the object and potential energy is $P = m\phi$. Above statement can be rewritten as following

$$\frac{mv_{esc}^2}{2} = m\phi, \tag{1.44}$$

where v_{esc} is the escape velocity, i.e. the minimum velocity needed for the object to escape gravitational field of a central massive object

$$v_{esc}(r) = \sqrt{-2\phi(r)}. \tag{1.45}$$

Above expression shows that by measuring escape velocity profile $v_{esc}(r)$, one can directly measure gravitational potential of the object.

Overall, dynamical properties of galaxy clusters can be described by a distribution of the galaxies on a phase-space diagram, which represents velocities and positions

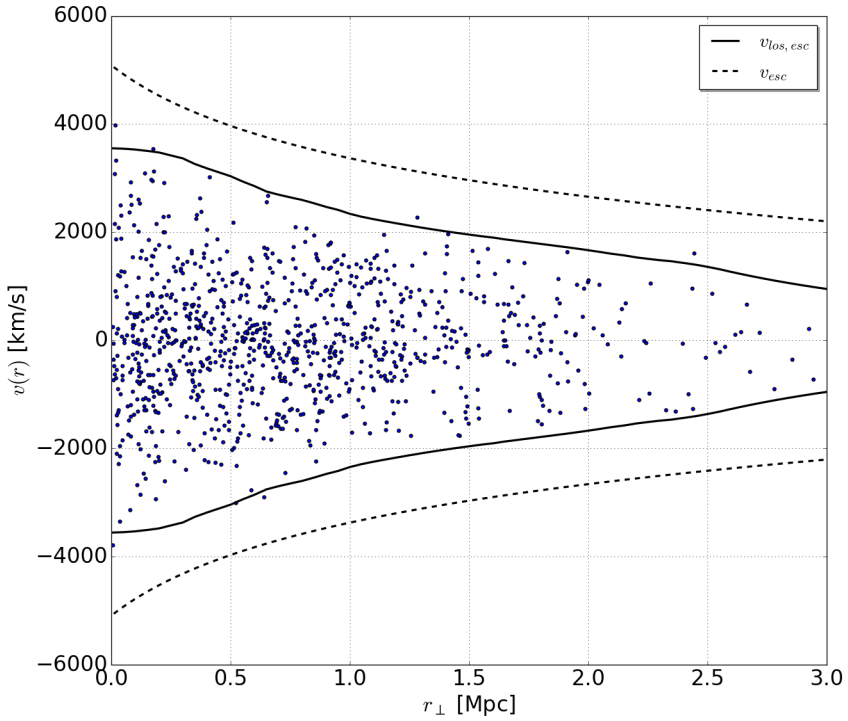

Figure 1.10: Projected phase-space diagram of a galaxy cluster. Dots correspond to positions and velocities of individual galaxies. Dashed black lines correspond to 3-dimensional escape velocity profile (1.45). Solid black lines correspond to the maximum observed on projected-phase space diagram velocity profile measured by using interloper removal prescription proposed by *Gifford et al.* (2013).

of individual galaxies relatively to the center of the cluster (see blue dots on figure 1.10). Individual galaxies which are gravitationally bound to the cluster can not have velocity higher than $v_{esc}(r)$ and the galaxies with the highest velocities are close to be able to escape gravitational field of the central object. By directly measuring on the phase-space diagram velocity profile, which consists of the galaxies with the highest velocities, one can observe $v_{esc}(r)$, which in turn is a measure of gravitational potential (1.45). Due to limited number of galaxies per cluster in observational data catalogs, special procedure of measuring escape velocity profile needs to be applied. This procedure was developed by *Gifford et al.* (2013) and it is applied throughout

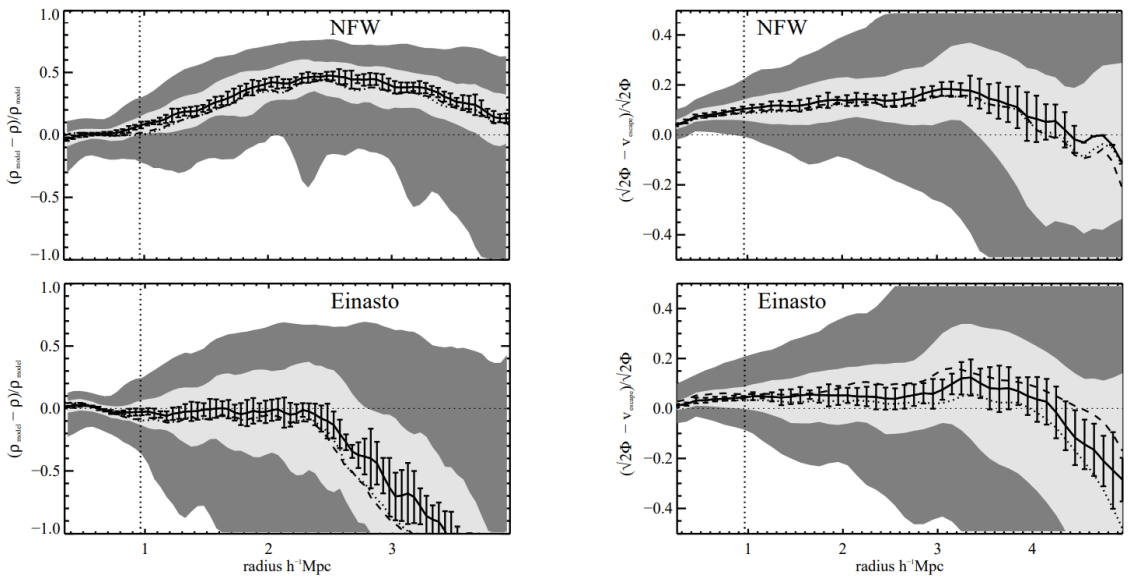

Figure 1.11: Left: density profiles of NFW (1.36) (top) and Einasto (1.38) (bottom) models are used to measure density of simulated halos (*Springel et al.*, 2005). Partial ratios of densities predicted by these two models and directly measured from simulations are presented. Models are fitted for $r < R_{200}$ and extrapolated at higher radii where they compared with simulated data. One can notice substantial overestimation of the density by NFW model, while Einasto model successfully predicts density all the way up until $\sim 2.5h^{-1}$Mpc. Right: v_{esc} from using best-fit parameters of fitting densities (left figures) in application to NFW (1.42) and Einasto (1.38) potential models. Partial ratios of v_{esc} predicted by NFW (top) and Einasto (bottom) with directly measured v_{esc} are plotted. Due to overestimation of the density at high radii, NFW model significantly overestimates escape velocity profile all the way starting from the core. (Adopted from *Miller et al.* (2016)).

this work.

It should be noted, that NFW density profile (1.36) tends to over estimate mass in the outskirts of galaxy clusters (see top left figure 1.11), while Einasto model does not have this issue (*Miller et al.*, 2016). This is due to the shape of the NFW model (1.36) which is an inverse power-law and it can not fall as quickly as exponential expression such the one Einasto model uses to correctly describe density profiles of galaxy clusters at high radii (i.e. $r > R_{200}$). It should be noted that both of these

profiles work great in the inner region up to R_{200} and start to split afterwards, so this does not produce any negative consequence for those who are working explicitly with density profiles in the inner regions of galaxy clusters.

However, NFW density overestimation produces highly negative effect on precision of gravitational potential as it is obtained by integrating density all the way up to ∞ (1.41). This creates significant effect on gravitational potential starting from the cores of galaxy clusters. Due to correct prediction of the density profile by Einasto model all the way to $\sim 2.5h^{-1}$Mpc (see bottom left figure 1.11), v_{esc}, predicted by Einasto potential (1.43) using parameters from fitting densities of the simulated halos, correctly describes the true measured escape velocity profiles (bottom right figure 1.11). For this reason, we mostly utilize the Einasto model throughout this work.

1.5.5 Escape velocity profiles in an expanding universe

Due to the presence of dark energy, simple equation (1.45) should be modified. To calculate potential from matter density, we solve Poisson equation (1.40), by integrating it up to the point, where potential is zero, i.e. up to ∞. However, DE creates a gravitational pull which effectively decreases gravitational potential. This forces gravitational potential to be equal to zero at some finite distance, which is called equilibrium radius

$$r_{eq} = \Big(- \frac{GM}{q(z)H^2(z)} \Big)^{1/3}, \tag{1.46}$$

where deceleration parameter is

$$q(z) = \frac{1}{2}\Omega_m(z) - \Omega_\Lambda(z). \tag{1.47}$$

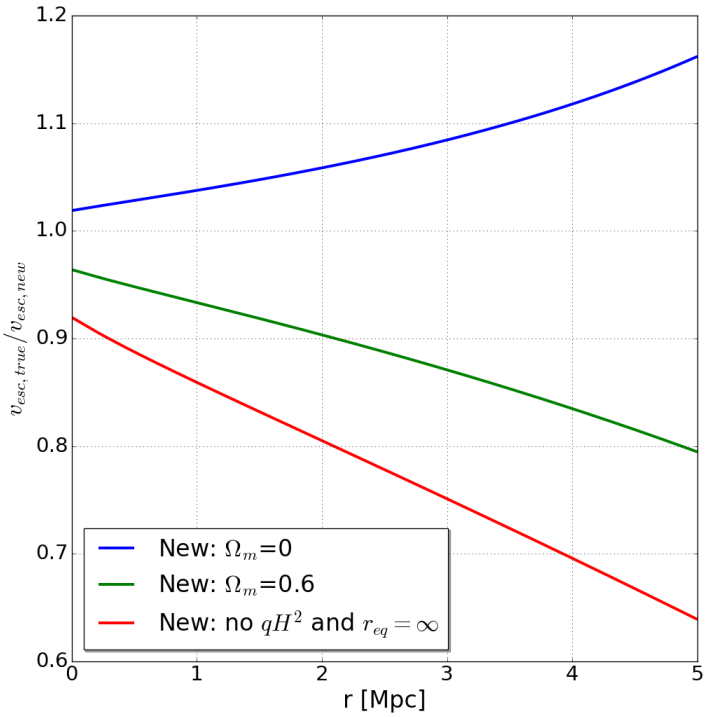

Figure 1.12: The ratio of escape velocities $v_{esc,true}/v_{esc,new}$ is presented. Index $_{true}$ corresponds to the cosmology with $\Omega_m = 0.3, h_0 = 0.7$. Index $_{new}$ corresponds to cosmologies with other Ω_m's: $\Omega_m = 0$ (blue), $\Omega_m = 0.6$ (green) and red line corresponds to the case without cosmological contribution, i.e. v_{esc} in the form (1.45) instead of (1.48) using which the rest of the cases were calculated.

Behroozi et al. (2013b) applied this idea and derived connection between v_{esc} and gravitational potential in a cosmological background

$$v_{esc} = \sqrt{-2[\phi(r) - \phi(r_{eq})] - q(z)H^2(z)[r^2 - r_{eq}^2]}. \tag{1.48}$$

The effect of cosmology on v_{esc} can be seen on figure 1.12, where we can see substantial difference in v_{esc} between the case without cosmology (1.45) and with cosmological contribution (1.48) by focusing on the red line, which already in the core overpredicts v_{esc} by $\sim 10\%$.

1.5.6 Projection effects on phase-space diagram

As we have seen, galaxy clusters provide a direct measure of gravitational potential through observation of v_{esc}. Moreover, it provides us with opportunity of testing cosmology. However, we observe galaxies only from one point of view, i.e. effectively having only 2-dimensional information, while we need to know 3-dimensional gravitational potential to correctly infer v_{esc} and to test cosmology.

In general, to build projected phase-space we need to infer individual galaxy distances from the center of the cluster ($r_\perp$)

$$r_\perp = r_\theta\Big(\frac{1}{1+z_g}\frac{c}{H_0}\int_0^{z_g}\frac{dz'}{E(z')}\Big), \tag{1.49}$$

where r_θ and $r_\perp$ are angular and radial separations between galaxy and the center of the cluster, $E(z) = \sqrt{\Omega_\Lambda + \Omega_M(1+z)^3}$. Moreover, we need to know velocities along line-of-sight (v_{los}) from redshifts (z_g) of galaxies and redshift of the cluster center (z_c)

$$v_{los} = c\Big(\frac{(1+z_g)^2-1}{(1+z_g)^2+1} - \frac{(1+z_c)^2-1}{(1+z_c)^2+1}\Big), \tag{1.50}$$

where c is the speed of light and relativistic Doppler effect formula was used ($1+z = \sqrt{\frac{1+v_{los}/c}{1-v_{los}/c}}$).

These two expressions provide us with all the required information to build projected phase-space (e.g. blue dots on figure 1.10), from which we measure maximum observed velocity profile ($v_{los,esc}$) by inferring the edge of this phase-space (see solid black line on figure 1.10) in an identical manner as we infer v_{esc} (i.e. by using interloper removal prescription proposed by *Gifford et al.* (2013)). However, observed edge on the projected phase-space diagram is suppressed in comparison with v_{esc} (e.g. dashed line is significantly lower than solid line on figure 1.10) meaning that we need to find this suppression to be able to utilize phase-spaces and v_{esc} to test cosmology.

One such approach was introduced by *Diaferio and Geller* (1997); *Diaferio* (1999). This approach is based on idea of the suppression being function of anisotropy parameter

$$\beta = 1 - \frac{\sigma_\theta^2}{\sigma_r^2}, \tag{1.51}$$

where σ_θ and σ_r are tangential and radial velocity dispersions. Dispersion is

$$\sigma^2(r) =< v^2(r) >, \tag{1.52}$$

where $v(r)$'s are velocities of individual galaxies measured with respect to zero (i.e. to the cluster frame of reference) and the average $< \cdot >$ is over all the galaxies inside a radial bin at r with a width Δr that gravitationally bound to the galaxy cluster. The range of possible values of $\beta(r)$ is $(-\infty; 1]$ with individual cases $\beta(r) = -\infty$, when the galaxies inside clusters are on fully circular motion. In the case $\beta(r) = 1$ galaxies follow radial infall and at the intermediate stage when $\beta(r) = 0$, galaxy velocities isotropically distributed.

Diaferio (1999) derives the expression which connects v_{esc} and $v_{los,esc}$ through anisotropy parameter β

$$v_{los,esc}(r) = \frac{1 - \beta(r)}{3 - 2\beta(r)} v_{esc}(r). \tag{1.53}$$

However, we show in chapter III, that this approach has issues which make it extremely problematic to apply to the real systems with small number of galaxies. Instead, we develop and apply a novel approach to infer suppression, which we show is independent of anisotropy parameter $\beta(r)$, mass of the cluster and cosmology. This provides us with necessary information to infer v_{esc}, which subsequently leads to ability of testing cosmology.

1.6 Outline of current manuscript

The primary focus of this work is to test cosmological and gravitational models. In chapter II by utilizing baryon and dark matter density distributions we test Emergent Gravity model, which is a great example of applying galaxy clusters to probe gravity which was similarly done in *Nieuwenhuizen* (2017) (where information of only one non-spherically symmetric cluster was utilized) and *Ettori et al.* (2019) (where 13 clusters from the narrow small redshifts range ($z \approx 0.047 - 0.091$) with reconstructed hydrostatic mass profiles which have non-negligible hydrostatic bias due to non-thermal pressure sources were used). Our work collects 23 galaxy clusters, which helps to address sample variance. Moreover, careful analysis of possible systematic uncertainties in the observed weak-lensing and X-ray profiles was conducted.

Chapter III focuses on exploring possible effects due to projection, with the main goal of answering the question of the amount of suppression of escape velocity profile. The novel approach of simulation of galaxy clusters is proposed and carefully investigated on N-body Millennium simulated data set (*Springel et al.*, 2005). Our approach is capable of predicting maximum observed velocity profile ($v_{los,esc}$) to a $\sim 2\%$ agreement with simulations. Application of this approach allowed us derive functional form of suppression and show that it is independent of anisotropy (in contrast to *Diaferio* (1999)), of mass of the cluster and cosmology. We show that it is only a function of number of galaxies and with a high enough sampling we should be able to reconstructs v_{esc} in projected phase-space as it is suppressed to a $< 1\%$ in the range withing R_{200}.

The first attempt of the application of the functional form of the suppression to the real data in testing cosmology is presented in the section 4.5. A list of 38 galaxy clusters with weak lensing data and individual galaxy positions and redshift was collected. The application of the suppression to the real data helped us to constraint cosmological parameters Ω_m and h_0 to a few percent precision. While these results

are preliminary, they are in agreement with current probes, while favoring Cepheid observations of Hubble constant (*Riess et al.*, 2019). This is the first to our knowledge direct utilization of the projected phase-spaces of galaxy clusters in testing cosmology and placing constraints on cosmological parameters.

CHAPTER II

Testing Emergent Gravity with mass densities of galaxy clusters

2.1 Abstract

We use a sample of 23 galaxy clusters to test the predictions of an Emergent Gravity (EG) (*Verlinde*, 2017) as an alternative to dark matter. Our sample has both weak-lensing inferred total mass profiles as well as X-ray inferred baryonic gas mass profiles. Using nominal assumptions about the weak-lensing and X-ray mass profiles, we find that the EG predictions (based on no dark matter) are acceptable fits only near the virial radius. In the cores and in the outskirts, the mass profile shape differences allow us to confirm previous results that EG can be ruled out at $> 5\sigma$. However, when we account for systematic uncertainties in the observed weak-lensing and X-ray profiles, we find good agreement for the EG predictions. For instance, if the weak-lensing total mass profiles are shallow in the core and the X-ray gas density profiles are steep in the outskirts, EG can predict the observed dark matter profile from $0.3 \leq r \leq 1\mathrm{R}_{200}$, where R_{200} is the radius which encloses $200\times$ the critical density of the Universe. The required X-ray and lensing shapes are within the current observational systematics-limited errors on cluster profiles. We also show that EG itself allows flexibility in its predictions, which can allow for good agreement

between the observations and the predictions. We conclude that we cannot formally rule our EG as an alternative to dark matter on the cluster scale and that we require better constraints on the weak-lensing and gas mass profile shapes in the region $0.3 \leq r \leq 1\mathrm{R}_{200}$.

2.2 Introduction

Galaxy clusters provide a unique opportunity to study gravity in the weak-field regime. They are the only astrophysical objects which provide three simultaneous measures of gravity. We can observe the dynamical properties of clusters through the line-of-sight movement of their member galaxies. We can measure their gas content via the Bremsstrahlung X-ray emission. We can observe the distortion of spacetime through the shearing of the shapes of background galaxies. In turn, each of these needs to produce a consistent picture of the underlying gravitational theory. Our standard cosmological paradigm is based on general relativity (GR) in a de Sitter spacetime with a positive cosmological constant, where the majority of the gravitating mass is in a dark form (*Frieman et al.*, 2008). Clusters should be able to test this theory on a case-by-case basis.

This paper is concerned with one of the biggest mysteries in modern cosmology: the origin of the dark matter, which was introduced to explain the deviation from Newtonian dynamics for galaxy rotation curves (*Zwicky*, 1933; *Rubin and Ford*, 1970). Current particle theory favors options such as weakly interacting massive particles, neutrinos and axions (*Freese*, 2017). Alternatively, modified Newtonian dynamics (MOND) has been shown to provide a theoretical explanation of the galaxy rotation curves (*Milgrom*, 1983; *Milgrom*, 2008; *Famaey and McGaugh*, 2012).

Recently, there has been an advance in the theory of gravity as an emergent property of the universe. It was shown by *Jacobson* (1995b) that general relativity is an emergent theory and it is possible to derive Einstein's equations from the concept of

entropy of black holes and thermodynamic concepts such as temperature, heat and entropy. The revised emergent gravity (EG) proposal emphasizes the entropy content of space, which could be due to excitations of the vacuum state that manifest as dark energy (*Verlinde*, 2011, 2017). Briefly, this new EG defines the spacetime geometry as due to the quantum entanglement of structure at the microscopic level. Entropy then describes the information content of a gravitating system and its amount is reflected by the number of microscopic degrees of freedom. In *Verlinde* (2011), anti-de Sitter space was used to derive the surface entropic contribution around matter. In *Verlinde* (2017), de Sitter spacetime was implemented in the theory which resulted in an assumed additional bulk volume component to the entropy. This volume contribution grows as the scale-size of a system increases. The excess entropy (over the surface component) results in a scale dependence for gravity as manifested through the elastic spacetime, which in turn mimics an apparent dark matter. This apparent dark matter is a result of the presence of baryonic matter.

Given the observational signature of the gas content as the dominant baryonic component in clusters, as well as the observational signature of the spacetime metric through lensing, galaxy clusters provide a rare opportunity to test EG's predictions. However, the current model proposed in *Verlinde* (2017) makes some important simplifying assumptions, such as that objects need to be spherically symmetrical, isolated, and dynamically "relaxed". In addition to that, *Verlinde* (2017) assumes that the universe is totally dominated by the dark energy which implies that Hubble parameter $H(z)$ is a constant. Working in a small redshift regime is a good approximation to this assumption as it implies small changes to the Hubble parameter, which makes it close to being constant, as well as adds negligible corrections to the measurements due to the small change in the cosmological evolution. The real galaxy clusters which are used in the current work fit well into these assumptions as we do not include merging systems in our sample, such as the Bullet cluster, and clusters with high

redshifts.

Some progress has been done in testing EG model using galaxy clusters. *Nieuwenhuizen* (2017) tested Emergent Gravity with strong and weak lensing data of Abell 1689 cluster (a part of our data sample) and showed that EG fits the data well only with inclusion of neutrinos. *Ettori et al.* (2019) analyzed 13 clusters with reconstructed hydrostatic mass profiles and in $0.047 - 0.091$ redshift range and concluded that EG provides overall better fit in comparison with MOND especially at $\sim R_{500}$ where Emergent Gravity mass prediction matches hydrostatic mass measurements.

Our goal is to conduct a thorough analysis of all the available in the literature galaxy clusters data. We analyze 23 clusters which cover a wide redshift range $(0.077 - 0.289)$ in an extended radial range $(0.1R_{200} - 2R_{200})$ and utilization of this number of clusters helps us to mitigate sample variance, which is a dominant systematic error unaddressed in *Nieuwenhuizen* (2017). In contrast to *Ettori et al.* (2019), where only weak lensing uncertainties were analyzed, we include in our analysis systematic uncertainties on the X-ray and weak lensing observables, including biases and additional scatter from the weak lensing inferred total mass profile shapes, biases from X-ray inferred baryon profile shapes, as well as stellar mass contributions and cosmology (via the Hubble parameter).

Moreover, our cluster sample does not have issues which data of *Nieuwenhuizen* (2017); *Ettori et al.* (2019) posses: 13 clusters from *Ettori et al.* (2019) have hydrostatic bias due to non-thermal pressure sources and cluster Abell 1689 has discrepancy between mass estimates based on the X-ray data and on the gravitational lensing (*Broadhurst et al.*, 2005) and it was shown by *Sereno et al.* (2012) that Abell 1689 has an orientation bias and the discrepancy could be resolved by dropping spherical symmetry assumption used in deriving weak lensing mass (as it was mentioned above, spherical symmetry is one of the key requirements of the EG model).

In section 2.3 we introduce the theoretical framework of the EG model. Descrip-

tion of the observational data are presented in section 2.4. In section 2.5 the testing procedure is described as well as constraints of the EG model are presented. Discussion of the results and the conclusions are presented in sections 2.6 and 2.7.

For the observational data we assume a flat standard cosmology with $\Omega_M = 0.3$, $\Omega_\Lambda = 1 - \Omega_M$ and $H_0 = 100h$ km s^{-1} Mpc^{-1} with $h = 0.7$. Throughout the work we refer to the following quantities R_{200} and M_{200} which are the radius and the mass of the clusters at the point when the density drops to $200\rho_{c,z}$, where $\rho_{c,z} = 3H^2/(8\pi G)$ is the critical density of the universe at redshift z and $H^2 = H_0^2(\Omega_\Lambda + \Omega_M(1+z)^3)$. The connection between R_{200} and M_{200} is by definition the following: $M_{200} = \frac{4\pi}{3}(200\rho_{c,z})R_{200}^3$.

2.3 Theoretical framework

The full emergent gravity theory is presented in the *Verlinde* (2017) and here we point out the main ideas of the EG model as well as present the equation which provides connection between baryon matter distribution of the spherically symmetrical isolated non-dynamical system and the apparent dark matter. To do so we adopt the EG description presented in *Tortora et al.* (2018).

While the original model is derived for an n-dimensional surface area[1], we work in four dimensional spacetime and in a spherically symmetric approximation, such that the surface mass density is

$$\tilde{\Sigma}(r) = \frac{M(r)}{A(r)}, \tag{2.1}$$

where $A(r) = 4\pi r^2$ and $M(r)$ is the total mass inside a radius r

$$M(r) = \int_0^r 4\pi r'^2 \rho(r') dr'. \tag{2.2}$$

[1] $\tilde{\Sigma}$ is used in order not to confuse our reader with Σ which is the integral of the mass density along the line of sight

By incorporating quantum entanglement entropy in a de Sitter spacetime, *Verlinde* (2017) identified a thermal volume law contribution to the entropy of the universe (S_{DE}). Heuristically, one can think of emergent gravity as modifying the law of gravity due to the displacement of S_{DE} in the presence of matter. *Tortora et al.* (2018) emphasizes the "strain" as the ratio of entropy from the baryonic matter in some volume compared to the entropy from the vacuum expansion of the universe:

$$\epsilon_{DM}(r) = \frac{S_{DM}}{S_{DE}} = \frac{8\pi G\tilde{\Sigma}_{DM}(r)}{a_0}, \tag{2.3}$$

where $a_0 = cH_0$ is the acceleration scale (*Milgrom*, 1983). In regions of normal matter density with a large number of microscopic states $\epsilon_{DM}(r) > 1$, the theory recovers the simple Newtonian equations as a limit to the theory of general relativity. However, as the number of microscopic states becomes small (i.e., in low density regions of the Universe) ($\epsilon_{DM}(r) < 1$), not all of the de Sitter entropy (S_{DE}) is displaced by matter. The remaining entropy modifies the normal gravitational laws in the GR weak-field limit (i.e., the Newtonian regime). This gravitational effect can be described by an additional surface density component

$$\tilde{\Sigma}_{DM} = \frac{a_0\epsilon_{DM}}{8\pi G}. \tag{2.4}$$

where the subscript DM refers to the apparent dark matter.

To get the "mass" of the apparent DM one needs to estimate the elastic energy due to the presence of the baryonic matter. The calculations (see *Verlinde* (2017)) lead to the following inequality

$$\int_{\mathcal{B}} \epsilon_{DM}^2 dV \leqslant V_{M_b}(\mathcal{B}), \tag{2.5}$$

where ϵ_{DM} is defined in formula 2.3 and $\mathcal{B}$ is the spherical region with the area

$A(r) = 4\pi r^2$ and radius r. The r.h.s. of the inequality 2.5 is the volume which contains an equal amount of entropy with the average entropy density of the universe to the one which is removed by the presence of baryons

$$V_{M_b}(r) = \frac{8\pi G r M_b(r)}{3a_0}, \tag{2.6}$$

where $M_b(r)$ is the total mass of the baryonic matter inside some radius r.

Tortora et al. (2018) notes that most of the recent papers on the EG theory focus on the equality in the expression 2.5, but there is no particular reason to choose this case as it places the upper bound on the amount of the apparent DM. However, if we work at the maximum, we can combine equations 2.4 and 2.6 with equality in 2.5 to get

$$M_b(r) = \frac{6}{a_0 r} \int_0^r \frac{G M_{DM}^2(r')}{r'^2} dr'. \tag{2.7}$$

To find the apparent dark matter we can differentiate both sides of the equation (2.7)

$$M_{DM}(r) = \Big[\frac{a_0 r^2}{6G}\Big(M_b(r) + r\frac{\partial M_b(r)}{\partial r}\Big)\Big]^{0.5}. \tag{2.8}$$

Equations 2.7 and 2.8 provide predictions from the theory to test the data against. We use the observed baryonic matter density through the emitting X-ray gas combined with a total (dark matter plus baryonic) inferred from weak lensing to make these tests.

2.4 Data

We require inferred total mass and baryonic mass profiles for a large set of galaxy clusters. The weak lensing data are given in the NFW formulism *Navarro et al.* (1996). The baryonic data are given via a β profile *Vikhlinin et al.* (2006). Because we are going to focus on the virial region of clusters, we simplify the analysis by

using a single analytical form for all of the mass profiles. There has been much recent work (*Merritt et al.*, 2006; *Miller et al.*, 2016) on the dark matter mass profiles of clusters in simulations which show that the preferred profile is close to an Einasto form (*Einasto*, 1965). The Einasto profile is described by

$$\rho(r) = \rho_0 \exp(-s^{1/n}), \tag{2.9}$$

where $s \equiv \frac{r_0}{r}$, r_0 is the scale radius, ρ_0 is the normalization and n is the power index. Below, we discuss how we convert between the Einasto and the NFW or β models, as well as the implication of this profile homogenization.

2.4.1 Total Mass Profiles

We are using Sereno meta catalog (*Sereno*, 2015) as a source of weak lensing data of the galaxy clusters. The weak lensing parameters are presented in the NFW form (*Navarro et al.*, 1997)

$$\rho_{NFW} = \frac{\rho_s}{\frac{r}{r_s}(1+\frac{r}{r_s})^2}, \tag{2.10}$$

where ρ_s and r_s are two parameters of the model and we can define concentration parameter $c_{200} = r_{200}/r_s$, which describes the overall shapes of the density profiles. *Sereno* (2015) uses the following relationship between M_{200} and c_{200}

$$c_{200} = A\Big(\frac{M_{200}}{M_{pivot}}\Big)^B (1+z)^C, \tag{2.11}$$

where $A = 5.71 \pm 0.12$, $B = -0.084 \pm 0.006$, $C = -0.47 \pm 0.04$, $M_{pivot} = 2 \times 10^{12} M_\odot/h$ (*Duffy et al.*, 2008).

We convert the NFW profiles to the Einasto form (2.9). *Sereno et al.* (2016) has already showed that both the NFW and the Einasto density profiles are nearly identical outside the core region of clusters up to R_{200}. We confirm this and find

Table 2.1: List of Galaxy Clusters and References

Name[2]	Redshift	WL[3]	$M_{200,w}$ $(10^{14}M_{\odot})^5$	$R_{200,w}$ (Mpc)	$\rho_{0,w}$ $(10^{17}M_{\odot})$	$r_{0,w}$ (pc)	n_w	Bar[4]	$\rho_{0,b}$ $(10^{15}M_{\odot})^6$	$r_{0,b}$ (pc)	n_b
A1682	0.227	P07	6.05	1.62	6.1	65.8	4.21	G17	1.62	8980	2.89
A1423	0.214	OK15	6.7	1.68	5.8	71.9	4.19	G17	40.5	20.8	5.08
A2029	0.077	C04	10.28	2.03	5.2	86.3	4.19	V06	54.0	111.6	4.2
A2219	0.226	MULT	15.33	2.21	4.46	122.7	4.13	G17	4.63	6347.8	2.95
A520	0.201	H15	12.75	2.09	4.63	111.6	4.14	G17	0.46	97100	1.8
A773	0.217	MULT	15.45	2.22	4.43	123.7	4.13	G17	8.36	1670	3.36
ZwCl3146	0.289	OK15	7.94	1.73	5.36	86.6	4.15	G17	1170.0	1.8	5.38
RXJ1720	0.16	OK10	5.38	1.59	6.43	58	4.23	G17	250.0	7.1	5.07
RXCJ1504	0.217	OK15	8.26	1.8	5.46	81.2	4.18	Gi17	1280.0	0.9	5.58
A2111	0.229	H15	8.08	1.78	5.38	83.5	4.17	G17	9.49	535	3.9
A611	0.287	OK10	8.68	1.78	5.19	92.2	4.15	G17	260.0	6.3	5.12
A697	0.281	OK10	15.16	2.15	4.47	125.9	4.12	G17	3.16	11500	2.67
A1689	0.184	U15	18.86	2.4	4.2	137.2	4.12	Gi17	311.0	3.9	5.29
A1914	0.166	H15	11.2	2.03	4.89	99	4.16	G17	74.51	174	3.95
A2261	0.224	OK15	18.01	2.33	4.25	135.7	4.12	G17	526.0	1.1	5.79
A1835	0.251	H15	16.88	2.26	4.35	131.3	4.12	G17	568.0	4.9	5.15
A267	0.229	OK15	9.07	1.85	5.26	87.7	4.17	G17	383.0	2.2	5.48
A1763	0.231	H15	14.13	2.14	4.48	120.9	4.12	G17	2.19	11000	2.75
A963	0.204	OK15	10.66	1.97	4.95	97.9	4.15	G17	2.36	14634	2.42
A383	0.189	OK15	8.06	1.8	5.54	78.2	4.19	V06	450.0	1.9	5.39
A2142	0.09	OK08	13.63	2.22	4.74	104.4	4.16	Gi17	333.0	1.1	5.86
RXCJ2129	0.234	OK15	7.24	1.71	5.67	75.8	4.18	G17	23.8	443	3.73
A2631	0.277	OK15	12.34	2.02	4.7	112.5	4.13	G17	1.11	36800	2.17

that the Einasto parametrization can recreate a given NFW profile in the region $0.15 \leqslant r \leqslant R_{200}$ to less than 1% accuracy. This defines the statistical floor of our total mass profiles. We include additional error on the total mass profiles from the published errors in (*Sereno*, 2015).

The use of a specific mass versus concentration relationship adds a systematic uncertainty from the observations. The average concentration of our sample is $< c_{200} >= 3.15$ with specific concentrations in the range $2.57 < c_{200} < 3.58$. We also explore the effect of an additional systematic error in the concentrations on our conclusions.

[2]Cluster name. The original papers are cited above, but actual spherical weak lensing masses (and their respective errors) we use in our analysis were taken from the *Sereno* (2015) meta catalog. More specifically, *Sereno* (2015) standardizes the M_{200} masses for the clusters shown above (as inferred from each reference listed in the "weak lensing" column) for the fiducial cosmology mentioned in our introduction.

[3]Weak lensing. The abbreviations in this column refer to the following papers: H15= *Hoekstra et al.* (2015), OK08 = *Okabe and Umetsu* (2008), OK10 = *Okabe et al.* (2010), OK15= *Okabe and Smith* (2015), A14 = *Applegate et al.* (2014), C04 = *Cypriano et al.* (2004), D06 = *Dahle* (2006), P07 = *Pedersen and Dahle* (2007), U15= *Umetsu et al.* (2015). MULT = we averaged over multiple

2.4.2 Baryon profiles

In what follows we are using only gas density profile as a source of baryon density while neglecting stellar mass contribution as it is around or less than 10% of the overall baryon mass for the clusters with the masses of the clusters we use in our analysis (*Giodini et al.*, 2009; *Andreon*, 2010; *Laganá et al.*, 2013). We will test the assumption of neglecting stellar contribution later in the text. Also, we do not take into account the brightest cluster galaxy (BCG) in each of the galaxy clusters, since it was shown by *ZuHone and Sims* (2019) that the BCG contribution is negligible outside $r \sim 100$ kpc (in our analysis, we focus on the region outside $r \sim 0.1 \times R_{200}$ which is $r \sim 160 - 240$ kpc for the analyzed clusters (see table 2.1)). The gas density profiles are taken from several sources *Giles et al.* (2017); *Vikhlinin et al.* (2006); *Giacintucci et al.* (2017). Unlike the weak lensing data, the baryon density uncertainties are not reported in the papers from which the data used in this work were taken.

Giles et al. (2017); *Vikhlinin et al.* (2006) use beta profile to infer the baryon density distribution

$$n_p n_e = n_0^2 \frac{(r/r_c)^{-\alpha}}{(1+r^2/r_c^2)^{3\beta-\alpha/2}} \frac{1}{(1+r^\gamma/r_s^\gamma)^{\epsilon/\gamma}} + \frac{n_{02}^2}{(1+r^2/r_c^2)^{3\beta_2}}, \tag{2.12}$$

where n_p and n_e are the number densities of protons and electrons in a gas, r_c is the characteristic radius and n_0 is the central density. *Giles et al.* (2017) uses the same profile but without the second term in the sum, i.e. without $\frac{n_{02}^2}{(1+r^2/r_c^2)^{3\beta_2}}$.

To get the actual baryon matter density distribution, relation 2.12 is used (*Vikhlinin*

weak lensing sources to get M_{200} as well as the errors of the clusters A2219 (OK10/0K15/A14) and A773 (OK15/D06).

[4]Baryons. The abbreviations in this column refer to the following papers: G17 = *Giles et al.* (2017), V06 = *Vikhlinin et al.* (2006), Gi17 = *Giacintucci et al.* (2017)

[5]Index w stands for weak lensing in the Einasto parameters (2.9)

[6]Index b stands for baryon gas in the Einasto parameters (2.9)

et al., 2006)

$$\rho_b = 1.624 m_p (n_p n_e)^{0.5}, \tag{2.13}$$

where m_p is the proton mass.

Giacintucci et al. (2017) uses so called double beta model which provides the number density of the electrons in the gas

$$n_e = \frac{n_0}{1+f}\Big((1+\frac{r^2}{r_{c_1}^2})^{-1.5\beta_1} + f(1+\frac{r^2}{r_{c_2}^2})^{-1.5\beta_2}\Big), \tag{2.14}$$

where n_0 is the central density, the rest of the parameters are free parameters and in order to infer the baryon matter profile the following relation is used (*Schellenberger and Reiprich*, 2017)

$$M_b(r) = 4.576\pi m_p \int_0^r n_e(r') r'^2 dr'. \tag{2.15}$$

We transform the beta profiles into Einasto profiles in the identical manner as the NFW profiles what was described in the previous subsection. The Einasto profile recreates the beta profile with a high precision in the region from around the core until R_{200} (see fig. 2.4.2). While we chose to transfer beta to the Einasto profile in the region up to R_{200}, we could do this procedure with almost identical accuracy in the region up to $2R_{200}$.

We note that like for the case of the weak lensing profiles, the shapes of the baryon profiles are systematics limited. In equation 2.12, the parameter ϵ governs the shape of the baryon profile in the outskirts. Large values indicate steeper slopes. *Vikhlinin et al.* (2006) applies an upper limit of $\epsilon = 5$ and his original sample has a $\langle\epsilon\rangle = 3.24$. On the other hand, the fits to our subset of the cluster data by equation 2.12 have significantly shallower slopes at $\langle\epsilon\rangle = 1.69$. Uncertainties on ϵ are not available, and so like concentration in weak lensing NFW fits, we explore systematic errors in this parameter later on.

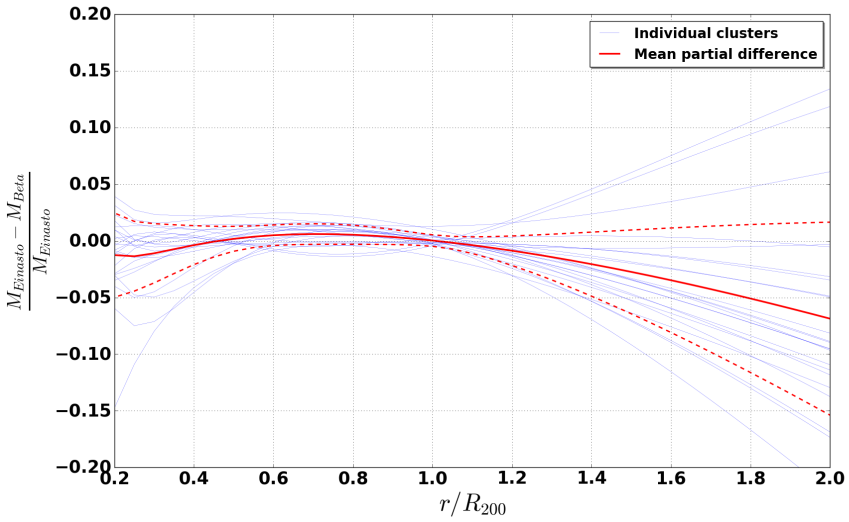

Figure 2.1: Partial difference between Einasto and beta profiles. Blue lines are the partial differences of individual clusters. Red solid line is the mean value and dashed lines are 68.3% error bars around the mean. As we can see they are almost identical all the way until R_{200} and starts to deviate outside this range. Moreover, the beta profile at average tends to overestimate the mass $M(r)$ since the partial difference is smaller than zero after R_{200}.

2.4.3 Dark Matter profiles

In what follows, we treat the weak lensing masses as total masses of the galaxy clusters and the dark matter mass is calculated as

$$M_{DM} = M_{tot} - M_b, \tag{2.16}$$

where M_{tot}, M_{DM} and M_b are the total mass, the dark matter mass and the baryon matter mass of a cluster.

2.4.4 The Clusters

We list all the 23 clusters in the table 2.1. The average mass of our set of 23 observed galaxy clusters is $< M >= 1.14 \times 10^{15} M_\odot$ while individual masses are in rather broad range $(5.4 \times 10^{14} M_\odot, 1.89 \times 10^{15} M_\odot)$. To create a list of galaxy clusters

used in this work, the following selection procedure was followed. The first criteria is the data availability, i.e. only clusters with the available in the literature weak lensing and baryon density profiles were selected. The second stage is to remove from the sample merging systems (e.g. the Bullet cluster) and clusters with high redshifts (e.g. BLOXJ1056 with $z = 0.831$). All of the clusters in our list have rather small redshifts (< 0.289) and that fits well into approximation made by the EG theory, i.e. constant Hubble parameter. However, we will still test this assumption later in the current manuscript.

2.5 Testing Emergent Gravity

We have two ways of comparing the EG model with the data. The first one is based on equation 2.7 such that we compare the observed baryon mass profile to the one predicted from the "observed" dark matter profile. Recall from Section 2.4.3 that the observed dark matter profile is actually the total mass profile from weak lensing minus the observed baryon profile. The second approach is based on equation 2.8 which represents opposite situation. In this case, we use the observed baryon profile to make a prediction for the dark matter profile and compare that to the "observed" dark matter profile.

2.5.1 Qualitative assessment of the EG model

Figure 2.2 shows the results of applying equation 2.7, which makes a prediction for the baryon profile from the dark matter profile. The red line is the observed baryon profiles using the X-ray data and including a 10% additional stellar component. The blue line comes from applying equation 2.7 using the dark matter mass profile from equation 2.16. We note that in figures 2.2 and 2.3, we have normalized each cluster baryon profile to the value at the observed weak lensing R_{200} for clarity. Actual radii (in terms of Mpc) were used in all of the statistical analyses. The solid lines

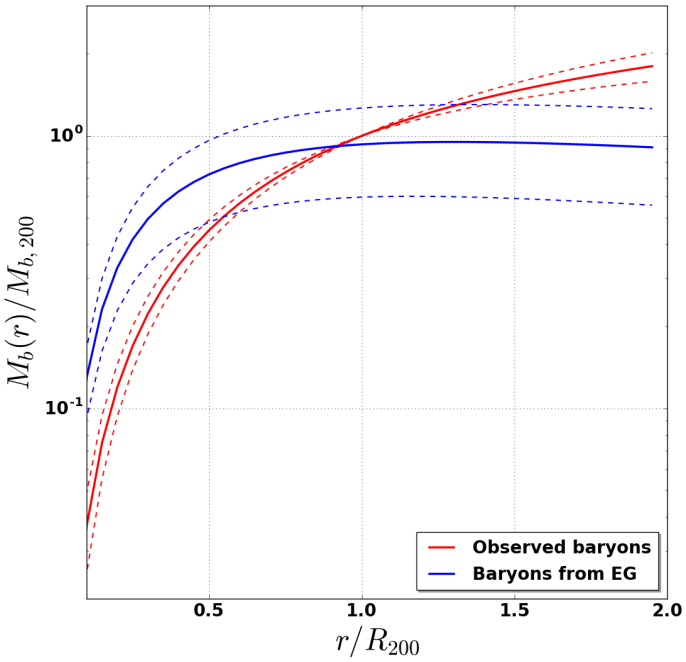

Figure 2.2: The normalized by M_b at R_{200} average total baryon mass inside a spherical region of a radius r (see f-la 2.2) for all the 23 galaxy clusters from the data of the baryon density distribution (red lines) and by applying EG relation 2.7 to the dark matter from the data (blue lines). Solid and dashed lines are the mean and 68.3% error bars around the mean. The Baryon density here was increased by 10% to account for the stellar mass. Note the agreement in the total baryonic mass at $\sim R_{200}$, except that EG predicts most of the baryons to be in the cluster cores.

represent the means of the samples and the dashed lines the observed 1σ scatter from the 23 systems. We find that the data (red) and the model (blue) agree at $\sim R_{200}$ and beyond. However, EG predicts that the majority of the baryons are enclosed within the cluster core. Specifically, EG predicts that 50% of the baryons are within $\sim 0.2 \times R_{200}$. However, the observed baryons do not reach 50% until $\sim 0.5 \times R_{200}$.

Figure 2.3 shows the results of applying equation 2.8, which makes a prediction for the dark matter profile from observed baryon profile. The red line is from the observed dark matter profiles. The blue line comes from applying equation 2.8 to the observed baryon profiles. The solid lines represent the means of the samples and the

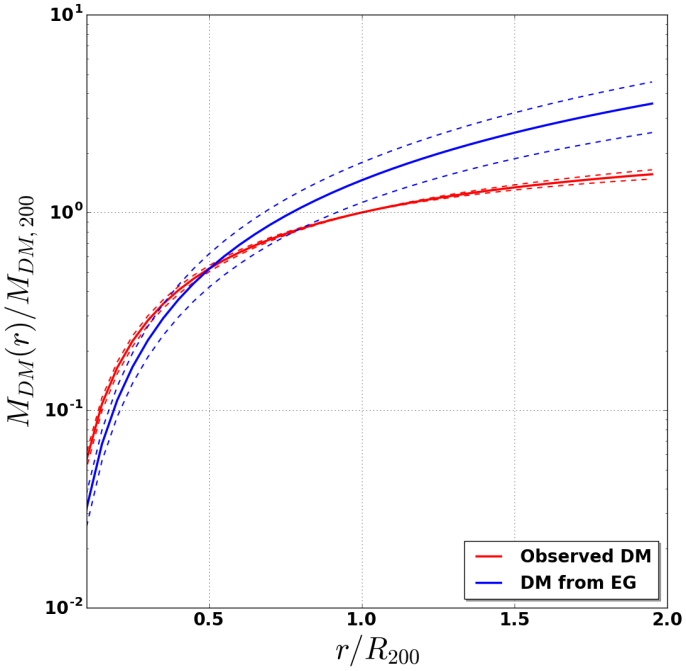

Figure 2.3: The normalized by M_{DM} at R_{200} average total dark matter mass inside a spherical region of a radius r (see f-la 2.2) from the data (red lines) and by applying EG relation 2.8 to the baryon density distribution data (blue lines). Solid and dashed lines are the mean and 68.3% sample variance around the mean. Baryon density here was increased by 10% to account for the stellar mass. One might be able to notice that blue line increases linearly starting from around R_{200} which does not look physical as we expect the mass of the galaxy clusters to stop growing at some finite radius close to a few R_{200}. Moreover, we see significant difference between blue and red solid lines especially at high radii.

dashed lines the observed 1σ scatter from the 23 systems. We normalize each of the cluster's dark matter profile to the value at the weak-lensing inferred R_{200} in order to conduct a combined analysis of all 23 galaxy clusters.

From figures 2.2 and 2.3 we find a qualitative agreement between the observations and EG theory. A key success of the theory is the amplitude it predicts, which is close to what we observe near the virial radius. In other words, using just the observed baryons, EG predicts the observed dark matter mass at $\sim R_{200}$. Likewise, the difference between the total weak-lensing inferred mass and the baryon mass at $\sim R_{200}$ is

what is predicted from EG using just the baryons alone. However, differences become apparent at smaller and larger[7] radii. Unfortunately, the observed baryon profiles are not highly constraining in the core regions and in the outskirts of clusters. The cores of clusters are active environments with varying levels of astrophysical processes which could alter the profiles. Likewise, X-ray surface brightnesses drop steeply beyond R_{500}, to the point where it becomes impossible to constrain the gas density profile out beyond the virial radius. We discuss these issues in the next subsections. In the meantime, we can first apply a more stringent quantitative comparison in the region where the data is more certain.

2.5.2 Data analysis and statistical constraint of the EG model

To compare the EG model with the data we apply fitting procedure which is based on minimization of χ^2

$$\chi^2 = \sum_i \frac{(M(r_i) - M_{th}(r_i))^2}{\sigma(r_i)^2}, \tag{2.17}$$

where $M_{th}(r_i)$ is given by the r.h.s. of the equation 2.8 (the apparent dark matter prediction by the EG model) while $M(r_i)$ and $\sigma(r_i)$ are provided by the weak lensing data. The relevant quantity to compare the model with the data is a reduced χ^2 which is calculated as $\chi^2_{d.o.f} = \chi^2/N_{d.o.f}$, where $N_{d.o.f.}$ is the number of degrees of freedom.

As shown previously, the best qualitative agreement is the radial region around the virial radius. In what follows, we measure each of the cluster mass profiles with a step $0.1R_{200}$ and for example in the range from $0.3R_{200}$ to R_{200} that gives us 8 data points per clusters and 184 data points in total as we have 23 clusters in our data sample. The total $N_{d.o.f.} = 181$, since the Einasto matter density model has three

[7] One can notice strange behaviour in EG predictions at high radii which is especially noticeable on the figure 2.2 where $M_b(r)$ starts to decrease at $\sim 1.5 \times R_{200}$. This result can be derived analytically: equation 2.7 leads to $M_b(r) \propto \frac{1}{r^2}$ assuming convergence of $M_{DM}(r)$ to a constant number at high radii.

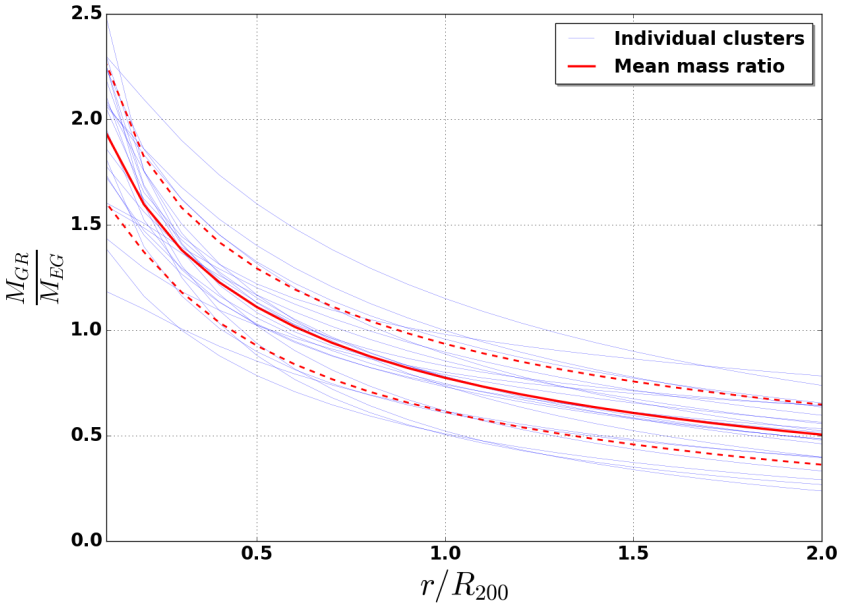

Figure 2.4: The mass ratio $\frac{M_{GR}}{M_{EG}}$ of the observed dark matter (M_{GR}) and the apparent dark matter (M_{EG}) which is predicted by the EG model. Thing blue lines are the individual mass ratios of the real 23 galaxy clusters. Red solid and dashed lines are the mean and 68.3% error bars around the mean of all the blue lines. In order for the EG model to be compatible with the observational data the red mean line should be as close as possible to the unity. Unfortunately, this is not the case all the way until approximately $0.6R_{200}$ when the red dashed line crosses unity. This result means that the EG model does not describe the observed data in all the regions except $\sim 0.6R_{200}$, i.e. the EG model underestimates the amount of matter close to the core and overestimates the mass at high radii.

free parameters.

In spite of the fact that at $\sim R_{200}$ the predicted by the EG model the apparent dark matter is similar to the observed dark matter, quantitatively we find that the profiles predicted by EG differ from the observed profiles by $> 5\sigma$. The best agreement we find is within the narrow range $0.55R_{200} \leqslant r \leqslant 0.75R_{200}$, where the EG model is only ruled out at the 2σ level.

Having uncertainties of the baryon density profiles could not easing significantly the level of the precision of the constraint of the EG model. To confirm this statement we add some error of the baryon profiles by treating $\sigma(r_i)^2$ in the formula 2.17 as a

sum of the squares of the errors of the weak lensing (σ_{weak}) and baryon masses (σ_{bar}), i.e. $\sigma(r_i)^2 = \sigma_{weak}(r_i)^2 + \sigma_{bar}(r_i)^2$. Placing uncertainties on the baryon matter even half of the uncertainties of the weak lensing data (i.e. $\sigma_{bar}(r_i) = 0.5\sigma_{weak}(r_i)$) does not decrease significantly the level of constraining EG model in the range $0.3R_{200} \leqslant r \leqslant R_{200}$ as it is still $\sim 5\sigma$. However, with these baryon matter uncertainties the EG model is compatible with the observations at almost 1σ level in the "narrow" range.

Given that the amplitude predicted by EG is reasonably well represented by the model, we focus our comparison on the profile shapes. Fig. 2.4 shows the mass ratio $\frac{M_{GR}}{M_{EG}}$ of the observed dark matter (M_{GR}) and the apparent dark matter (M_{EG}), which is predicted by the EG model. One can see that the observed dark matter is almost two times higher than the apparent dark matter in the area close to the cores ($0.1R_{200}$) of the galaxy clusters (around 40% higher at $0.3R_{200}$) and it also can be seen that the mass profiles of the dark matter and the apparent dark matter are very different. EG underestimates the dark matter mass in the regions closer to the core while overestimating the mass in the regions beyond approximately $0.9R_{200}$. At the current stage we must claim that the EG model is unable to describe the real observational data at Mpc scales.

2.5.3 Systematic uncertainty from concentration

As it was discussed above (see subsection 2.4.1), the mass-concentration relation of the galaxy clusters is a source of systematic uncertainty. We can include these systematics in the following way: $\sigma(r_i)$ in the formula 2.17 is now a sum of statistical and systematical uncertainties, i.e. $\sigma(r_i)^2 = \sigma_{weak}(r_i)^2 + \sigma_{sys}(r_i)^2$. We neglect $\sigma_{bar}(r_i)$ here as discussion of the baryon uncertainty was done in the previous subsection. We define $\sigma_{sys}(r_i)$ as the difference between true value of the $M_{DM,true}$, i.e. at the concentration which is given by the data 2.11 and $M_{DM,new}$ at the concentration

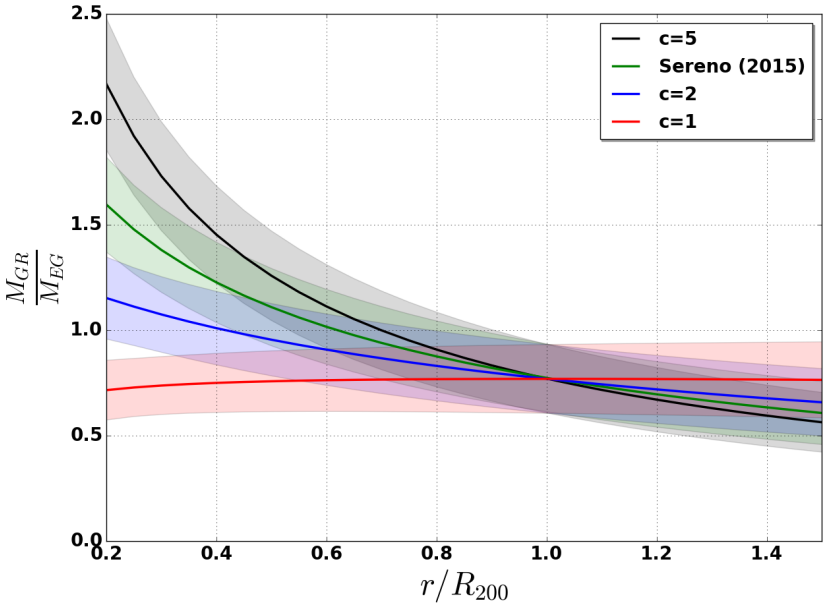

Figure 2.5: The mass ratio $\frac{M_{GR}}{M_{EG}}$ of the observed dark matter (M_{GR}) and the apparent dark matter (M_{EG}) which is predicted by the EG model. Solid lines and shaded regions around them are the mean and 68.3% error bars around the mean. Green color correspond to the case with the concentrations c_{200} which are given by *Sereno* (2015). Red, blue and black colors correspond to the concentrations $c_{200} = 1, 2$ and 5 with M_{200} given by *Sereno* (2015). As it was pointed out in subsection 2.4.1, the mean concentration of the data from *Sereno* (2015) is $< c_{200} >= 3.15$. It can be seen from the plot that the EG model prefers smaller concentrations.

motivated by *Groener et al.* (2016),

$$\sigma_{sys}(r_i) = M_{DM,true} - M_{DM,new}. \tag{2.18}$$

Through this technique, we allow the systematic uncertainty in the concentration to impact the uncertainty on the amplitude of the profiles, but not the shape. We consider the effect of systematic uncertainties by concentrations up to $c_{200,new} = 10$. We focus our analyses only on the range ($0.3R_{200} \leqslant r \leqslant R_{200}$) where the mass densities are measured with the step $0.1R_{200}$. The effect of the systematic uncertainty starts to be noticeable at $c_{200,new} \approx 4.1$ were the median $\sigma(r_i)/\sigma_{sys}(r_i) \approx 5$. This effect pushes

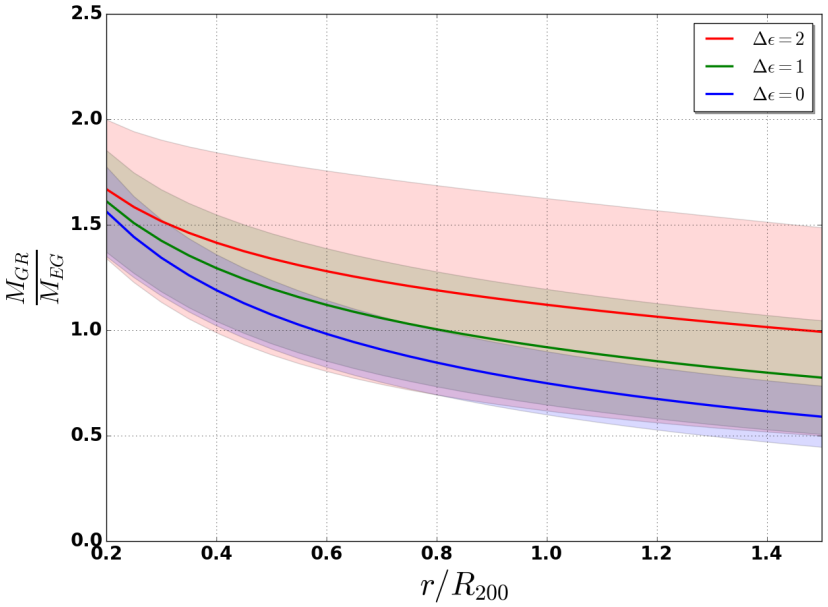

Figure 2.6: The mass ratio $\frac{M_{GR}}{M_{EG}}$ of the observed dark matter (M_{GR}) and the apparent dark matter (M_{EG}) which is predicted by the EG model. Solid lines and shaded regions around them are the mean and 68.3% error bars around the mean. Baryon matter distribution in our sample have rather small steepness which is described by ϵ in the form 2.12: $<\epsilon>= 1.69$ for 20 clusters and zero ϵ for the three clusters with double beta profiles (2.14). However, in general steepness parameter is higher (for example it is $<\epsilon>= 3.24$ in *Vikhlinin et al.* (2006)). To take that into account we have increased ϵ of the 20 clusters by 1 (green) and by 2 (red), which made steepness parameter to be $<\epsilon>= 2.69$ and $<\epsilon>= 3.69$ respectively. Blue color corresponds to the implementation of the data with the original steepness parameters.

the constraint level down to $\sim 3\sigma$ and at $c_{200,new} = 10$ the EG model is compatible with the observations at 1σ.

2.5.4 Systematic shape bias from concentration

An alternative approach to simply increasing our mass measurement errors as a result of systematic uncertainties in our χ^2 analysis, we can fix the mass measurement with our current errors but allow the profiles shapes to be more uncertain. As we can see from the figure 2.5, if we assume that the cluster weak-lensing inferred masses are

unbiased, the EG model becomes more consistent with the data for $c_{200} \approx 2$. While small, this average value for the NFW concentration of the weak-lensing mass profiles of massive clusters is close to those obtained in simulations (*Groener et al.*, 2016; *Klypin et al.*, 2016; *Correa et al.*, 2015).

2.5.5 Baryon profile bias

Three clusters from *Giacintucci et al.* (2017) utilize double beta profile (2.14) which does not take into account steepness parameter ϵ in equation 2.12. The remaining 20 clusters in our sample have average steepness parameter $< \epsilon >= 1.69$ which is significantly smaller than the average steepness parameter $< \epsilon_V >= 3.24$ of *Vikhlinin et al.* (2006) data set. Increasing ϵ in our data rotates the apparent DM distribution curve and shifts it upwards which makes the EG prediction of the apparent DM more consistent with the observation of DM (see figure 2.6). Recent results from *Ettori and Balestra* (2009); *Eckert et al.* (2012) suggest that the baryon profiles are in fact much steeper than the original beta profile and in agreement with the high ϵ values from *Vikhlinin et al.* (2006).

2.5.6 Other Systematics

One of the assumptions of the EG model, which was discussed above in the introduction, is the fixed value of the Hubble parameter. To test this assumption we divided by redshifts our data sample of 23 galaxy clusters into two bins, i.e. one bin contained 11 clusters with the lowest redshifts ($< z >= 0.17$) and the second bin contained 12 clusters with the highest redshifts ($< z >= 0.25$). Utilization of both bins produced almost completely identical results which supports the assumption made.

The second assumption which we made on the data is that the hot gas represents the total baryon mass of the clusters which is not totally true as stars contribute as well. However, stellar mass is less than 10% (*Giodini et al.*, 2009; *Andreon*, 2010;

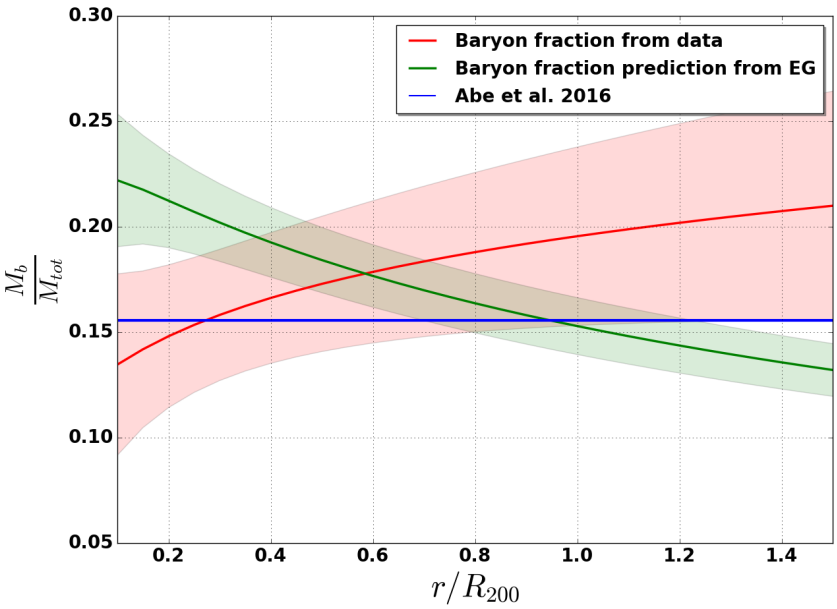

Figure 2.7: The ratio of baryon mass to the total mass of the galaxy cluster as a function of radius of the observed data set of 23 galaxy clusters. Red line and red shaded region represent the baryon fraction of the observed clusters, i.e. $M_b/M_{tot,GR}$, where M_b is the observed baryon mass, $M_{tot,GR}$ is the total mass from the weak lensing data and this result correlates with other results (*Giodini et al.*, 2009; *Andreon*, 2010) as we expect to see higher baryon fraction for heavier galaxy clusters and the average mass of the clusters in our sample is high ($< M_{200} = 1.14 \times 10^{15} M_{\odot}$). Green line and green shaded region correspond to the effective baryon fraction which is predicted by the EG model, i.e. $M_b/M_{tot,EG}$, where $M_{tot,EG}$ is the total mass predicted by the EG model, i.e. the sum of the apparent dark matter and the baryon matter. Solid lines are the mean values and shaded regions are 68.3% error bars around the means. One can observe that the EG model prediction diverge from the observed baryon fraction starting from the cores of the clusters up to $\sim 0.6 R_{200}$ which means that the EG model predicts that the baryon fraction is the biggest in the regions around the core of the clusters while the observations predict the baryon fraction to increase with a distance from the core. Interestingly, the baryon fraction prediction of the EG model agrees well with the baryon fraction which is observed from the CMB (*Ade et al.*, 2016) (see blue flat line) at around R_{200}.

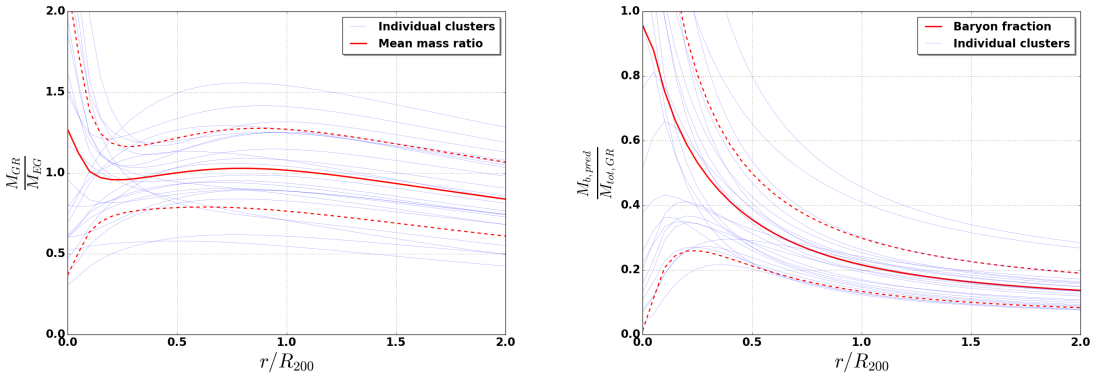

Figure 2.8: Left: the predicted dark matter mass ratio M_{GR}/M_{EG} in the case of the baryon fraction $M_{b,pred}/M_{tot,GR}$ in the form from the right figure. $M_{b,pred}$ is the predicted baryon matter, $M_{tot,GR}$ is the total observed mass from the weak lensing data, M_{GR} is the observed dark matter and M_{EG} is the predicted apparent dark matter with the predicted baryon matter $M_{b,pred}$. For the EG model to be able to properly describe the weak lensing data (left figure) the baryon fraction should have rather weird shape (right figure). One of the biggest problems with such baryon fraction is the huge amount of baryon matter in the core which is in total contradiction with the observations (compare with red line on figure 2.7) as it requires baryon fraction to be close to unity there.

Laganá et al., 2013) of the hot gas for the clusters with the masses we use in this paper ($< M_{200} >= 1.14\times10^{15}M_{\odot}$). To check this assumption, we increased the baryon mass by 10% which shifted the mass ratio $\frac{M_{GR}}{M_{EG}}$ in figure 2.4 only by approximately $0.05 - 0.08$ or changed this ratio by around 6%. This small shift in the mass ratio not only does not change the precision of constraining the EG model, but also does not change at all the main conclusion of incompatibility of the EG model with the galaxy clusters. So, the assumption of neglecting stellar masses is totally valid.

2.6 Discussion

In this section, we discuss the consequences of the current EG predictions in the context of the observation data. We also explore alternatives to our fiducial analysis which could bring the EG predictions and the data into better agreement.

2.6.1 Effect on the baryon fraction

One of the consequences of the EG model is in the distribution of the baryons in clusters. We can define the effective baryon fraction which is predicted by the EG model by introducing the following ratio

$$f_{b,EG} = \frac{M_b}{M_{tot,EG}}, \tag{2.19}$$

where M_b is the observed baryon mass and $M_{tot,EG}$ is the total mass which is predicted by the EG model.

The results of the fig. 2.7 imply that the EG effective baryon fraction is different in many aspects from the observed baryon fraction with the total mass $M_{tot,GR}$ defined by the weak lensing data. The first difference is the shape of the lines in 2.7: the EG model has a monotonically decreasing behaviour while the data shows that the baryon fraction is an increasing with the radius function. In agreement with *Nieuwenhuizen* (2017) this means that the EG predicts baryons to be concentrated in the region around the cores of the galaxy clusters while the observations imply that the baryons are actually spread in the broader regions with highest fraction in the outskirts of the clusters. Secondly, the effective baryon fraction is almost twice as high close to the core (at $r \approx 0.1R_{200}$) which should be detected as it implies brighter cluster cores than we would observe in GR. This effect could be actually smaller if BCG would be correctly taken into account by weak lensing data. In spite of these differences, the EG model predicts correctly the baryon fraction at the distances approximately $0.4R_{200} \leqslant r \leqslant 0.8R_{200}$. Additionally, the EG model predicts the effective baryon fraction to be close to 15.6% (the number which is expected from the CMB observations (*Ade et al.*, 2016)) at the distances close to R_{200} .

One of the tenets of EG is that there is no particle-like dark matter. In the case of a flat universe, the only two contributions to the energy density are baryons and

dark energy (*Ade et al.*, 2016). We can build a toy model for how the baryons should be distributed in EG such that at the core of a virialized system one finds $\sim 100\%$ of the baryons, while in the outskirts the EG baryon fraction falls to the global value of 5-10%. This toy model is shown in figure 2.8 right. If this toy model would describe how the real baryons are distributed in our Universe, we would find a high level of consistency between what we observe with what weak lensing predicts for the dark matter profiles and what EG predicts for the apparent dark matter. This is just a toy model, but it is an example of how one could achieve closer agreement between the EG predictions and the current observations.

2.6.2 Modifying EG

As opposed to reconsidering the distribution of the baryons inside clusters, one could alter the maximal strain of the EG model as described in Section 3 in equation 2.5. Recall that we chose equality in the inequality of the EG model in equation 2.5. We could have chosen some form away from its maximum value. As a new toy model, we propose a modification to the EG model which consists in changing $r'^2 \rightarrow r_0 r'$ in the denominator on the r.h.s. of the equation 2.7. For $r_0 = 1.2$Mpc, the l.h.s. is smaller than its maximum value until beyond this radius. In the case $r_0 = 1.2$ Mpc the result is consistent with the observations (see fig. 2.9). While the modification is based purely on phenomenological ground it might help in developing the theory of the EG model as we can see that the data favor the proposed form instead of the original form 2.7. This results leads to the conclusion that while by default equality is chosen in most of the works related to the testing and development of the EG theory, it is not necessarily the right or only choice.

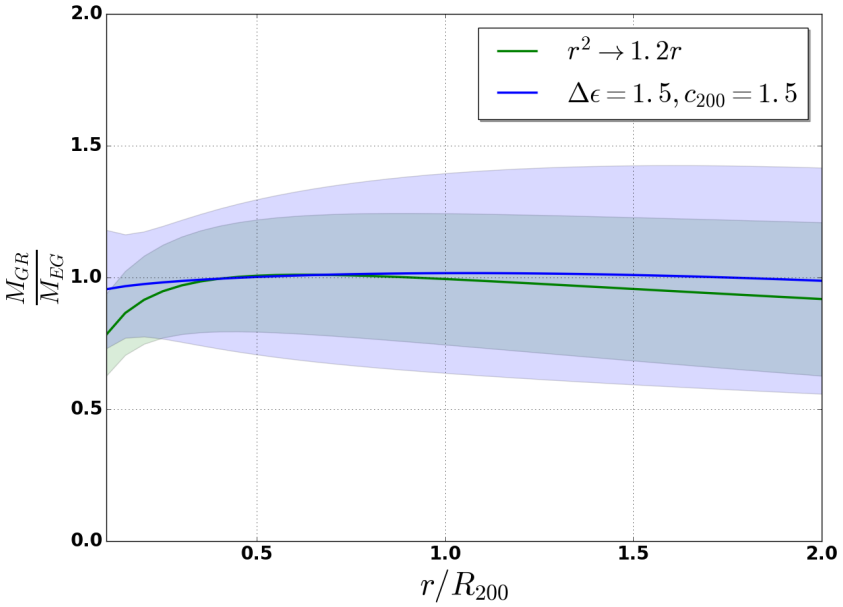

Figure 2.9: The mass ratio $\frac{M_{GR}}{M_{EG}}$ of the observed dark matter (M_{GR}) and the apparent dark matter (M_{EG}). Solid lines and shaded regions are the means and 68.3% error bars around the means. Green color corresponds to the phenomenological modification of EG prediction (see subsection 2.6.2) in the case of substituting r^2 in the denominator of the r.h.s. of the equation 2.7 by $1.2r$. Blue color corresponds to the adjusting both weak lensing data (shifting concentration parameter so it is $c_{200} = 1.5$ for all the data (see subsection 2.5.3 for motivation of this modification)) and baryon matter distribution (increasing steepness parameter by $\Delta\epsilon = 1.5$ for all the clusters (see subsection 2.5.5 for motivation of this modification)). It can be seen that both modifications presented in the figure make EG model to be consistent with the observed data as the mass ratio $\frac{M_{GR}}{M_{EG}} \approx 1$ in the radial region $0.3 \leq r/R_{200} \leq 2$.

2.6.3 Combining Systematics

As it was mentioned in the section 2.5, concentration parameter (c_{200}) of the weak lensing and the steepness parameter (ϵ) could be changed to make EG to be more compatible with the observed data. Moreover, by adjusting both of these parameters at the same time the prediction of the EG model correlates nicely with the observed data (see figure 2.9).

2.7 Conclusions

The first attempt on testing Emergent Gravity was done by *Nieuwenhuizen* (2017), where in contrast to our approach of using only weak lensing in determining matter profiles, combination of strong and weak lensing data (which compliment each other and overall better than weak lensing along determine matter profiles (*Umetsu*, 2013)) of one cluster A1689 showed that EG does not work in the region up to $0.4 - 0.5R_{200}$, while inclusion of neutrinos into EG framework helps to achieve a very good fit. *Brouwer et al.* (2017) showed that the EG model is in good agreement with the galaxy data. *Ettori et al.* (2019) tested the EG theory with 13 clusters in the narrow small redshifts range ($z \approx 0.047 - 0.091$) with reconstructed hydrostatic mass profiles which have non-negligible hydrostatic bias due to non-thermal pressure sources. By analyzing 4 clusters, *ZuHone and Sims* (2019) confirmed conclusion of current manuscript as well as supported results of *Nieuwenhuizen* (2017) that at small radii ($\sim 3 - 100$ kpc), EG produces a bad fit to the data.

In this work, the cluster data set was extended and resulted in utilization of 23 galaxy clusters in wider radial ($0.1R_{200} - 2R_{200}$) and redshift ($0.077 - 0.289$) ranges. In addition to testing the nominal EG model, we consider an extension to the basic predictions of the framework (see also *Hossenfelder* (2017)).

EG provides good results only in the area near the virial radius and by taking into account the cores and the outskirts, the mass profile shape differences allow us to rule out EG at $> 5\sigma$. However, given our current level of systematic errors in the observed shape profiles, our results lead to the conclusion that the EG model is a viable alternative to dark matter in the range $0.3 \leq r \leq 1\mathrm{R}_{200}$. Under the nominal assumptions (i.e., without systematics), EG favors a radially decreasing baryon fraction which peaks in the cluster core (this effect could be slightly amplified due to the BCG not always taking into account by weak lensing data). This is a different baryon fraction profile when compared with the standard dark matter model (see *Ade et al.*

(2016)).

The EG model predicts a flatter shape of the dark matter mass distribution than the observed data, as well as steep X-ray gas density profiles. One of the successes of the model is that the observed weak lensing data and the predicted apparent dark matter are almost identical in the region close to R_{200}.

Finally, we investigate the level of systematic errors needed to reach good agreement between EG and the data. We find that within the current systematic limits, there are combinations of shape profiles which can match EG to the data. Likewise, we investigate whether the EG model itself has the flexibility to better match the data and we find that it does through a lowering of the maximal strain. Given the level of systematic uncertainties in the data, as well as the depth of the theoretical framework, we are unable to formally rule out in the wide region (i.e. in $0.3 \leq r \leq 1\mathrm{R}_{200}$) the EG model as an alternative to dark matter in galaxy clusters.

CHAPTER III

Quantifying the projected suppression of galaxy clusters 3D escape velocity profiles

3.1 Abstract

The radial escape-velocity profile of galaxy clusters has been shown to be a promising and competitive probe of cosmology in an accelerating universe. Projection onto the sky is a dominant systematic uncertainty for statistical inference, since the observed line-of-sight galaxy positions and velocities can suppress the underlying 3D escape-velocity edge. In our work, we utilize Keplerian orbital dynamics to numerically model cluster phase-spaces. We then compare the analytical escape edge to those from N-body simulations. We show that given high enough sampling, the 3D escape velocity edge is in fact observable without systematic bias or suppression with $< 1\%$ accuracy over the range $0 \leq r/r_{200} \leq 1$. In the case of moderate sampling (< 500 galaxies), we model the amount of the edge suppression (Z_v) with $\sim 2\%$ accuracy and $\sim 5\%$ precision for massive ($> 10^{14} M_{\odot}$) systems over the range $0.4 \leq r/r_{200} \leq 1$. The model incorporates observables such as richness and the line-of-sight velocity dispersion. We show that the numerically modeled suppression is independent of velocity anisotropy over the range $-2.5 \leq \beta \leq 0.5$. Finally, we show that suppression is mass and cosmology independent and can be successfully modeled by inverse power-law

$Z_v = 1 + (N_0/N)^\lambda$ with best-fit parameters $N_0 = 14.205, \lambda = 0.467$ (the bottom error bar line: $N_0 = 3.213, \lambda = 0.392$, the top error bar line: $N_0 = 35.822, \lambda = 0.454$) and it is a function of richness only. We conclude that the 3D cluster escape velocity profile can be inferred from projected phase-space data without knowledge of cosmology or the use of simulations.

3.2 Introduction

Galaxy clusters are the most recently formed cosmological objects. Galaxies inside the reach of the potential are sparsely distributed and represent a small fraction of the baryonic content. The majority of the baryons that do exist are in the mostly smooth gaseous intra-cluster medium. In the current ΛCDM paradigm, the cluster potential is dominated by dark matter which does not interact with the member galaxies or the gas. Through the Poisson equation, the cluster potential governs the dynamics of galaxies which have recently undergone (or are still undergoing) gravitational infall. In this scenario, we expect that galaxies which have been accelerated to escape speeds will be largely unaffected by dynamical friction, tidal interactions or encounters with other galaxies (for a review, see *Aguilar* (2008)). Therefore, the escape velocity profile becomes an observable property of clusters representing the underlying potential with few systematics.

The escape velocity profile ($v_{esc}(r)$) of a cluster is a clearly defined edge in the radius/velocity phase space diagram. In 3D, only the galaxies with the maximum possible speed and which are still gravitationally bound to the cluster will contribute to this edge (*Miller et al.*, 2016). The power of utilizing the observed $v_{esc}(r)$ is in its direct connection to the total potential, enabling cluster mass estimations, tests of gravity on the largest scales in the weak field limit, and placing tight constraints on the ΛCDM cosmological parameters (*Gifford and Miller*, 2013; *Gifford et al.*, 2013; *Stark et al.*, 2016b; *Stark et al.*, 2017).

It is difficult to reconstruct cluster 3D phase-space data because we only measure the projected galaxy positions and velocities. Up until now, simulations have always shown that the observed edge is lower than the underlying radial or tangential v_{esc} profile. Because of this, most researchers have utilized N-body simulations to calibrate the amount of suppression of the projected escape velocity profile (*Diaferio and Geller*, 1997; *Diaferio*, 1999; *Serra et al.*, 2011; *Gifford et al.*, 2013). However, *Stark et al.* (2016a) used a novel technique where they combined weak lensing mass profiles and cluster phase-space data to observationally constrain the suppression without simulations. Combined, these studies find a suppression of the 3D escape edge down to the projected edge of about $70\% \rightarrow 80\%$. This is the dominant systematic when using the observed phase-space edge to infer cluster mass profiles or in cosmological parameter estimation.

In this work, we take a new approach to determine the amount of projected escape edge suppression which does not require simulations or weak lensing observations. Our approach is rather simple and is based on populating mock halos with galaxies on Keplerian orbits. While these mock phase-spaces do not contain the full dynamical information of a true massive and fully evolved halo, we show that the 3D and projected phase-space edges accurately and precisely match those of simulations.

The plan of the paper is following. First, we introduce physics of connection of escape velocity profiles with gravitational potentials and cosmological parameters (i.e. motivation of the whole work) as well as we show the math behind projection effects and the way the real systems are observed. In the section 4, we make some observations of conclusions that can be made based on *Diaferio* (1999) approach and show that in theory the actual escape velocity profile can be observed. The section 5 is devoted to deriving Keplerian orbits in a vicinity of a galaxy cluster. We follow with the section where we describe our approach. We spend some time describing simulations against which we test our approach. After that, we show that

the approach indeed works by testing on two sets of simulations as well as we present the suppression function with a proof that is is only a function of the number of galaxies per cluster. We finish with a discussion and conclusions.

For the simulation data a flat standard cosmology with $\Omega_M = 0.25$, $\Omega_\Lambda = 1 - \Omega_M$ and $H_0 = 100h$ km s^{-1} Mpc^{-1} with $h = 1.0$ is assumed. Throughout this chapter we refer to the following quantities R_{200} and M_{200} which are the radius and the mass of the clusters at the point when the density drops to $200\rho_{c,z}$, where $\rho_{c,z} = 3H^2/(8\pi G)$ is the critical density of the universe at redshift z and $H^2 = H_0^2(\Omega_\Lambda + \Omega_M(1+z)^3)$. The connection between R_{200} and M_{200} is by definition the following: $M_{200} = \frac{4\pi}{3}(200\rho_{c,z})R_{200}^3$.

3.3 Motivation

3.3.1 Escape velocity profile in an expanding universe

The main conclusion of general relativity is the Einstein equation which relates matter/energy density to the curvature of space-time *Jacobson* (1995a). Through the Poisson equation, this curvature in-turn governs the dynamical behavior of the local matter. *Nandra et al.* (2012) derived an invariant fully general relativistic expression, valid for arbitrary spherically symmetric systems, for the force required to hold a test particle at rest relative to the central point mass in an accelerating universe. As then also noted by *Behroozi et al.* (2013a), in a ΛCDM universe there is a location in space (r_{eq}) which is well-defined and relative to a massive body (like a cluster), where the radially inward gravitational force acting a tracer from the massive object is equivalent to the effective radially outward force due to the acceleration of the underlying space-time,

$$r_{eq} = \Big(- \frac{GM}{q(z)H^2(z)} \Big)^{1/3}, \tag{3.1}$$

where G is the gravitational constant, M is the mass of the cluster, and the deceleration parameter is $q(z)$.

An important observational consequence of equation 3.1 is in the definition of the escape velocity on cosmological scales. In the Newtonian or weak-field limit where

$$v_{esc} = \sqrt{-2\Phi}, \tag{3.2}$$

Φ becomes the total potential, which includes the gravitational potential (ϕ) as well as the potential in the expanding space-time (*Riess et al.*, 1998; *Calder and Lahav*, 2008). As discussed in (*Behroozi et al.*, 2013a), the radial[1] escape velocity profile is of the following form

$$v_{esc} = \sqrt{-2[\phi(r) - \phi(r_{eq})] - q(z)H^2(z)[r^2 - r_{eq}^2]}. \tag{3.3}$$

Equation 3.3 tells us that the slope of the escape velocity profile runs downward with radius due to the $q(z)H^2(z)r^2$ contribution and also that the overall amplitude of the escape edge shifts downward due to r_{eq}, the latter being the dominant effect. Equation 3.3 was tested to high precision and accuracy (percent level) using N-body simulations (*Miller et al.*, 2016).

3.3.2 From 3D to the Projected Data

In order to infer 3D escape velocity profiles (v_{esc}) of the galaxy clusters from observational data, we need to follow several steps. The first step is to collect the galaxy velocities along line-of-sight (v_{los}) by measuring their redshifts (z_g) as well as

[1]Objects on tangential escape trajectories also have a revised escape velocity, as presented in *Behroozi et al.* (2013a).

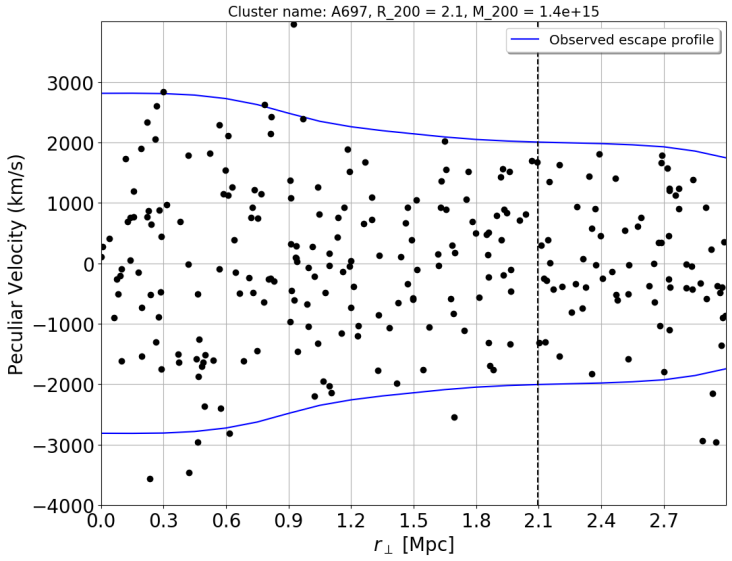

Figure 3.1: Projected phase space, i.e. peculiar velocity [km/s] (v_{los}) vs. radial distance [Mpc] away from the center of the cluster A697. Blue lines are the measured maximum velocity profiles ($v_{los,esc}$). The procedure of inferring $v_{los,esc}$ from positions and redshifts of individual galaxies (black dots) with line-of-sight velocities v_{los} (3.4) and radial distances $r_\perp$ (3.5) is done by finding galaxies which have the top 1% velocities in each of the 0.2 Mpc radial bins. The interloper removal prescription proposed by *Gifford et al.* (2013) is followed. The vertical line is the weak-lensing inferred 3D r_{200}.

the redshift of the cluster center (z_c)

$$v_{los} = c\Big(\frac{(1+z_g)^2-1}{(1+z_g)^2+1} - \frac{(1+z_c)^2-1}{(1+z_c)^2+1}\Big), \tag{3.4}$$

where c is the speed of light and relativistic Doppler effect formula was used ($1+z = \sqrt{\frac{1+v_{los}/c}{1-v_{los}/c}}$).

We then need to infer the galaxy projected radial distances from the center of the cluster ($r_\perp$),

$$r_\perp = r_\theta\Big(\frac{1}{1+z_g}\frac{c}{H_0}\int_0^{z_g}\frac{dz'}{E(z')}\Big), \tag{3.5}$$

where r_θ and $r_\perp$ are angular and radial separations between galaxy and the center of

the cluster[2], $E(z) = \sqrt{\Omega_\Lambda + \Omega_M(1+z)^3}$. By knowing both ($v_{los}$) and ($r_\perp$) we create a projected phase space for each cluster, i.e. v_{los} vs. $r_\perp$ (see an example using real data in Fig. 3.1).

The edge in the projected phase space is the maximum velocity profile (see blue lines on figure 3.1). To infer the underlying escape velocity profiles v_{esc} from the projected phase space edge, we need to understand the effects of projection on the galaxy positions and velocities.

Diaferio and Geller (1997) and *Diaferio* (1999) laid the initial foundations for the projected escape velocity technique using the idea of "caustics" in the 2D phase-space density. They worked in potential units, such that they were using the observed escape velocity to infer the square of the escape velocity profile. Thus, the underlying premise involves a geometric projection of the classic anisotropy parameter, β. Formally, the velocity anisotropy is

$$\beta = 1 - \frac{\sigma_\theta^2}{\sigma_r^2}, \tag{3.6}$$

where σ_θ and σ_r are tangential and radial velocity dispersions. In general, dispersion

$$\sigma^2(r) =< v^2(r) >, \tag{3.7}$$

where $v(r)$'s are velocities of individual galaxies measured with respect to zero (i.e. to the cluster frame of reference) and the average $< \cdot >$ is over all the galaxies inside a radial bin at r with a width Δr that gravitationally bound to the galaxy cluster. Using simple geometric arguments, Diaferio posits the following relation between the l.o.s. and 3D escape velocity of a cluster:

$$\langle v_{esc,los}^2 \rangle(r) = \frac{(1-\beta(r))}{(3-2\beta(r))} \langle v_{esc}^2 \rangle(r) = (g(\beta(r)))^{-1} \langle v_{esc}^2 \rangle(r) \tag{3.8}$$

[2]We assume that with a large enough galaxy sample in the phase-space data ($\sim$ 100 galaxies), or with ancillary X-ray data, the cluster center can be well determined. Clusters which show signs of mergers or other significant substructure can be excluded from this type of scientific analysis.

This premise suffers from an important statistical issue that was never tested in simulations. The problem lies in the fact that it is based on projected dispersions averaged over projected radii (see Figure 3.2). The dispersion measured in the small box **B** is not the same as that of the dispersion measured through the integrated line-of-sight. By necessity of monotonic potentials, the dispersions in boxes **A** and **C** must be smaller than at **B**. Therefore, a simple average over the line-of-sight is not valid.

As another approach in considering validity of equation 3.8, consider a highly sampled phase space (e.g., of dark matter particles). With enough sampling, one would surely identify a tracer near the escape speed with its velocity perfectly aligned with the line-of-sight and with a projected radius identical to the 3D radius (i.e., position **K** in Figure 3.2). In this case, one could observe the full 3D escape speed at the radius regardless of the radially averaged anisotropy of the underlying system, because the maximum possible velocity of any other tracer along the l.o.s. must necessarily be less than (or equal to) the velocity of this special tracer see Figure 3.3.)

Instead of equation 3.8, we posit that the projected l.o.s. escape profile is dependent solely on the sampling of the phase space. We test this using the Millennium simulation data (see details in Section 3.7). In Figure 3.13, we show how we can in fact recover the full 3D escape velocity given proper sampling. In the next section, we propose a new analytical model to determine the projection term which suppresses $v_{los,esc}$ compared to the underlying v_{esc}.

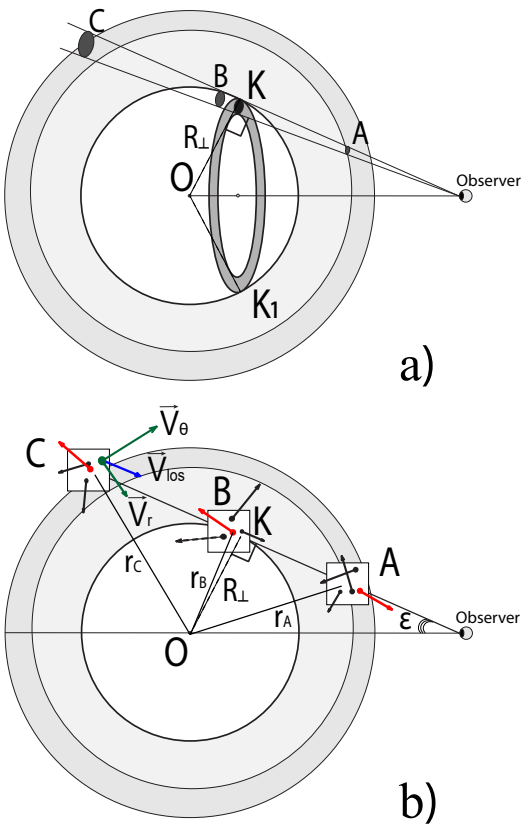

Figure 3.2: Figure a). While in reality the areas A, B and C are spatially separated, for the outside observer they have the same position on the sky. The grey ring KK_1 represents the area which is equally separated from the center of the cluster O. Any galaxy in this ring as well as on the sphere KK_1 will be in the grey band $R_\perp$ on the 3-dimensional phase space on figure 3.3a. All the galaxies in the cone which is created by circling the line of sight AC around the ring KK_1 (we call this cone as $ACKK_1$ cone in the text) will be in the grey band $R_\perp$ on figure 3.3. Figure b). Arrows represent velocities of individual galaxies. Black (red) arrows are the galaxies with velocity directions not aligned (aligned) with the line of sight AC. Any vector velocity of a galaxy (see formula 3.9) is a sum of tangential, radial (green arrows in the box C) and azimuthal (not presented due to direction pointing in/out of the plane of the figure) velocity components. The magnitude of the line of sight velocity (blue arrow in the box C) can be expressed in term of tangential and radial components (see equation 3.10). The angle ϵ between the line of sight AC and the line which connects the center of the cluster O and the observer while represented big is small in reality due to the distance from observer to the cluster much larger in comparison to the size of a cluster. The distances between different points: $OC = r_C, OB = r_B, OK = R_\perp$ and $OA = r_A$. $OK \perp AC$.

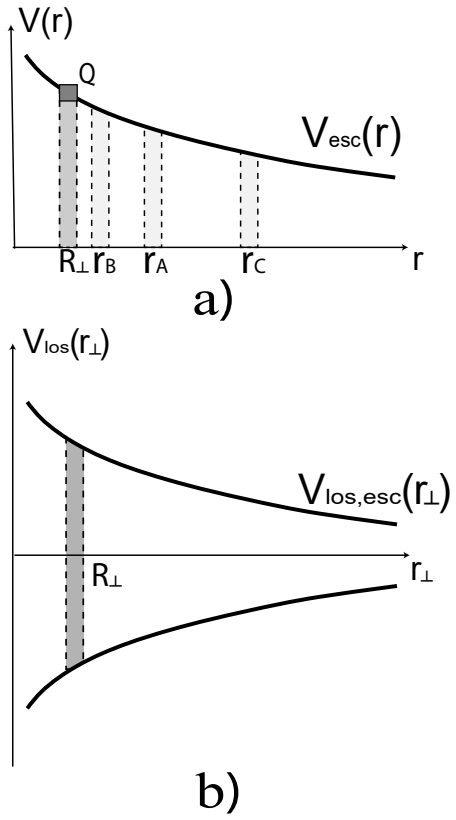

Figure 3.3: Figure a). Phase space, i.e. peculiar velocity [km/s] vs. distance r [Mpc] away from the center of the cluster. $v_{esc}(r)$ line is a measure of gravitational potential (see formula 3.2). Grey bands r_B, r_A and r_C represent areas on the phase space where galaxies from dark small ellipses (figure 3.2a) and boxes (figure 3.2b) B, A and C would be observed. Box Q represents area, where all the galaxies with $v_{esc}(R_\perp)$ from the thin shell with radius $R_\perp$ and center O would be observed on the phase space. Figure b). Observed phase space, i.e. observed peculiar velocity [km/s] vs. radial distance $r_\perp$ [Mpc] away from the center of the cluster. $v_{los,esc}(r_\perp)$ lines are the maximum observed velocities which can be obtained by taking partial derivative (3.12). Similarly, blue lines on figure 3.1 are observed maximum velocities in the real cluster Abell 697. The grey band $R_\perp$ represents where galaxies from the ellipses (figure 3.2a) and the boxes (figure 3.2b) B, A and C would be observed on the observed phase space. Note, while phase space on the figure a) is always positive (presenting absolute value of velocity relatively to the center of the cluster), observed phase space can be negative as well due to galaxy velocities being able to point towards and away from the observer.

3.4 General approach

3.4.1 Relative position

From the prospective of the outside observer many galaxies in the same cluster are at the same distance. Some of the galaxies are physically closer to the observer (arrows in the box A in figure 3.2b), some further away from the observer (box C) and some are somewhere at an intermediate distance (box B). At the same time, galaxy's physical distances relatively to the center of the cluster (point O) are not the same $r_B < r_A < r_C$ (see figure 3.2) and that can be depicted on the physical phase space diagram (figure 3.3a), i.e. on the plot of the full 3-dimensional peculiar velocity $v(r)$ vs. physical distance in relation to the center of the cluster r. However, for the outside observer the relative position of all the boxes (i.e. A, B and C) in respect to the center of the cluster (point O) are the same and equal to $OK = R_\perp$ (see figure 3.3b). This observation means that all the galaxies in the cone which is created by circling the line of sight AC around the ring KK_1 (we will call this cone as $ACKK_1$ cone below) are depicted in the narrow range $R_\perp$ on the phase space diagram (figures 3.2a and 3.3).

3.4.2 The maximum observed velocity

The total velocity can be written down in terms of 3 individual vector components

$$\vec{v}(r) = \vec{v}_\theta(r) + \vec{v}_\phi(r) + \vec{v}_r(r), \tag{3.9}$$

where $\vec{v}_\theta(r)$, $\vec{v}_\phi(r)$ and $\vec{v}_r(r)$ (see green vectors on figure 3.2b) are tangential, azimuthal and radial component of the total velocity $\vec{v}(r)$.

The projected component of the $\vec{v}(r)$ along line of sight (see blue vector on figure 3.2b)

$$v_{los}(r_C) = v_\theta(r_C)\cos(\frac{\pi}{2} - \measuredangle OCB) - v_r(r_C)\cos\measuredangle OCB, \tag{3.10}$$

where r_C is the actual distance between point C and the center of the cluster O.

In general, expression 3.10 can be written down in terms of $R_\perp$ (the radial separation between galaxy at the point C and the center of the cluster)

$$v_{los}(r, r_\perp) = v_\theta(r)\frac{r_\perp}{r} - v_r(r)\frac{(r^2 - r_\perp^2)^{0.5}}{r}, \tag{3.11}$$

where r_C ($R_\perp$) has been substituted by r ($r_\perp$) so the formula can be applied to any galaxy.

The maximum observed velocity $v_{los,esc}$ is what we actually get from observations (see blue lines on figure 3.1). In order to get this maximum $v_{los,esc}$ at $r_\perp$ we need to calculate the maximum value of equation 3.11 by taking partial derivative

$$\frac{\partial v_{los,esc}(r, r_\perp)}{\partial r} = 0. \tag{3.12}$$

The maximum observed velocity ($v_{los,esc}$) is a function of both v_r and v_θ. In general, as it was noted in *Diaferio* (1999), this maximum is at some $r = r_M$ which could differ from $r_\perp$.

3.4.3 Connection between v_{esc} and $v_{los,esc}$

Generally, there are many galaxies in the boxes A, B and C (see figure 3.2b). Some small number of these galaxies will have a velocity which is closely aligned with the line of sight. An even smaller number will be in their orbits such that their 3D velocity is at the escape speed. And yet an even smaller number will have their 3D radius at the same location as the projected radius. In other words, for all of the galaxies along the l.o.s. in Figure 3.2, few will be the red line at position **K**. The other concern is whether any galaxy could have v_{los} higher than the escape speed at any projected radius. We address these concerns analytically in the next few subsections.

Let's define several parameters. The galaxy's velocity will be changing throughout

its orbit. For elliptical orbits, the highest speed is reached at perihelion and the slowest at aphelion. Therefore, we define a parameter to represent the ratio of velocity of the galaxy to its escape velocity

$$\alpha(r) = \frac{v_g(r)}{v_{esc}(r)}, \tag{3.13}$$

where $0 \leq \alpha(r) \leq 1$ and $v_g(r)$ is the full 3-dimensional velocity of the galaxy.

We also define the ratio of radial component to the tangential component of the velocity

$$\gamma(r) = \frac{v_r(r)}{v_\theta(r)}. \tag{3.14}$$

It should be noted that we treat our galaxies as having zero azimuthal velocity component. One could always shift the coordinate frame accordingly to accomplish this.

Using the above parameters we can express v_{los} (eq 3.11) in terms of v_{esc}. First, we need to define tangential and radial components in terms of these parameters and $v_{esc}(r)$

$$v_\theta(r) = \frac{\alpha(r) v_{esc}(r)}{\sqrt{\gamma^2(r)+1}}$$
$$v_r(r) = \frac{\alpha(r)\gamma(r) v_{esc}(r)}{\sqrt{\gamma^2(r)+1}}.$$

And we are ready to write down the expression of our interest

$$v_{los}(r, r_\perp) = \frac{\alpha v_{esc}}{\sqrt{\gamma^2+1}} \frac{r_\perp}{r} - \frac{\alpha\gamma v_{esc}}{\sqrt{\gamma^2+1}} \frac{(r^2 - r_\perp^2)^{0.5}}{r}, \tag{3.15}$$

where α, γ and v_{esc} are all functions of r. To simplify analysis, from now on we treat α and γ as constants.

As one can notice, $\alpha(r)$ is simply a factor to v_{los} and so we can apply the maximum value $\alpha(r) = 1$ throughout our analysis. This allows us to focus only on the $\gamma(r)$ parameter.

One might notice the similarity between $\gamma(r)$ and anisotropy parameter: both β and γ describe the ratio of velocity components. However, they differ in the fact that anisotropy parameter describes the averages of squares of velocity components, while $\gamma(r)$ describes individual galaxies by simply taking the ratio of velocity components. Connecting these two variables is possible only in special cases, such as for a constant $\gamma(r)$), which allows us to drop averages in equation 3.7 such that

$$\beta_{esc}(r) = 1 - \frac{v_\theta^2(r)}{v_r^2(r)} \equiv 1 - \gamma^{-2}(r). \tag{3.16}$$

3.4.4 Predictions for a Single Galaxy

In Figure 3.4 we inspect equation 3.15 for a cluster with an Einasto density profile with a galaxy moving at the escape speed in 3D. We consider three values for γ: 0.1, 1 and 100 which correspond to tangential, isotropic, and radial motion. These lines are the colored curves increasing in their value with increasing γ. We identify three lines-of-sight: 0.01, 0.5, 1.5 projected Mpc corresponding to the blue, green, and red curves. The vertical lines represent the two maxima of each set of curves. From this we can conclude that the highest velocity galaxies observed at the core have $r_\perp = r_{3D}$ and $v_{los} = v_{3D} = v_{esc}$ when their motion is either purely radial or purely tangential. In the virial region, only galaxies on tangential orbits have $v_{los} = v_{3D} = v_{esc}$ and it only occurs when $r_\perp = r_{3D}$.

Figure 3.4 can also explain the general trumpet shape phase-space density profile. The outer envelope is defined purely by the Einasto parameters and cosmology. The multiple escape-speed galaxies which would populate the phase-space lie within this envelope, with most having l.o.s. velocities lying within $v_{los}/\sqrt{2}$ envelope. We will come back to this later.

The three colored stars on Figure 3.4 are important, as they represent galaxies

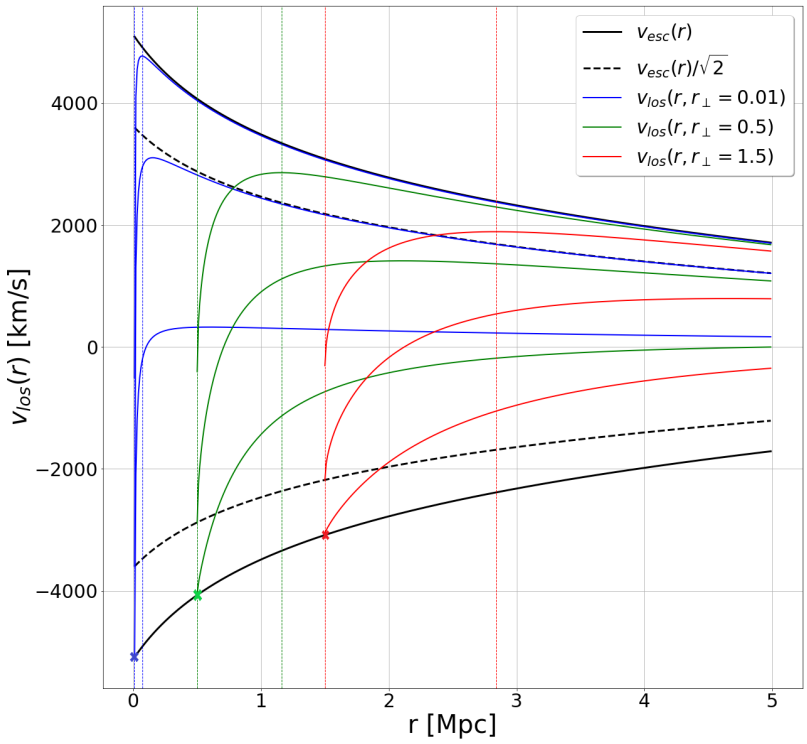

Figure 3.4: The projected escape velocity (colored curves) of a galaxy moving at the full 3D escape speed versus a 3D (black curves) location in its orbit. γ ranges from 0.1, 1 and 100 which corresponds to tangential (lowest curve), isotropic (middle curve), and radial (upper curve) motion. The lines-of-sight range from 0.01, 0.5, to 1.5Mpc corresponding to the blue, green, and red curves. The vertical lines represent the two maxima of each set of colored curves. We can conclude that the highest velocity galaxies observed at the core have $r_\perp = r_{3D}$ and $v_{los} = v_{3D} = v_{esc}$ when their motion is either purely radial or purely tangential. In the virial region, only galaxies on tangential orbits have $v_{los} = v_{3D} = v_{esc}$ and it only occurs when $r_\perp = r_{3D}$.

which would appear on a phase space having both the true underlying 3D radius and velocity, even though they are measured in projection.

Suppose we now sample a "mock" galaxy cluster phase space from Figure 3.4 with lots of galaxies, each with the same γ. We show how such a mock cluster's observed line-of-sight maximum velocity profile would look in Figure 3.5. To facilitate the interpretation, we map the γ's to the typical velocity anisotropy β via equation 3.16. We stress that this is not representative of any real system, since we forced every

galaxy to have the same ratio between its radial and tangential velocity. However, the trends are enlightening. As noted in Figure 3.4, galaxies with tangential orbits would enable a direct measure of the 3D escape velocity edge, regardless of the projected viewpoint from Earth. Galaxies on radial orbits will always lie below the 3D escape velocity, except in the extreme case of $\beta = 1$ and in the innermost core. However, the most important trend in this figure is for $\beta = 0$, which is around the average value for clusters observed in simulations and in the real Universe. In this case, the maximum line-of-sight velocity is near $v_{esc}/\sqrt{2}$. This suppression of the observed escape edge is near the value we have measured in data and in simulations as mentioned in the Introduction 3.2.

We stress again that Figure 3.5 is not representative of any real cluster and does not imply that there is an inherent relationship between the maximum observed line-of-sight velocity and a cluster's anisotropy profile measured through averaging the velocity dispersion components. There mere existence of galaxies on tangential orbits is what sets the phase-space edge, which is clarified in Figure 3.4 and which we address further in the next section. The treatment in this section is simple, and so we move to a more realistic cluster with Keplerian orbits and then we populate the clusters with the full variety of galaxies in their orbital locations and velocity vectors.

3.5 Keplerian Orbits

In this section, we move to a much more realistic cluster with orbital parameters that represent a physical reality. We utilize the vis-viva equation which has a rather simple expression for the orbital velocity of a tracer around a central point mass

$$v(r)^2 = GM\Big(\frac{2}{r} - \frac{1}{a}\Big), \tag{3.17}$$

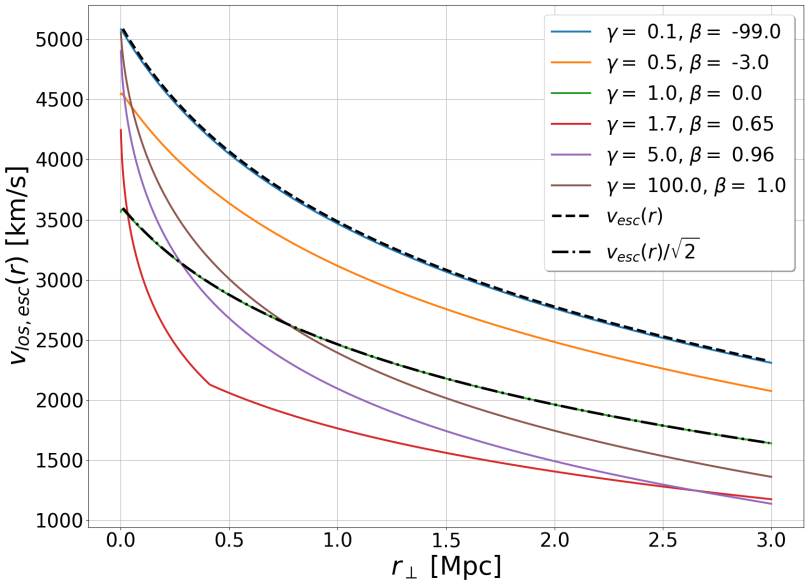

Figure 3.5: A representation of mock phase space showing the observed maximum line-of-sight velocity versus the projected radius for galaxies moving at the 3D escape speed. This is not a realistic system, since all galaxies have a fixed $\gamma(r)$ which can then be mapped to the velocity anisotropy parameter β_{esc}. In the case where all galaxies are on tangential orbits $\beta = -99$, the projected maximum velocities will populate the 3D escape velocity profile. Galaxies with radial orbits never populate $v_{esc}(r)$, except in the inner core. Galaxies with "isotropic" motion populate the region around $v_{esc}/\sqrt{2}$, which is about the same level of suppression observed in simulations and in real data.

where G is gravitational constant, M is a mass of a point mass, r is a distance of an object from the central point mass and a is a semi-major axis of the object's orbit.

While the central point mass is a good starting point, it is rather unrealistic for the type of systems we work with. To properly describe the total physical velocity of a galaxy, we need to derive the vis-viva equation in the framework of an extended mass and with cosmological background.

We use the the semi-major axis (a) and semi-minor axis (b) as parameters to describe ellipses. However, it is easier to derive velocity equations in a non-point-like central mass gravitational field using apsides (minimum (r_{min}) and maximum (r_{max})

distances from the focus to the ellipse, i.e. the elliptical orbit of the galaxies). By definition

$$a = \frac{r_{min} + r_{max}}{2},$$
$$b = \sqrt{r_{min} r_{max}}.$$

Using these two definitions, we can express

$$r_a \equiv r_{min} = \frac{b^2}{a + \sqrt{a^2 - b^2}}, \tag{3.18}$$
$$r_p \equiv r_{max} = a + \sqrt{a^2 - b^2}. \tag{3.19}$$

To find the total velocity of a galaxy on elliptical orbit we follow the nominal steps used in the derivation of the vis-viva equation. We know that the total energy is a conserved quantity, i.e. $E/m = \frac{v(r)^2}{2} + \Phi(r) = const.$ We can write this expression for both r_a and r_p

$$\frac{v(r_a)^2}{2} + \Phi(r_a) = \frac{v(r_p)^2}{2} + \Phi(r_p).$$

Using conservation of angular momentum ($r_a v(r_a) = r_p v(r_p)$) and adding to both sides $\Phi(r_a)$

$$\frac{v(r_a)^2}{2} + \Phi(r_a) = (\Phi(r_p) - \Phi(r_a)) \frac{r_p^2}{r_p^2 - r_a^2} + \Phi(r_a). \tag{3.20}$$

Due to the energy conservation, we can rewrite the above expression for any radial distance by substituting r_a by r

$$E/m = \frac{v(r)^2}{2} + \Phi(r) = (\Phi(r_p) - \Phi(r_a)) \frac{r_p^2}{r_p^2 - r_a^2} + \Phi(r_a), \tag{3.21}$$

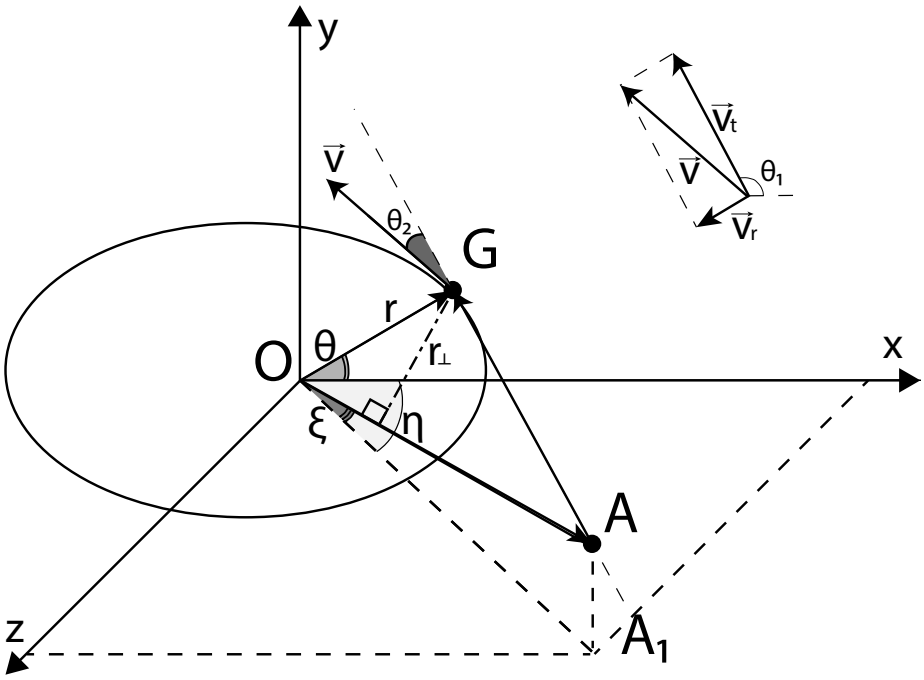

Figure 3.6: Schematic description of the projected view of the galaxy G by observer A. xyz coordinate system is chosen, so that an elliptical orbit of the galaxy G is placed on xy plane. A_1 is the projected position of the observer on xz plane, O is the center of coordinate system xyz and the center of the cluster, which is in the focal point of the elliptical orbit of the galaxy G. θ is the angle between the line OG and x-axis and describes position of the galaxy on its orbit, η is the angle between the line OA_1 and x-axis, ξ is the angle between the lines OA and OA_1. η and ξ describe relative position of the observer and the orbit of a galaxy. $r = OG$, the physical distance between center of the cluster O and galaxy G, is $\geq r_\perp$, where $r_\perp$ is projected distance between galaxy G and the center O along line of sight OA, i.e. $r_\perp$ is the distance between O and G as seen by observer A. $R = OA$ is the distance between observer and the center of the cluster.

where on the right hand side we have a constant which depends on the semi-major and semi-minor axes.

The total velocity is then a function of r and can be derived from 3.21

$$v = \sqrt{2(P - \Phi(r))}, \tag{3.22}$$

where $P = (\Phi(r_p) - \Phi(r_a))\frac{r_p^2}{r_p^2 - r_a^2} + \Phi(r_a)$. In the case of high ellipticity (i.e. $r_p \gg r_a$) $P \to \Phi(r_p)$, which is the same case as for a point mass (equation 3.17).

The total dynamical potential $\Phi(r)$ is a function of both the mass distribution and cosmology. Overall, it can be derived from expressions 3.2 and 3.3

$$\Phi(r) = \phi(r) - \phi(r_{eq}) + \frac{qH^2[r^2 - r_{eq}^2]}{2}, \tag{3.23}$$

where $\phi(r)$ is described by Einasto model (*Einasto*, 1965)

$$\rho_e(r) = \rho_0 \exp\left[-\left(\frac{r}{r_0}\right)^{1/n} \right]. \tag{3.24}$$

By using integral form of the Poisson equation, gravitational potential can be derived (*Retana-Montenegro et al.*, 2012)

$$\phi_e = -\frac{\mathrm{GM}}{r}\left[1 - \frac{\Gamma\left(3n, \left(\frac{r}{r_0}\right)^{1/n}\right)}{\Gamma(3n)} + \frac{r}{r_0}\frac{\Gamma\left(2n, \left(\frac{r}{r_0}\right)^{1/n}\right)}{\Gamma(3n)}\right], \tag{3.25}$$

where ρ_0, r_0 and n are the parameters of the Einasto model and $\Gamma(a,b) = \int_b^\infty t^{a-1}e^{-t}dt$ is an incomplete gamma function. We use the Einasto model instead of other models such as NFW (*Navarro et al.*, 1996, 1997), since it correctly predicts escape velocity profiles in full N-body simulated halos (*Miller et al.*, 2016).

3.5.1 Keplerian orbits from a distant observer's point of view

To find the phase space in a projected view, we need to derive the projected distance between a galaxy and the center of a cluster and the projected velocity as seen by the observer. To assist in the derivation, we refer the reader to the schematic representation of the geometry in Figure 3.6.

3.5.1.1 Projected distance

To find the expression for the projected distance $r_\perp$ as seen by the observer (see figure 3.6), we need to find x - distance from the center of the cluster O and the point

of intersection of perpendicular from the point G on OA and OA itself.

The position of the observer in terms of the spherical coordinates is

$$x_A = R\cos\xi\cos\eta$$
$$y_A = R\sin\xi\cos\eta$$
$$z_A = R\sin\eta.$$

The position of the galaxy is

$$x_G = r\cos\theta$$
$$y_G = r\sin\theta$$
$$z_G = 0,$$

where in this derivation we have placed the galaxy in the $x-y$ plane.

Knowing the distance from the observer to the galaxy

$$r_{AG} = \sqrt{(x_A - x_G)^2 + (y_A - y_G)^2 + (z_A - z_G)^2} \tag{3.26}$$

and using the fact that $r_\perp$ is perpendicular to OA

$$r_\perp^2 = r^2 - x^2 = r_{AG}^2 - (R - x)^2,$$

we can find the expression for the x distance

$$x = \frac{R^2 + r^2 - r_{AG}^2}{2R}.$$

From Pythagorean theorem the projected distance is then

$$r_\perp = \sqrt{r^2 - x^2}. \tag{3.27}$$

3.5.1.2 Projected velocity

To derive the projected velocity of a galaxy, we need to know the angle between the total velocity vector (3.22) and the vector that connects the observer and the galaxy, i.e. $\overrightarrow{AG}$ in figure 3.6. Using this angle, we can project the total velocity on the line of sight.

We start with deriving velocity vector $\vec{v}$. In order to do that we need to know tangential and radial components of the total velocity 3.22. We enforce the conservation of angular momentum

$$L \equiv r v_t(r) = r_a v_a(r_a), \tag{3.28}$$

where we used the fact that at the apsides the radial component of the velocity is zero. From equation 3.28 we get the tangential velocity component as a function of angle θ

$$v_t(\theta) = (1 + e\cos\theta)\sqrt{\frac{\phi(r_p) - \phi(r_a)}{p(r_p - r_a)}}, \tag{3.29}$$

where we used the expression of a distance

$$r(\theta) = p/(1 + e\cos\theta) \tag{3.30}$$

and introduced parameter $p = b^2/a$ and eccentricity

$$e = \sqrt{1 - (b/a)^2}. \tag{3.31}$$

Note, that from now on we use the angle θ (see figure 3.6) as the main parameter that characterizes the position of the galaxy in its orbit. For elliptical orbits, $\theta = 0$ represents the galaxy at its minimum distance from the focus or perihelion (r_a) and

$\theta = 0$ represents the galaxy at aphelion (r_p).

The radial component of the total velocity (eq. 3.22) is

$$v_r(\theta) = \sqrt{v(\theta)^2 - v_t(\theta)^2}, \tag{3.32}$$

where the total velocity is a function of the angle θ instead of the distance r, which is done by using equation 3.30.

By knowing the lengths of the individual components of $\vec{v}$, we can determine an expression for $\vec{v}$ in the xyz coordinate system. $\vec{v}_r$ is on the line OG and it is pointing towards O. Using coordinates of the point G (see subsection 3.5.1.1)

$$\vec{v}_r = [v_r \cos\theta, v_r \sin\theta, 0], \tag{3.33}$$

where the magnitude v_r is expressed in equation 3.32.

Since both $\vec{v}$ and $\vec{v}_r$ have zero z component, we can present vector $\vec{v}_t$ in terms of the magnitude of the v_t and some angle θ_1, i.e. $\vec{v}_t = [v_t \cos\theta_1, v_t \sin\theta_1, 0]$. Knowing that $\vec{v}_t$ is perpendicular to $\vec{v}_r$, we can find θ_1 by taking the scalar product $\vec{v}_t \cdot \vec{v}_r$, which is equal to zero due to the perpendicularity of two vectors. After doing some straightforward calculations, one can show that

$$\theta_1 = \arctan(-\cot\theta). \tag{3.34}$$

Finally, we arrive at an expression for the vector description of the total velocity

$$\vec{v} = [v_t \cos\theta_1 + v_r \cos\theta, v_t \sin\theta_1 + v_r \sin\theta, 0], \tag{3.35}$$

where angle θ_1 is a function of the angle θ and the magnitudes of v_t and v_r are expressed in equations 3.29 and 3.32 respectively.

Vector $\overrightarrow{AG}$ can be expressed using coordinates of points A and G (see subsection 3.5.1.1)

$$\overrightarrow{AG} = [r\cos\theta - R\cos\xi\cos\eta, r\sin\theta - R\sin\xi\cos\eta, -R\sin\eta]. \tag{3.36}$$

Projection of the vector $\vec{v}$ on $\overrightarrow{AG}$ can be found using expression of the angle (we call it θ_2) between the two vectors (i.e. $\cos\theta_2 = \frac{\vec{v}\overrightarrow{AG}}{|\vec{v}||\overrightarrow{AG}|}$). We then arrive at our final expression of the velocity along line-of-sight, which is

$$v_{los} = \frac{\vec{v}\overrightarrow{AG}}{|\overrightarrow{AG}|}. \tag{3.37}$$

3.5.2 Energy ratio for Keplerian Orbits in an Extended Mass Profile

Later, will show that the ratio between a galaxy's kinetic to potential energy places constraints on the maximum possible observed line-of-sight velocity. For a point mass, this ratio is simply 1/2 in a virialized orbital system (*Eddington*, 1916). To derive the ratio between the kinetic to potential energy for an extended mass source, we start with the force balance equation

$$-\frac{d\phi}{dr} = \frac{v^2}{r}, \tag{3.38}$$

where we cancelled the mass of the tracer, m. By definition, kinetic energy per unit mass is $k = v^2/2$. To find a simple analytical expression for ϕ, instead of the bulky Einasto potential (3.25), we use the expression for the NFW potential (*Navarro et al.*, 1996)

$$\phi(r) = -\frac{4\pi G\rho_0(r_0)^2\ln(r/r_0+1)}{r/r_0} = -\frac{c\ln(r/r_0+1)}{r}, \tag{3.39}$$

where c is a constant. ρ_0 and r_0 are parameters of the model. Taking the derivative with respect to r, we find the following expression for kinetic energy

$$\frac{d\phi}{dr} = \frac{c\ln(r/r_0+1)}{r^2} - \frac{c/r_0}{r(r/r_0+1)}. \tag{3.40}$$

Note that a point mass does not have the *log* contribution, i.e. no second term in derivative and no ln in the first term in derivative: $d\phi/dr = c/r^2$. From here we can get expression for kinetic energy

$$k = -0.5\Big(\frac{c\ln(r/r_0+1)}{r} - \frac{c/r_0}{r/r_0+1}\Big). \tag{3.41}$$

The ratio of the kinetic to potential energy in the NFW case without a cosmological background is then

$$\frac{k}{\phi} = \frac{1}{2} - \frac{1}{2\ln(r/r_0+1)}\frac{1}{1+r_0/r}. \tag{3.42}$$

Compared to a point mass, for the extended mass distribution the ratio is not a constant ($\frac{1}{2}$), but is a function of r/r_0. Moreover, we can notice that the energy ratio for the NFW profile is smaller than for the point mass source due to the negative second term in equation 3.42. *Łokas and Mamon* (2001) evaluated this ratio in the context of the Jeans equation for an entire cluster and a given anisotropy profile. Our context is much different, with a focus on individual galaxy orbits. In what follows, we also require a cosmological background.

3.5.3 Energy ratio in a Cosmological Background

To incorporate cosmology we change from the gravitational form ϕ to the total potential Φ using equation 3.23

$$u(r) = -\frac{v_{esc}}{2} = \phi(r) - \phi(r_{eq}) + \frac{q(z)H^2(z)[r^2 - r_{eq}^2]}{2}. \tag{3.43}$$

We can then express the energy ratio

$$\frac{k}{u} = \frac{P - u(r)}{u(r)} = \frac{\frac{u(r_p)}{u(r)} r_p^2 - \frac{u(r_a)}{u(r)} r_a^2}{r_p^2 - r_a^2} - 1, \tag{3.44}$$

where r_a and r_p are functions of minimum (perihelion) and maximum (aphelion) distance from the center of the cluster to the galaxy on an elliptical orbit (equation 3.18).

We show the energy ratio in Figure 3.7 for a galaxy with an perihelion distance of 1Mpc and on various orbits with different eccentricities. We show four locations in the galaxy's orbit with 0 degrees at perihelion (top left) and approaching aphelion at 180 degrees. We note that there is a maximum allowed eccentricity, which is a function of the perihelion distance r_a and due to the ratio v_{tot}/v_{esc} being lower for smaller e. The consequence of equation 3.1 in an accelerating space-time is that galaxies with orbits that take them beyond r_{eq} will escape. The reader can ignore the energy ratio beyond this maximum eccentricity in Figure 3.7, where our formalism becomes meaningless.

Figure 3.7 is quite informative. We notice that the extended density profile lowers the energy ratio. We also see that in a non-accelerating space-time, galaxies cannot escape the cluster (i.e., requiring an energy ratio > 1). Adding in the acceleration term changes the potential by lowering it and thus raising the energy ratio. As a galaxy just above a ratio of one at perihelion approached aphelion, it ends up with an energy ratio that enables escape. This does not mean that the galaxy's is sped

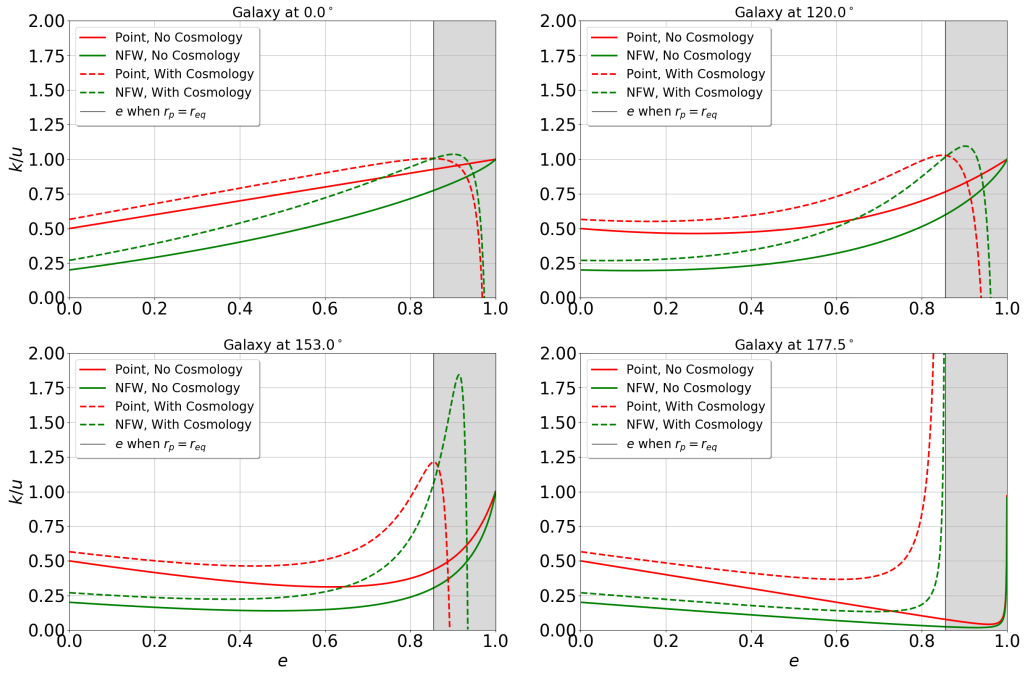

Figure 3.7: The ratio of kinetic (k) to potential (u) energy as a function of eccentricity for a mock cluster and fixed perihelion distance of $r_a = 1$Mpc. Galaxies with ratios near one will populate the escape edge of a cluster phase-space and those even slightly above one will escape at some point. The gray band delimits the eccentricity such that galaxies with those orbits will gain enough energy to escape from the system and so the ratio can be ignored. The extended density profile lowers the ratio while adding in an accelerating space-time raises the ratio. The top left plot shows the galaxy at perihelion, where it is moving the fastest where eccentricities above ~ 0.8 will enable future escape. As the galaxy approaches aphelion (180 degrees), we see that those galaxies with the highest eccentricities can reach ratios such that they escape. As we increase (decrease) the perihelion distance the gray band moves left (right), but the curves remain the same. This implies that we will have fewer galaxies to populate the escape edge in cluster outskirts (i.e. near aphelion).

up during its orbit which would be unphysical. It simply means that an accelerating space-time changes the energy boundary for escape. The effect is amplified with the shape of the orbit, such that radial orbits are more likely to escape.

Figure 3.7 explains what previous researchers have characterized about particles escaping a cluster in simulations. *Behroozi et al.* (2013a) found that kinetic and potential energies are a poor predictor of escape and that orbits matter. They also found that the mass fraction of unbound particles increases towards the edges of halos and decreases significantly at higher redshifts. Our analytical approach can explain each of these findings. *Miller et al.* (2016) showed that the phase space dynamical radial escape edge in simulations requires a potential of the form in equation 3.43, i.e. that particles must have escaped over time as acceleration kicks in. They also show that this effect becomes lessened with increasing redshift. Again, both of these findings can be explained by considering the energy ratio for a galaxy inside an extended mass profile having a Keplerian orbit.

Finally, we return to our main purpose of observing v_{esc}. Figure 3.7 shows that galaxies moving at their escape speeds will be near their perihelion. If we re-make the orbits using a galaxy with a smaller r_a (perihelion distance), the gray band will shift to right and then our system can have galaxies with higher eccentricities and those galaxies can populate the escape edge. On the other hand, as the perihelion distance of a galaxy increases, the gray band moves towards smaller eccentricities and a galaxy is less able to ever reach escape speeds. This places a constraint on the v_{esc} that we are able to actually observe. A galaxy with a large perihelion distances and which lives in the outskirts will populate the region below the escape edge in the radius/velocity phase-space, but not contribute to it.

3.5.3.1 Observed Velocities for Galaxies on Elliptical Orbits

In the previous subsection we showed that some galaxies inside an extended mass profile having Keplerian orbits within a cosmological background can populate the escape edge of the radius/velocity phase space. The question remains as to whether this velocity is observable given the line-of-sight projection. In this subsection we focus on the case with zero azimuthal velocity component ($\eta = 0$ on figure 3.6) and consider observer's line of sight being parallel to the orbit of the galaxy. This allows us to focus on the maximum possible observed velocity.

We first note that for the distances between the galaxy and the observer, which are large enough to allow for the use of small-angle approximation, the specific choice of distance does not matter. We then require a new angle, which is the orientation of the semi-major axis of the galaxy's orbit with respect to the observer. In Figure 3.6, this is noted as ξ, where $\xi = 0$ is the semi-major axis aligned with the line-of-sight and $\xi = \pm 90$ perpendicular to the line-of-sight. In both cases, the observer is aligned with the focus of the ellipse.

In Figure 3.8, we plot the escape velocity, the galaxy total velocity in 3D, and the observed line-of-sight velocity as a function of the orbit location for two eccentricities and from two viewing angles. Galaxies with low eccentricity never reach escape speeds whereas for high eccentricity they do. This is consistent with Figure 3.7. When the semi-major axis is aligned along the line-of-sight (left and middle panels), there are many regions in the orbit where the observed v_{los} captures the full 3D speed. In the case of high eccentricity, this occurs closer to aphelion, which on the sky will be towards the inner region of its projected orbit. For an orbit aligned with the semi-minor axis (right panel), v_{los} captures the full velocity at perihelion, which is also near the inner region of the orbit. For a cluster with galaxies of high eccentricity but randomly orientated orbital axes, an observer would have many opportunities to observe velocities at their full escape speed, but only for the inner regions of the

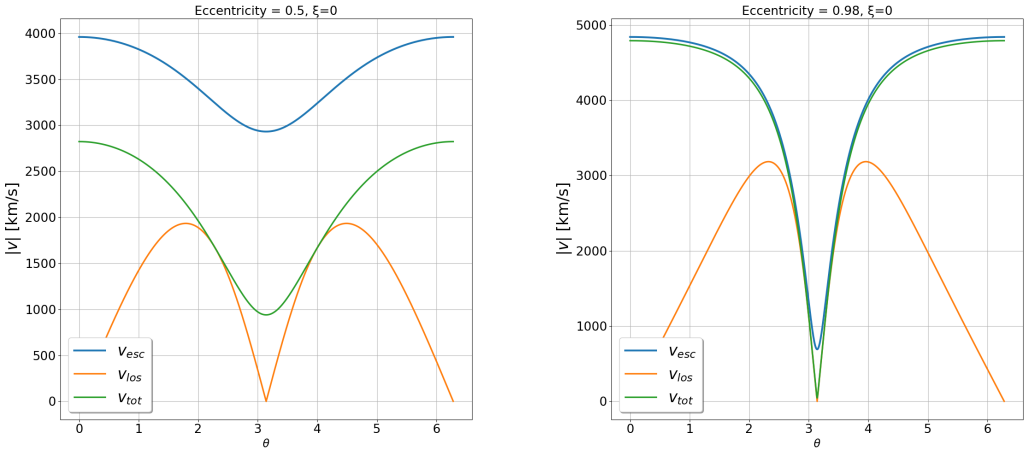

(a)

(b)

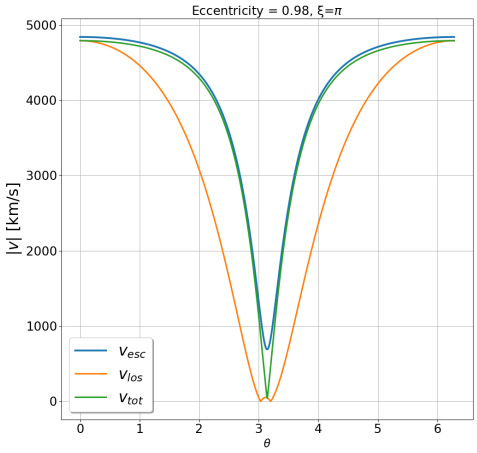

(c)

Figure 3.8: We plot the escape velocity, the galaxy total velocity in 3D, and the observed line-of-sight velocity as a function of the orbit location for two eccentricities and from two viewing angles (ξ). Galaxies with low eccentricity never reach escape speeds whereas for high eccentricity they do. This is consistent with Figure 3.7. When the semi-major axis is aligned along the line-of-sight (top panels), there are many regions in the orbit where the observed v_{los} captures the full 3D speed. In the case of high eccentricity, this occurs closer to aphelion. For an orbit aligned with the semi-minor axis (bottom panel), v_{los} captures the full velocity at perihelion. For a cluster with galaxies of high eccentricity but randomly orientated orbital axes, an observer would have many opportunities to observe velocities at their full escape speed.

cluster.

3.5.4 Quantifying the Escape Velocity Suppression

To quantify the projected escape velocity edge to the 3D edge, we introduce the ratio of the maximum possible observed velocity $v_{los,esc}$ to the escape velocity (v_{esc})

$$Z_v(r_\perp) = \frac{v_{los,esc}(r_\perp)}{v_{esc}(r_\perp)}. \tag{3.45}$$

This ratio quantifies the suppression of the 3D escape edge due to all of the effects discussed in this section and exemplified in Figure 3.8. This is all because of the fact that a distant observer only has one line-of-sight to the galaxy orbits.

We plot Z_v in Figure 3.9. In section 3.4, we argued that even from one position the distant observer is able to observe the actual v_{esc} for any radii with high enough number galaxies per cluster. From this figure we see that this is only the case out to $\sim r_{200}$.

In agreement with the statement in subsection 3.4.3, observing galaxies with $v_{los} \approx v_{esc}$ is a very challenging task (the second Kepler's law ($0.5Pr^2\frac{d\theta}{dt} = \pi ab$) is one of the reasons, e.g. see figure 3.10) and due to a limited number of galaxies the observed ratio Z_v (3.45) is higher than the theoretically predicted value simply due to sampling. The higher number of galaxies per cluster (N) we observe, the higher chance of observing galaxies that satisfy the above conditions which pushes $v_{los,esc}$ closer to v_{esc}. In order to actually figure out the ratio Z_v for each individual cluster, we can create our own mock cluster by populating with galaxies on Keplerian orbits. From this, we can create statistical samples based purely on the analytical formulism described in this section.

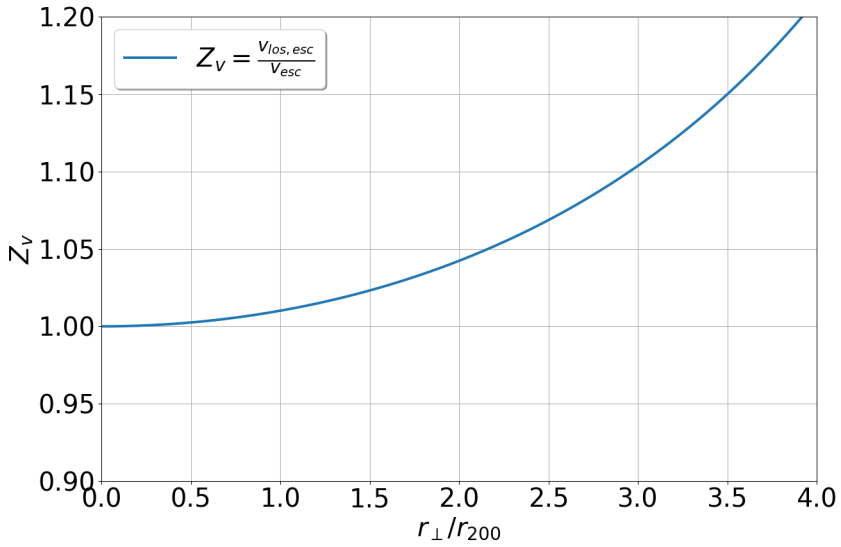

Figure 3.9: The ratio of maximum possibly observed velocity to the escape velocity (3.45). While the effect is significant at high $r_\perp$ it is small in the area of our interest when we work with the real data where we focus only on small distance, i.e. $0.3 \times r_{200} < r_\perp < r_{200}$. The change in the ratio Z_v reaches only 1% at r_{200} which is smaller than the ordinary uncertainty on the weak lensing data ($\sim 20 - 30\%$).

3.6 Statistical Approach

The statistical approach is based on the idea that we can create a cluster which would mimic the basic characteristics of a given galaxy cluster (observed or N-body simulated). To do so, we randomly place galaxies inside of the clusters while forcing them to satisfy several constraints:

1. The galaxies must be on Keplerian orbits.

2. The projected dispersion profile of simulated galaxies must match with high precision the given dispersion profile of the cluster of interest.

3. The normalized density profile must match the weak lensing mass density profile.

4. The number of galaxies inside of the range $0.3 \times r_{200} < r < r_{200}$ should be the

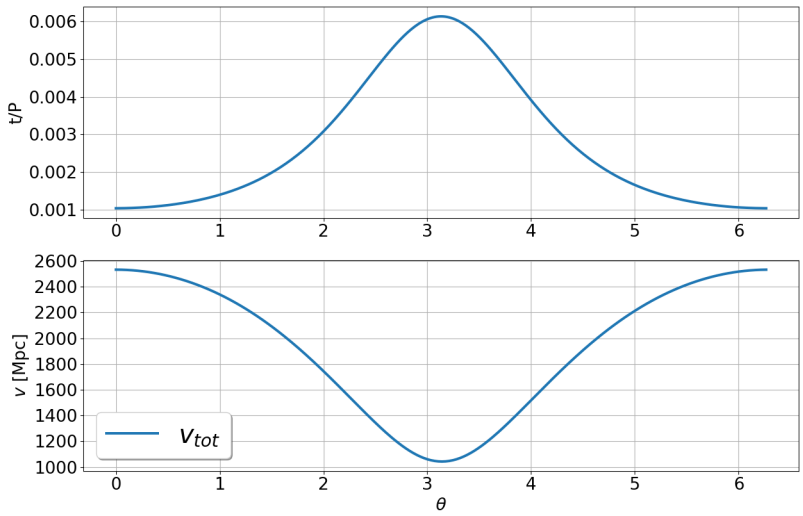

Figure 3.10: The top figure presents the time to cover $\Delta\theta = 1°$ by the galaxy on elliptical orbit relatively to the period of one rotation, i.e. $t(\theta, \Delta\theta = 1°)/P$. The bottom figure shows the actual velocity v_{tot} galaxy has on each of the angular positions θ.

same as of a given cluster.

While on the first glace this approach lacks crucial characteristics, meaning we do not take into account gravitational interactions (galaxy-galaxy, galaxy-DM etc.), we show on simulations that for our purpose we can safely neglect it.

3.6.1 Approach step-by-step realization

The approach consists of several steps. We describe these steps in this subsections.

3.6.1.1 Step #1

Infer from any given cluster several characteristics:

1. Parameters (r_0, ρ_0, n_0) of the Einasto model (3.24) which describe matter density distribution (ρ_w) obtained from weak lensing (green line on the bottom left figure 3.11).

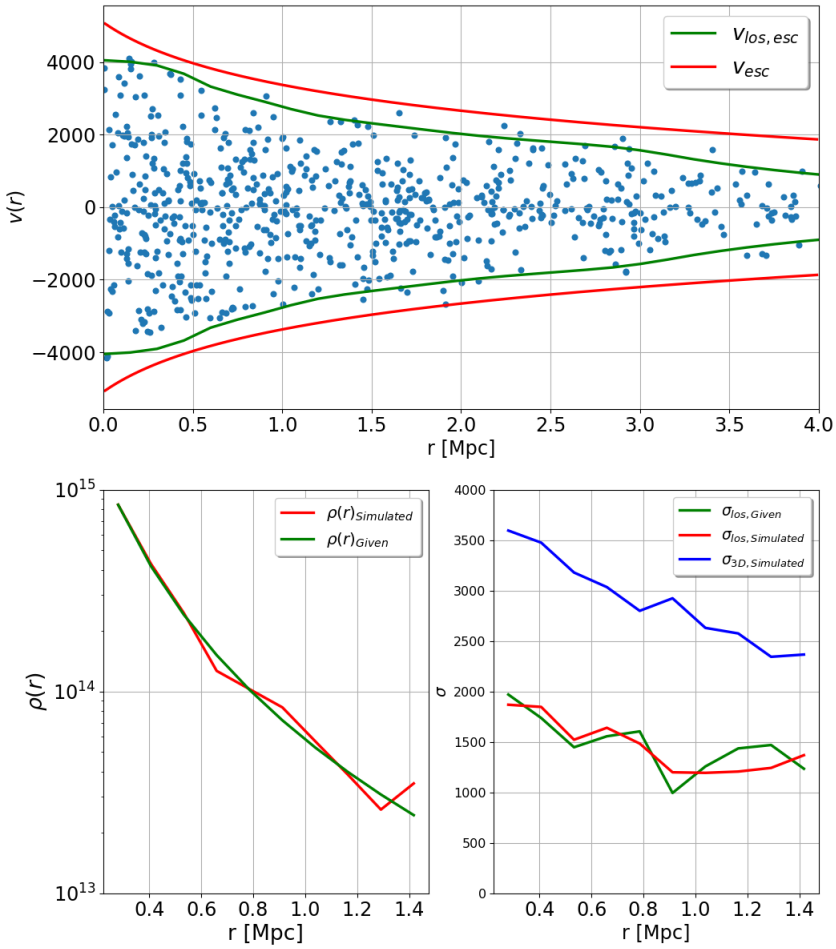

Figure 3.11: To create an analytical mocked cluster phase-space, we first need to be provided an Einasto density profile, a projected velocity dispersion profile and an observed richness measured between a projected $0.3 \leq r/r_{200} \leq 1$. The mock cluster is then generated by selecting galaxies with positions and velocities from a random selection of Keplerian orbits in a cosmological background such that it matches (a) the 3D density distribution; (2) the projected velocity dispersion; (3) the richness. The top figure is an example phase space of a simulated cluster which is populated by 250 galaxies. The 3D escape edge is shown in red and the measured edge (top 1%) is shown in green. Green and red lines on the bottom left (right) figure are the density (dispersion) profiles. In this case, we are mocking a cluster from the Millennium simulation and we also show the 3D velocity dispersion profile in blue.

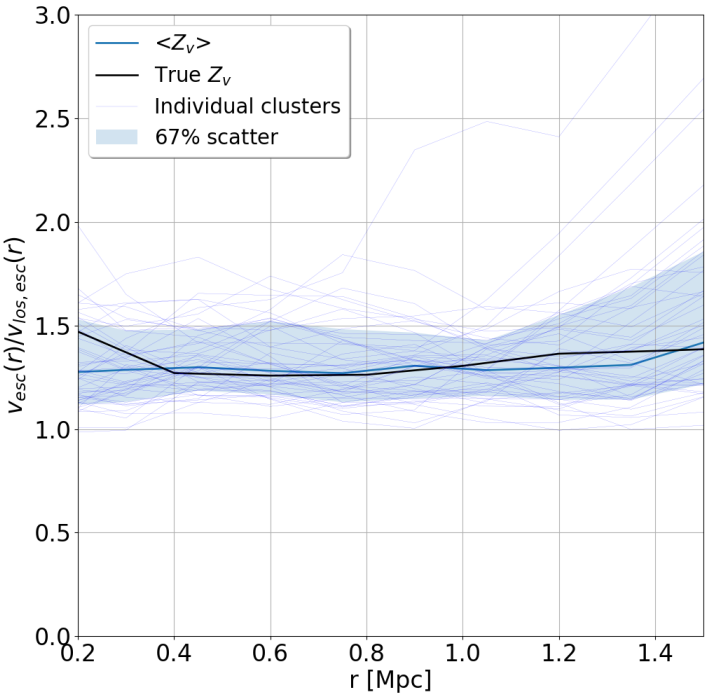

Figure 3.12: We apply the first 5 steps multiple times to find the average prediction for Z_v and its scatter. The thin blue lines are the velocity ratio ($Z_v = v_{esc}/v_{los,esc}$) of 50 individual clusters created by 50 repeats of steps #2-5. Thick blue line and blue shaded region around it are the median and 67% scatter around it of 50 thin blue lines. The thick black line is the actual Z_v of a given cluster, which is available in this case since it is from a simulation. We see that for this one cluster, our analytical prediction of Z_v agrees quite well with the observed suppression in the N-body simulation.

2. Number of galaxies (N) in the projected phase space in the area $0.3 \times r_{200} < r_{\perp} < r_{200}$.

3. Dispersion profile $\sigma(r)$ (3.7) (green line on the bottom right figure 3.11).

4. Maximum velocity profile of the projected phase space ($v_{los,esc}$). As it was mentioned above in the subsection 3.3.2, the interloper removal prescription proposed by *Gifford et al.* (2013) is followed to infer the edge of the phase space.

This provides us all the needed information about a given cluster.

3.6.1.2 Step #2

Apsides r_{min} and r_{max} (see section 3.5) are used to describe elliptical orbits of galaxies. Apsides of individual galaxies are randomly chosen from a given distribution

$$r_{min} = A_1 p_n(A_2, A_3) \tag{3.46}$$

$$r_{max} = B_1 p_n(B_2, B_3), \tag{3.47}$$

where A_2, B_2 are the means and A_3, B_3 are standard deviations of Gaussian distribution $p_n(\mu, \sigma)$.

Parameters A_i, B_i $(i = 1 : 3)$ are drawn randomly from distributions

$$\begin{aligned} A_1 &= p_u(0, r_{200}) \\ A_2 &= p_u(0, r_{200}) \\ A_3 &= p_u(0, r_{eq}) \\ B_1 &= p_u(0, 2 \times r_{200}) \\ B_2 &= p_u(0, 2 \times r_{200}) \\ B_3 &= p_u(0, r_{eq}), \end{aligned}$$

where $p_u(s_1, s_2)$ is a uniform distribution inside range $(s_1 - s_2)$. While above parameters are drawn randomly, the resulting r_{min} and r_{max} has to satisfy basic condition: $r_{eq} > r_{max} > r_{min} > 0$.

Note, each cluster is characterized by A_i, B_i $(i = 1 : 3)$, i.e. A_i, B_i are drawn just once to describe the cluster, so all the galaxies in the cluster have apsides which are drawn from a fix distribution.

3.6.1.3 Step #3

Position of a galaxy on its elliptical orbit is described by angle θ and position of the orbit relatively to the observer is described by angles ξ and η (see figure 3.6). Angles ξ and η are drawn from a uniform distribution $p_u(0, 2\pi)$ while angle θ is drawn from normal distribution $p_n(\pi, 0.5\pi)$ to account for time effect described on figure 3.10. The distance from the observer to the center of the cluster is calculated based on the redshift and cosmological parameters

$$R = \frac{c}{H_0} \int_0^{z_g} \frac{dz'}{E(z')}, \tag{3.48}$$

where $E(z) = \sqrt{\Omega_\Lambda + \Omega_M (1+z)^3}$.

3.6.1.4 Step #4

Procedure from steps #2 and #3 is repeated until number of galaxies in the range $0.3 \times r_{200} < r_\perp < r_{200}$ becomes equal to the number of galaxies of a given cluster. This ends creation of the simulated cluster (see top panel on figure 3.11).

Dispersion profile is calculated using created cluster (red line on the bottom right figure 3.11).

From distribution of galaxies of the created cluster, profile of galaxy density distribution (ρ_g) is calculated (red line on the bottom left figure 3.11). Mass $M_g = 10^{11} M_\odot$ is assigned to each galaxy. Since we want created cluster to have density equal to the density of a given cluster, to compare with weak lensing profile (which is always higher due to a presence of dark matter), normalization needs to be applied. Normalization is done by multiplying galaxy density distribution by $\rho_w(r_s)/\rho_g(r_s)$, where r_s is close to the core and in what follows $r_s = 0.1 \times r_{200}$ (the choice is motivated by the real clusters which have bad quality of the data at small radii).

3.6.1.5 Step #5

Both dispersion and galaxy cluster density is compared with dispersion and weak lensing density of a given cluster. The comparison is done by calculating the difference between logarithms of two profiles

$$\Delta\rho = \sum_i (\log(\rho_w(r_i)) - \log(\rho_g(r_i)))^2$$
$$\Delta\sigma = \sum_i (\log(\sigma_w(r_i)) - \log(\sigma_g(r_i)))^2$$

where $r_i = [0.2, 0.98] \times r_{200}$ with a step $\Delta r = 0.13 \times r_{200}$.

Upper limits $\Delta\rho_{max}$ and $\Delta\sigma_{max}$ are placed on quantities $\Delta\rho$ and $\Delta\sigma$. If any of these two quantities are higher than upper limit, the cluster is disregarded and all the steps #2-5 are repeated (A_i, B_i are redrawn as well) until both of these quantities lower than upper limits $\Delta\rho_{max}$ and $\Delta\sigma_{max}$. The choice of upper limits is discussed below in section 3.7 and it is based on comparison with Millennium simulations (section 3.7). Some of the clusters are disregarded to make sure that only clusters with a similar characteristics (density and dispersion) as of a given cluster are used in the step #6.

3.6.1.6 Step #6

Based on steps #2-5, total $N_{cl} = 50$ clusters are created (thing blue lines on figure 3.12 are the ratio of v_{esc} to $v_{los,esc}$ which are individually red and green lines on the top panel on figure 3.11). The median and 67% scatter around the median are calculated based on individual clusters. Overall, we can see based on this one cluster from Millennium simulations (section 3.7) that approach has predicting power (compare black and thick blue lines on figure 3.12) which we test in section 3.7 based on 100 simulated halos.

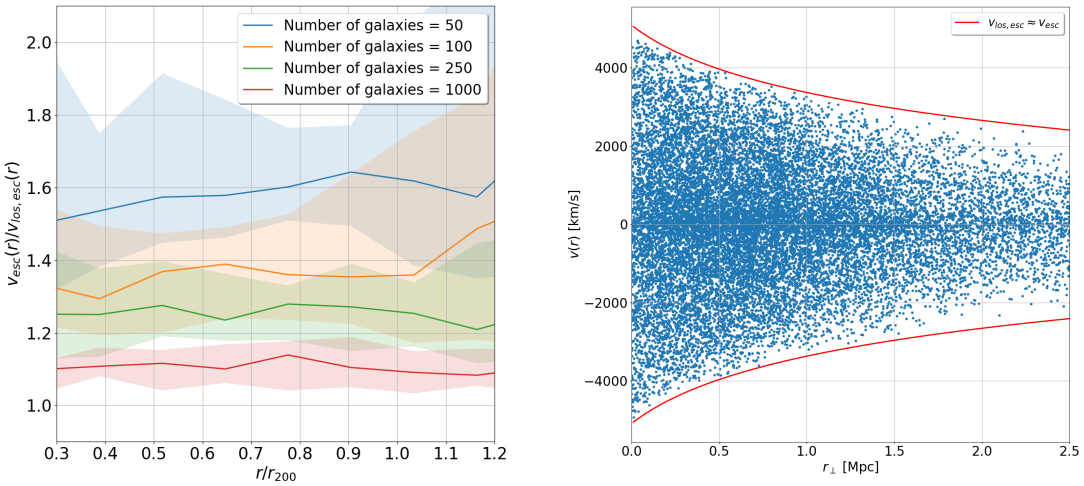

Figure 3.13: The ratio of the escape velocity to the observed phase space edge ($v_{esc}/v_{los,esc}$) by increasing the number of galaxies per cluster in the range $0.3 \times r_{200} - r_{200}$ while mass and dispersion are kept without change. Thick lines and shaded regions with the same colors on the left figure are the medians and 67% scatters around them. The higher the number of galaxies, the lower the ratio Z_v with the case of high number of galaxies (i.e. $N = 1000$) being only $\sim 10\%$ away from 1 and for $N = 10^4$ (right figure) $v_{los,esc} \approx v_{esc}$ as substantial amount of galaxies are on escape velocity profile. One can notice an agreement with theoretical derivation depicted on figure 3.9 as for higher radii maximum observed velocity is a few percent lower than $v_{los,esc}$, while for small radii up to $\sim 1 - 1.5$ Mpc there are galaxies on red line.

3.6.2 Discussion of the approach

The key parts, which are needed to populate the projected phase space, are the expressions of the projected distance $r_\perp$ (3.27) and v_{los} (3.37) which are functions of many parameters which can be combined into four groups:

1. Cosmological parameters: Hubble constant (H_0), matter density (Ω_m) and dark energy density ($\Omega_\Lambda = 1 - \Omega_m$).

2. Parameters that describe the galaxy cluster: redshift (z), total number of galaxies per cluster (N), dispersion profile, matter density distribution (in terms of

Einasto parameters: r_0, ρ_0, n) as well as R_{200} and M_{200} which can be derived from matted density distribution and cosmological parameters.

3. Description of the position and velocity of the galaxy inside of the cluster: angle θ, distance from the center of the cluster to the galaxy (r). Note, that while the total velocity relatively to the center of the cluster (v) is important in simulations, we do not need to know it as the Keplerian orbit defines the total velocity, i.e. all the parameters from these three groups define the total velocity.

4. The parameters describe position of the observer: two spherical angles (η and ξ) and the distance from the observer to the center of the cluster (R) which is a redundant parameter of the parameters mentioned above as it is a function of the redshift and cosmology.

Based on the approach we can not only predict $v_{los,esc}$ for a given number of galaxies, but also predict how $v_{los,esc}$ will change if we get more observational data from future surveys. Moreover, we can see that by increasing number of galaxies per cluster the ratio Z_v (3.45) decreases and moves closer to 1 which is equal to $v_{los,esc}$ increasing and moving closer to v_{esc} (see figure 3.13).

3.7 Results

From here on we describe the algorithm defined in the previous section as our "analytical model". This is because it is based purely on an analytic description of elliptical orbits in an extended mass profile and in a cosmological background. The choice of orbital parameter and orientations is infinite, but they all obey Keplerian dynamics. In order to create a mock cluster phase space, which is based on many galaxies each at some locations in their respective orbits, we are required to use Monte Carlo techniques to sample from the analytical formulae. Also as noted in the previous

section, we are also required to first define the parameters which describe the system itself, including the mass profile, the dispersion profile, and the number of phase space galaxies. There is no unique projected phase space for any cluster. However, each Monte Carlo realized phase space has the correct 3D escape profile (based on the mass profile), the correct dispersion profile, and the correct phase space richness.

Once we have realized a projected phase space profile, we measure the maximum velocity edge. We can create multiple realizations of a single cluster to place statistical constraints on the measurement of the edge itself. Likewise, we are able to create samples of different clusters with different mass profiles, change the cosmology, or change the phase space sampling. In this section, we use a sample of simulated halos and galaxy catalogs to quantify the precision and accuracy of the analytical formalism.

The simulated data we use was based on the Millennium simulations (*Springel et al.*, 2005). Particles from these simulations are used to calculate Einasto mass density profiles (equation 3.24) which we treat as observed weak lensing data. Overall, 100 halos are selected to test our approach. The masses are widely spread ($9.3\times10^{13}-1.03\times10^{15}M_{\odot}$) with the average mass $< M >= 2.34\times10^{14}M_{\odot}$ and $< R_{200} >= 0.95$ Mpc. To infer galaxies and the phase spaces in general, the semi-analytical galaxy catalog from *Guo et al.* (2011) is used.

To cover a typical range of the number of galaxies per cluster (N) as of realistic data, we create subsets of projected galaxy positions and velocities for these halos using varying apparent magnitude limits. Since our goal is to compare how well our approach predicts the observed edge in simulations, we project every simulated halo and its semi-analytic galaxies to a distance of 30 Mpc and create projections for 100 random viewing angle orientations. We measure the average phase space edges and calculate the average projected dispersion profiles and the average number of galaxies in the projected region $0.3\times r_{200} < r < r_{200}$ and its scatter. Based on the number

of semi-analytic galaxies, the dispersion and the density profiles, our approach allows us to predict the projected edge and compare to simulations.

The galaxy dataset with the bright magnitude limit provides clusters with projected phase space richnesses from $19 < N_l < 257$ with the average number $< N_l >= 58$. While the deeper dataset contains around twice as many galaxies per cluster as the set N_l: $40 < N_h < 525$ with the average $< N_h >= 118$. Note, these sets are different descriptions of the same halos with the only difference being a higher number of dimmer and less massive galaxies per cluster.

3.7.1 Velocity ratio of Millennium simulations as a function of number of galaxies per cluster (N)

In subsection 3.6.2 we showed that when using a cluster with a mass profile, dispersion profile, and phase space richness defined by a single halo in the Millennium simulation, we were able to recover the true suppression ratio using our analytical model (see figure 3.12). In that specific case, we used a single richness as defined by the "observed" (i.e., line-of-sight projected) data after applying a specific magnitude limit to a projected halo. We also used the observed projected velocity dispersion profile and the underlying 3D mass profile to create the analytical mock Keplerian system.

However, our premise is that the suppression value (Z_v) should depend on the phase space richness: we predict an increase in $v_{los,esc}$ (or a decrease in the projected suppression) as the number of galaxies per cluster increases. Our sample of Millennium clusters is big enough to split it into 6 groups based on number of projected phase space galaxies N: $0-25$, $25-50$, $50-75$, $75-100$, $100-150$, $150-200$ and 200+. The first four groups are taken from the bright magnitude dataset (N_l), while the last two groups from the sample with a deeper magnitude limit (N_h). We treat these datasets as being realistic observational data, such that the phase spaces are in

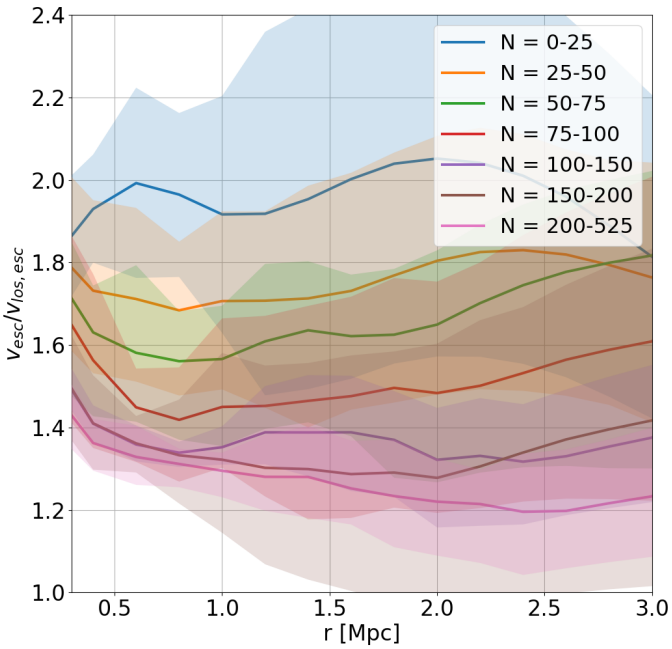

Figure 3.14: $Z_v(r)$ (3.45) as a function of number of galaxies per cluster (N) for the bright magnitude limit dataset (bins with $N_l = 0 - 150$) and the deeper dataset (bins with $N_h = 150 - 525$). Thick lines and shaded regions with the same colors are the medians and 67% scatters around them. Overall, we can easily detect clear consistency in this results with our theoretical and the approach predictions, as the increase in the number of galaxies per cluster in the range $0.3 \times r_{200} - r_{200}$ from $N = 0 - 25$ all the way to $N = 200 - 525$ pushes the ratio Z_v lower which is equal to pushing maximum observed velocity $v_{los,esc}$ higher and closer to the escape velocity v_{esc}. Moreover, the magnitudes of the ratios presented on this figure practically match results presented on the left figure 3.13.

principle observable to these magnitude limits with typical astronomical instrumentation. Recall that we are sampling the projected positions and velocities from the *Guo et al.* (2011) semi-analytic galaxy catalogs projected to a distance of 30Mpc.

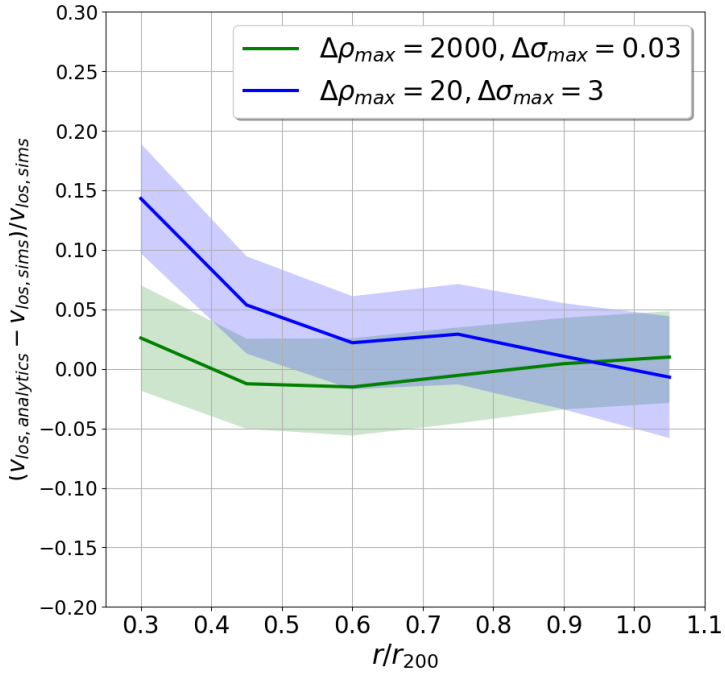

Figure 3.15: Comparison cluster-by-cluster Millennium simulations ($v_{los,sims}$) with the approach predictions ($v_{los,analytics}$) of $v_{los,esc}$ for the 10 heaviest systems with the masses typical observed clusters have (i.e. $M_{200} = 3.7 \times 10^{14} - 1.1 \times 10^{15} M_{\odot}$). Thick lines and shaded regions with corresponding colors are the weighted means and weighted errors around these means. Blue (green) color correspond to the case with tight (weak) density constraint and weak (tight) dispersion constraint. We can see great predicting power of $v_{los,esc}$ by the approach for the case with tight dispersion and weak density constraint in the range of our interest (i.e. $0.3r_{200} - r_{200}$), while blue line is significantly off.

3.7.2 Cluster-by-cluster comparison Millennium simulations with the approach

We saw that our approach is capable of predicting $v_{los,esc}$ profile for one cluster (see figure 3.12). However, the main question is how well our approach predicts maximum velocity profile for all the simulated halos available. Appears that the approach predictions are statistically in a great agreement with measured $v_{los,esc}$ profiles.

As it was discussed in section 3.6 step #5, we place upper limits on density

($\Delta\rho_{max}$) and dispersion ($\Delta\sigma_{max}$). It appears that results are not sensible to the density constraints while highly sensible to dispersion constraints (compare green and blue lines and shaded regions on figure 3.15). This allows us to conclude that tight upper dispersion (density) limit is (not) required to produce precise prediction of $v_{los,esc}$. It should be noted that despite placing tight density constraints, density is fitted practically identically well (i.e. similar values of $\Delta\rho$) for the case with very high upper bound on density. This is due to the tight dispersion constraint and the fact that velocities of individual galaxies are functions of gravitational potential, which indirectly forces galaxies to satisfy density constraints. We conclude that when creating a mock cluster phase space, it is more important to constrain against the dispersion profile than the density profile. This is an obvious consequence of the tight underlying connection between the velocity dispersion and the cluster mass (e.g., *Evrard et al.* (2008)).

First, we can look at the halos with the masses of real clusters (*Halenka and Miller*, 2018), i.e. $M_{200} = 3.8 \times 10^{14} - 1.1 \times 10^{15} M_{\odot}$ and there are 10 halos in total with the masses falling into this range. Both N_l and N_h sets produce great agreement with the actual simulations (e.g. see green line on 3.15) and the approach predicts escape velocity profile with $\sim 2\%$ accuracy in the range $0.35r_{200} - 1.05r_{200}$ with weighted errors not leaving tight 5% range.

Due to the way our approach is created (i.e. we create a cluster with the random distributions and only then compare dispersion with a given dispersion), it is computationally demanding and it is hard to place any sensible upper limit $\Delta\sigma_{max}$ which is different cluster-by-cluster since different clusters need different upper limit on dispersion to produce $v_{los,esc}$ close to the actual measured maximum observed velocity (this happens mostly due to a bumpy shape of dispersion profile, e.g. green and red lines on dispersion panel on figure 3.11). To solve both of these problems, we simply run our approach 10 times and choose the one with the dispersion closest to

a given dispersion, i.e. lowest $\Delta\sigma$, while not choosing clusters based on $\Delta\rho$. Based on our analysis, it appears that 10 runs is enough as we draw galaxies with velocities *a priopi* being functions of density. Moreover, using median and scatter allows us to effectively drop those clusters which have bad $v_{los,esc}$.

The real systems used for analysis have at least 50 galaxies per cluster. We apply 10 runs approach to both simulated halo sets. N_l set has 45 of such systems, while N_h has 96 (all but 4 halos have more than 50 galaxies). As we can see on the figure 3.16, the approach predicts correctly maximum observed velocity profile with $\sim 2\%$ accuracy in the range $0.4r_{200} - r_{200}$.

The success in predicting $v_{los,esc}$ allows us to argue that the approach is capable of correctly predicting maximum velocity edge by mimicking dispersion, density and N of a given cluster.

3.7.3 Independence from anisotropy

Diaferio (1999) introduced the approach of connecting v_{esc} and $v_{los,esc}$ using the anisotropy parameter $\beta(r)$. As noted in section 3.3.2, this cannot be valid for multiple reasons, including the fact that the 3D edge is in principle observable given enough data and regardless of the average cluster anisotropy. We can test this with our analytical model, since we can create mock cluster phase spaces that are otherwise identical, except that they have different levels of (average) velocity anisotropy.

We do this by selecting galaxies from the orbits in Step 3, such that the radial and tangential velocities produce the desired anisotropy. Of course when we do this, we ensure that all nominal requirements are still met (e.g., on the density profile, the dispersion profile, and the richness). With enough orbits, we are able to define different mock clusters with different anisotropies. We can selectively keep galaxies that are on elliptical orbits and at positions well beyond r_a such that their velocities are mostly radial. Similarly, we could choose to keep galaxies that are on more circular

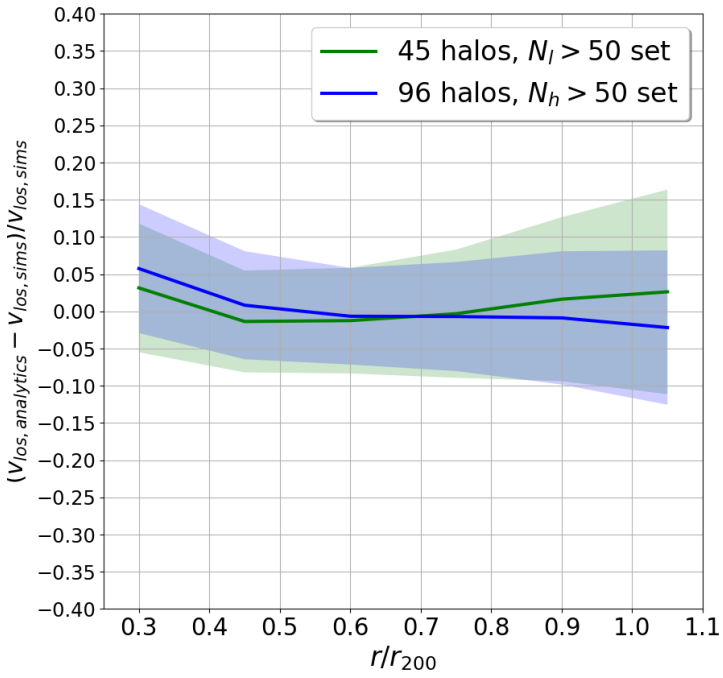

Figure 3.16: Comparison cluster-by-cluster of $v_{los,esc}$ for Millennium simulations with the approach predictions for the halos with > 50 galaxies per cluster in the $0.3 \times r_{200} - r_{200}$ range. Thick blue (green) line and shaded region around it correspond to the mean and 1σ standard deviation around the mean for the N_h (N_l) set with at least 50 galaxies. For each halo from simulations ($_{sims}$ on the label) the median prediction of $v_{los,esc}$ was calculated for 50 clusters created by the approach ($_{analytics}$ on the label), with each of these 50 clusters being chosen from 10 randomly created, so it has the closest dispersion to the simulated halo out of these 10 clusters.

orbits or near r_a, such that their tangential motion dominates. In practice, we simply draw different distributions from the angle θ which defines a galaxy's location in its orbit (and thus its ratio of the radial versus tangential velocity).

To make this test, we create 50 clusters and split them into two bins: 25 clusters with the highest β and 25 with the lowest (see green and blue lines on the bottom figures 3.17). We then measure the suppression ration Z_v. We created 4 bins in anisotropy with average values $\beta \sim$ -2.5, -1, 0, +0.5, which spans the range of possible values that is currently seen in data and simulations *Stark et al.* (2019). For each of

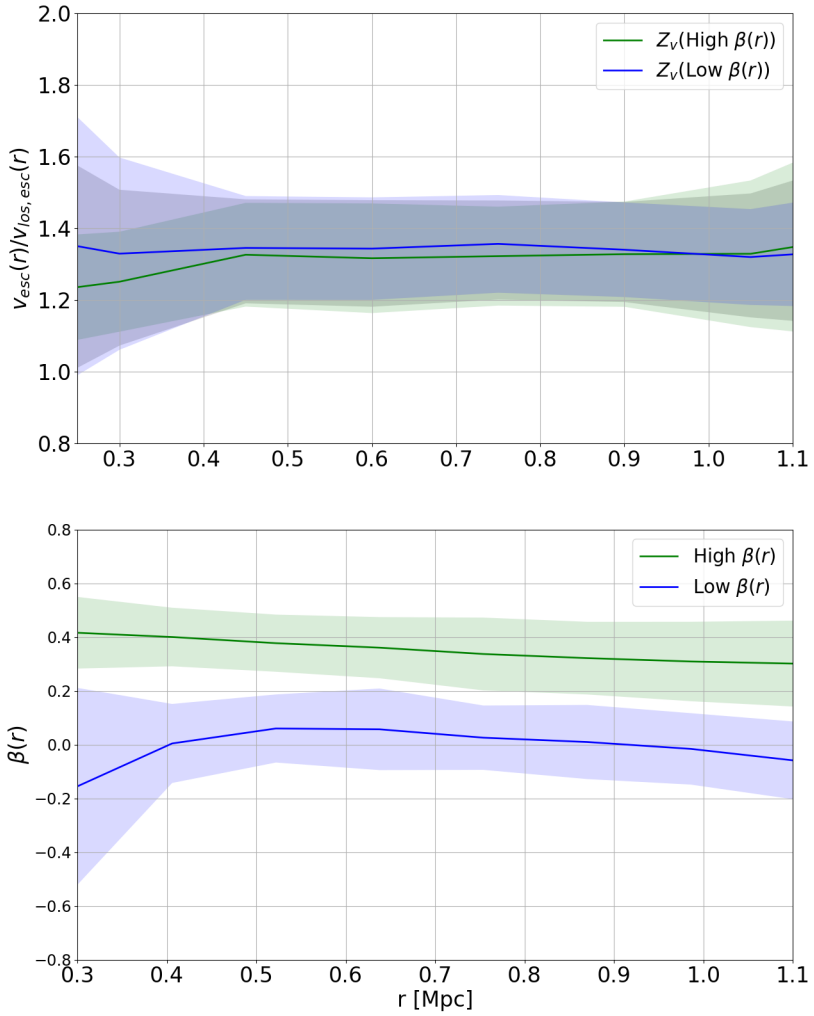

Figure 3.17: The top panel shows the velocity ratio Z_v for a typical cluster modeled on a specific cluster from the Millennium sample. The bottom panel shows the anisotropy profile for 25 realizations of this mock cluster after choosing galaxies such that their orbits are either mostly radial ($\beta = 0.5$) or mostly isotropic $\beta = 0$. As we see in the top panel, the suppression ratio is independent of anisotropy. This independence between Z_v and β holds down to at least $\beta = -2.5$, where galaxies are mostly on a tangential component of their orbit.

these 4 average values of β the suppression is the same (e.g. see figure 3.17 for $\beta \approx 0$ and ≈ 0.5), which allows us to conclude that the suppression ratio is independent of anisotropy in the range $-2.5 \leq \beta \leq 0.5$.

3.7.4 Mass and cosmology independence

The goal of this subsection is to show that for the clusters with different masses and for different cosmologies, but the same N the ratio Z_v is the same. This way we can create a map or grid of ratios as a function of N which would allow us to test cosmology, since we know measured $v_{los,esc}$ from the data and v_{esc} changes with cosmology.

3.7.4.1 Indirect dependence of $v_{los,esc}$ from cosmology

First, we see that for a fixed dispersion, but for different cosmologies we get the same $v_{los,esc}$, i.e. the approach populates clusters with galaxies individual velocities of which are calculated for different cosmological parameters. Results on figure 3.18 show that for a very wide range of cosmologies, $v_{los,esc}$ is practically unchanged. Note, in reality dispersion does change with the change in cosmological background, but we fix it unchanged (i.e. as if we have same dispersion in different environments), which leads to the conclusion of independence of $v_{los,esc}$ from cosmological background directly, while it is highly dependent of dispersion profile. This makes $v_{los,esc}$ depend on cosmology indirectly as evolution of the cluster and subsequently dispersion would change for different cosmologies.

3.7.4.2 Z_v independence from cosmology and mass

Overall, we can not test and prove independence using the approach or simulations alone: the approach needs dispersion (i.e. we need to know mapped dispersion with mass and cosmology), but we do not know how dispersion and mass are con-

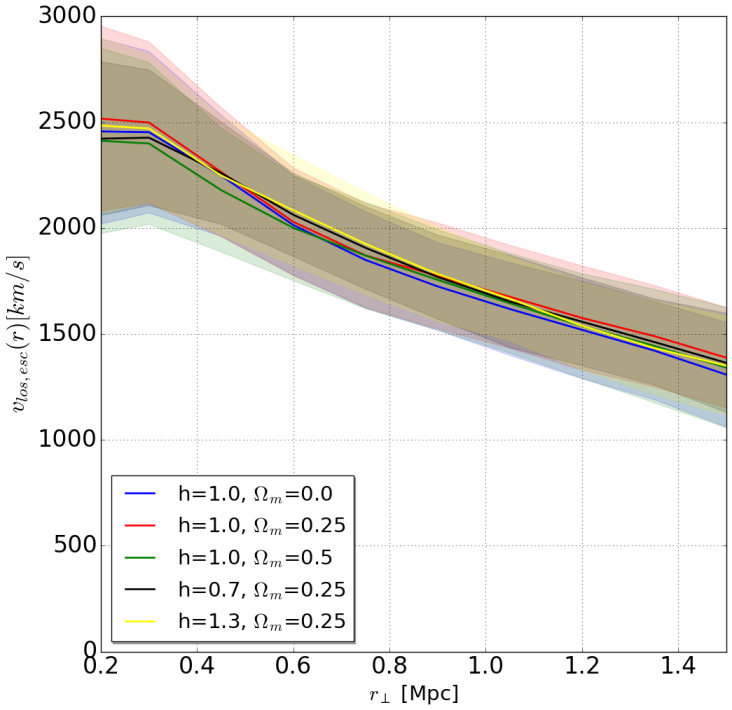

Figure 3.18: $v_{los,esc}$ for a fixed velocity dispersion (σ), but in different cosmological backgrounds (different h_0 and Ω_m parameters), the approach was applied to create cluster with mimicking dispersion of a given system. $h = 1, \Omega_m = 0.25$ is the true cosmology. There is practically no change in the maximum observed velocity profile for a fixed σ.

nected. Millennium simulations have direct correlation between number of galaxies and masses, i.e. the higher N consequently the higher m_{200}, so we can not split data into several mass bins with the same number of galaxies to test our hypothesis. Fortunately, there is a way to combine the approach with simulations. We need to follow several steps:

1. We know from simulations correct dispersion, cosmology, number of galaxies and matter distribution profile.

2. Using the approach we fit it in a traditional manner (i.e. apply the approach) which allows us to create multiple copies of a given cluster.

3. We know how the velocities and positions change with the change in matter distribution and cosmology (see 3.22 and 3.27). We change individual galaxy velocities and positions according to these expressions (e.g. see figure 3.19, where for different matter distributions positions of the galaxies on the phase-space change).

4. New "modified" clusters is used to measure new variance and $v_{los,esc}^{new}$ (see thick lines on figure 3.19).

5. Compare $Z_v^{new} = v_{esc}^{new}/v_{los,esc}^{new}$ (where ^{new} means new mass or cosmology) with the old original Z_v. If the original idea about independence of the ratio from cosmology and mass is correct, we will get $Z_v^{new} = Z_v$.

While by fitting the same dispersion for different cosmological backgrounds or equivalently matter distributions produces the same $v_{los,esc}$ (see previous subsection), change in cosmology should change dispersion itself. We can see it on figure 3.19, where for different matter distributions individual positions and velocities do change, which in turn changes maximum observed velocity profile as well as dispersion itself.

Calculating Z_v^{new} for a wide range of cosmological parameters and masses, we see that the velocity ratio Z_v does not change much at all (see figure 3.20), while on the first glance a significant change in the mass of the cluster is observed (see figure 3.19). This effect is due to a synchronization of changes in both escape velocity profile and $v_{los,esc}$ and these changes practically ($\sim 3-4$ times smaller than the 67% scatter) cancel each other out which leads to the proof of independence of the velocity ratio from cosmological parameters and mass of the cluster as we change all 3 parameters in the very wide region, i.e. $\Omega_m = 0-0.5, h_0 = 0.7-1.3$ and mass was increased and decreased by 20%.

This analysis reinforces the important concept which is the premise of this chapter: *the suppression of the 3D to 2D escape edge is due to statistical sampling alone.*

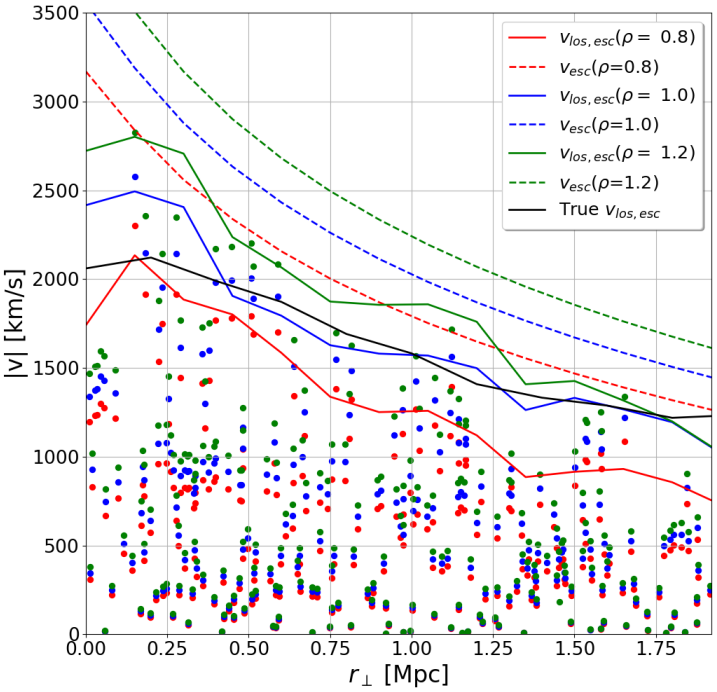

Figure 3.19: One cluster with a given from simulations dispersion, density and number of galaxies. Using approach a mock cluster is created. Since we know all the characteristics of individual galaxies, we can calculate how they will change due to the change of gravitational potential, which is a function of mass of the cluster, Hubble constant and Ω_m. While results are presented only for change in ρ (amplitude of matter density), similar changes on phase-space diagram occur when Ω_m and h_0 change.

Having searched for Z_v dependencies on velocity anisotropy, cluster mass, and cosmology and found none, the remaining choice is to identify the dependence on the number of phase-space galaxies.

3.7.5 Velocity ratio as a function of number of galaxies

Since it was shown above, that Z_v is independent of the cosmology and mass of the cluster and the approach predicts correctly observed velocity profile, we can find velocity ratio simply by running approach for a specific cluster with different number of galaxies. This does not change v_{esc} (no mass, cosmology changes), but substantially

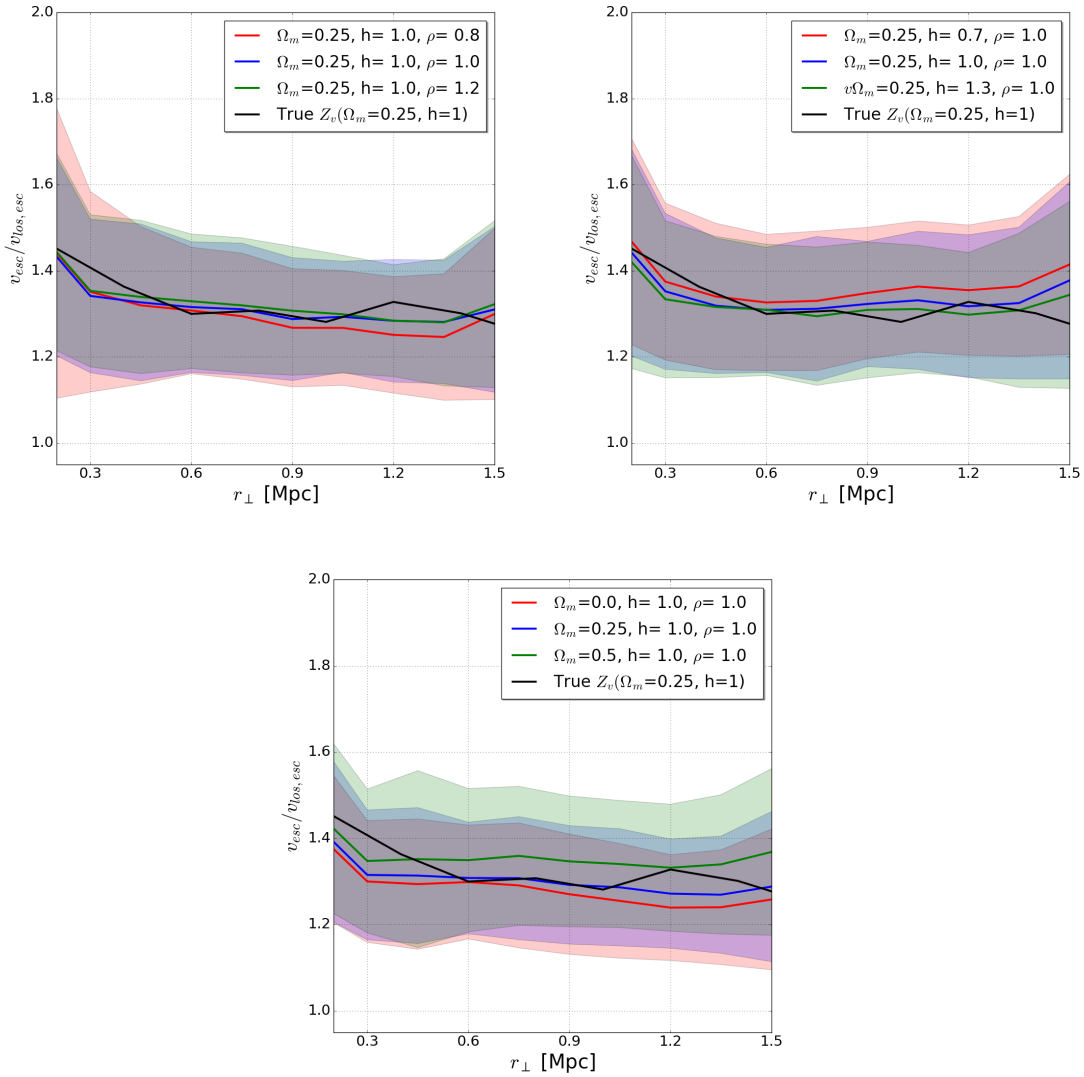

Figure 3.20: One cluster with a given from simulations dispersion, density and number of galaxies. Using approach 100 mock clusters are created. Since we know all the characteristics of individual galaxies, we can calculate how they will change due to gravitational potential change by changing mass of the cluster (top left), Hubble constant (top right) and Ω_m (bottom). Label ρ means the proportion of the total mass of the given system. The change in cosmological parameters or mass changes the ratio $Z_v \sim 3-4$ times less that the uncertainty of the approach, which allows us to safely count Z_v as being constant.

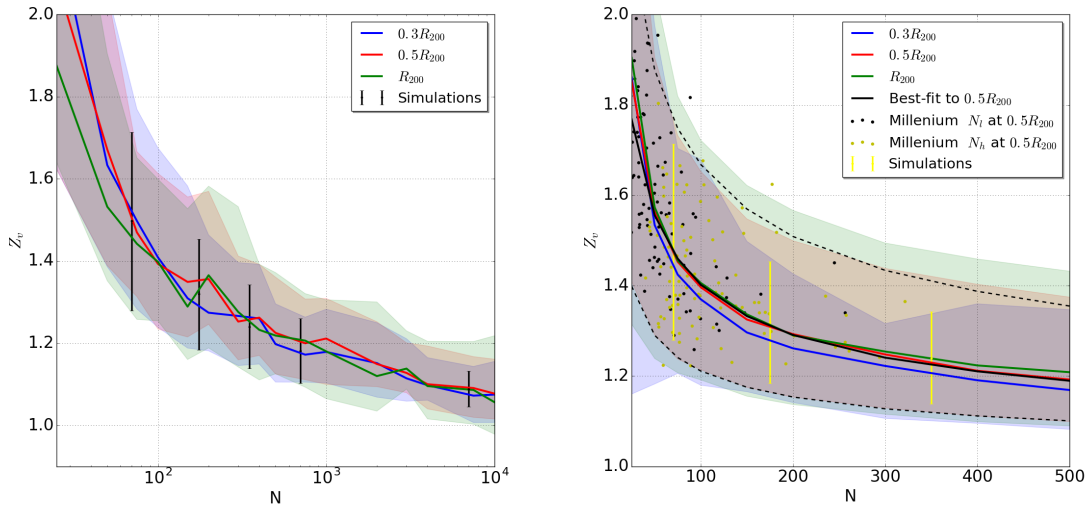

Figure 3.21: Velocity ratio Z_v as a function of number of galaxies. To find velocity ratio which is independent of cosmology and mass of a cluster (see subsection 3.7.4), we use a cluster and change number of galaxies (N) while measuring both v_{esc} and $v_{los,esc}$ to calculate velocity ratio. Left: thick lines and shaded regions correspond to medians and 67% scatters around the medians by measuring at 3 radial positions: $0.3R_{200}$ (blue), $0.5R_{200}$ (red) and R_{200} (green). Note, suppression function is clearly moving towards unity in logarithmic scale. Right: statistical analysis of $N_h = 100$ clusters at $0.3R_{200}$ (blue), $0.5R_{200}$ (red), R_{200} (green) and best-fit (black solid and dashed lines) fitted to the red line and shaded region based on functional form 3.49. Solid lines and shaded region with the same color correspond to the weighted means and weighted errors around the weighted means of 100 individual lines (e.g. see left figure). Black (yellow) dots are individual velocity ratios measured at $0.5R_{200}$ of systems from Millennium simulations set N_l (N_h). Note, while results are presented for N_h set, identical results (change $< 2\%$) are produced by $N_l > 50$ set. Black (yellow) error bars on the left (right) figure are the means and 1σ standard deviations of the scatter based on Millennium clusters and 30 lines of sight to each cluster (particle instead of galaxies were utilized to achieve high richness N).

changes $v_{los,esc}$ (due to change in N).

We measure median and 67% scatter at 3 points along radial axis: $0.3R_{200}, 0.5R_{200}$ and R_{200}. We can see clearly that suppression goes to 1 at high N and by $N = 10^4$ it is 7% away from being $Z_v = 1$ (see left figure 3.21). While the ratio looks the same at difference radii for one specific case (see left figure 3.21), it is actually the same only for $0.5R_{200}$ and R_{200}, while being slightly lower (by $\sim 2\%$) for $0.3R_{200}$ case, which is in agreement with prior results (e.g. see figure 3.13) as we saw that at $0.3R_{200}$ our approach overestimates $v_{los,esc}$. This result also implies that the ratio is constant for different radii. This allows us to focus our statistical analysis of velocity ratio at one radial point and without loss of generality we use $r = 0.5R_{200}$.

Overall, we can see clear inverse power-law functional form of the velocity ratio. This allows us to propose the following power-law model

$$Z_v(N) = 1 + \left(\frac{N_0}{N}\right)^{\lambda}, \tag{3.49}$$

where N_0 and λ are the parameters of the model.

The best-fit model of statistically analyzed velocity ratio of 100 halos from N_h sample (red line on right figure 3.21) is presented as solid and dashed black lines on the right figure 3.21 with the best-fit parameters: $N_0 = 14.205, \lambda = 0.467$ (the bottom error bar line: $N_0 = 3.213, \lambda = 0.392$, the top error bar line: $N_0 = 35.822, \lambda = 0.454$). This result correlates well with individual ratios from Millennium simulations (see black and yellow dots on the right figure 3.21). Moreover, much greater agreement of the approach is with the Millennium simulation when 30 different lines of sight were used to quantify suppression (see black (yellow) error bars on the left (right) figure 3.21). Note, that in this case particles instead of galaxies were used to achieve high richness. This high level of agreement supports the choice of the functional form of the suppression (3.49) and the corresponding best-fit values of the parameters of the

model.

3.8 Discussion and Conclusions

In this work we showed that in projected phase space the full 3D escape velocity can be measured with 1% accuracy at small radii (see subsection 3.5.3.1). Unfortunately, to do that we need a lot of galaxies and in reality we do not have high enough number of galaxies to actually fill out the phase space to have enough galaxies to contribute to the edge. To find how much we underestimate escape velocity profile on a cluster-by-cluster basis, we created a novel approach of predicting it, which is based on the idea of creating a mock cluster with a galaxies on Keplerian orbits so that they satisfy several constraints such as the mock cluster should have the same number of galaxies, identical dispersion and matter density profiles as a given cluster.

The general idea is to develop a way of predicting based on the phase space and the density distribution the actual observed edge on the phase space diagrams. While we create the simplified version of simulations which does not take into account any interactions between particles (or galaxies and dark matter), it allows us to quickly estimate the actual observed edge. This is in contrast to conventional simulations which would require heavy computations to run one round of simulations as well as traditional simulations do not allow us to control specific characteristics of the clusters, which is extremely important for us to be able to correctly estimate the actual observed edge of the real galaxy clusters (we simply use as a granted mass distribution from weak lensing and galaxy distribution on the phase space diagram). Being able to change by our choice all the mentioned above characteristics of galaxy clusters is an extremely powerful tool. One of the main applications is that we can utilize phase spaces to test variety of gravitational models and place constraints on cosmological parameters. Previously, people did use galaxy clusters for these applications. However, they utilize only one data point per clusters as their focus was

explicitly on equilibrium radius r_{eq} (point at which gravitational push by matter of a cluster is equal to the gravitational pull by dark energy). In contrast, our approach allows to utilize the whole phase-space, which gives us $6-10$ (depending on the binning approach utilized) data points per cluster. Moreover, these data points are in the most sensitive regions where the gravity is the strongest and precision of the data is the highest. It has a big potential in allowing us to place high precision constraints on the parameters and models of interest while utilizing the full constraining power of the phase-spaces of the galaxy clusters.

There were no attempts in the literature to connect the ratio of escape velocity profile to the observed edge ($Z_v = v_{esc}/v_{los,esc}$) with the number of galaxies per clusters. Moreover, it was previously thought that anisotropy plays crucial role in predicting this ratio (*Diaferio*, 1999). However, we argue based on our approach and our results that the number of galaxies plays very important role while the anisotropy does not and we showed that there is a direct correlation between number of galaxies N and the velocity ratio Z_v. We also argue that in principle, under specific circumstances, we can observe the actual v_{esc} (i.e. $Z_v \approx 1$) even in projected view. Moreover, we showed that the velocity ratio is mass and cosmology independent which makes Z_v to be a function of N only and it exhibits inverse power-law behaviour which can be described by the model 3.49 and be fitted with power ~ 0.5 effectively meaning that $Z_v \sim N^{-0.5}$.

We tested our approach against N-body Millennium simulations and predictions of the escape velocity profile broadly agree with the simulations with $\sim 2\%$ accuracy in the wide radial range $0.4R_{200} - R_{200}$ where we focus our analysis when work with the real clusters. One of the interesting conclusions of our work is the ability to predict the escape velocity profile based on mock clusters with galaxies which do not interact directly (the only interaction is a global gravitational field created by all the massive objects in the clusters and described by spherically symmetrical models such

as Einasto and NFW) as we populate our clusters with random galaxies on Keplerian orbits. This could potentially lead to the conclusion that most of the clusters are relaxed and 3-body interactions are rare. However, more work on this topic needs to be done.

CHAPTER IV

Conclusions

4.1 Dissertation overview

Huge amount of effort is done towards explaining the origin and the theory of DE and DM, but we are still far away from solving one of the greatest mysteries in present science. Our hope is that this work provides an important piece towards understanding of our Universe. Overall, the goal of the current work is to utilize the galaxy clusters to test gravity and cosmology. We use the galaxy clusters in two different ways: by utilizing matter density profiles and by using escape velocity profiles. The first method is used in the chapter II to test Emergent Gravity model proposed by *Verlinde* (2017), while the development of the second method is the goal of the chapter III, where we derived the suppression of the escape velocity profile due to the observation of the galaxy clusters in 2-dimensions. This allows us to have direct measure of gravitational potential through observation of the escape velocity profiles. Moreover, the first attempt to utilize this derived suppression to probe cosmological parameters is done in the section 4.5, where preliminary constraints on the cosmological parameters were placed by statistically analyzing 38 galaxy clusters using the Bayesian approach. Below, we summarize scientific results of each of these chapters.

4.2 The Emergent Gravity Test

While this works does not provide the first test of Emergent Gravity, it tests EG in the more statistically accurate way in comparison with the first attempts by *Nieuwenhuizen* (2017) and *Ettori et al.* (2019). We utilized the data set of 23 galaxy clusters for each of which high precision weak lensing and X-ray data were collected from the literature. The data cover a wide radial ($0.1R_{200} - 2R_{200}$) and redshift ($0.077 - 0.289$) ranges. The statistical analysis of the collected data sample allows us to rule out EG at $> 5\sigma$. This high level of constraint is due to the significant difference between the observed DM profile (inferred from the weak lensing and X-ray data) and the apparent DM profile (predicted by the EG model from the underlying baryon matter distribution).

It should be noted that EG provides good results in the area near the virial radius, where the observed DM and the predicted apparent dark matter are almost identical. Overall, EG model predicts a flatter than the observed data shape of the dark matter mass distribution, as well as steep X-ray gas density profiles and under the nominal assumptions (i.e., without systematics), EG favors a radially decreasing baryon fraction which peaks in the cluster core. This is a different baryon fraction profile when compared to the standard dark matter model (see *Ade et al.* (2016)).

Moreover, we investigate the level of systematic errors needed to reach good agreement between EG and the observational data. Our conclusion is that within the current systematic limits, there are combinations of shape profiles which can match EG to the data. Additionally, we investigated whether the EG model itself has the flexibility to better match the data and we find that it does through a lowering of the maximal strain. Overall, given our current level of the systematic uncertainties in the observed shape profiles of the weak lensing and baryon matter density as well as the current stage of the development of the theoretical framework of EG model, our results lead to the conclusion that we can not formally rule out EG model and it is a

viable alternative to dark matter in the galaxy clusters in the range $0.3 \leq r/R_{200} \leq 1$.

4.3 Deriving the Escape Velocity Suppression due to Projection Effects

It was shown (*Miller et al.*, 2016; *Stark et al.*, 2016a) that the radial escape-velocity profiles of galaxy clusters are a promising and competitive probe of cosmology in an accelerating universe. However, projection effects produce a significant systematic uncertainty as the observed line-of-sight galaxy positions and velocities suppress the 3-dimensional escape-velocity edge. To predict this level of the suppression (Z_v), we utilize Keplerian orbital dynamics to numerically model cluster projected phase-spaces. The test of the approach on N-body simulations shows that the developed approach models the edge suppression to $\sim 2\%$ accuracy and with $\sim 5\%$ precision for massive ($> 10^{14} M_{\odot}$) systems over the range $0.4 \leq r/r_{200} \leq 1$. We showed that the true 3-dimensional escape velocity profile can be observed in projected phase-spaces with high enough richness. Moreover, we showed that the suppression is a function of richness (N) only as it is anisotropy, mass and cosmology independent. This allows us to model the suppression with a simple power-law model ($Z_v \sim N^{-0.5}$). Note, that no other information except richness is required to predict the projected suppression. Our conclusion is that full 3D escape velocity profiles can be inferred from the projected phase-spaces without knowledge of cosmology or the use of simulations. One additional conclusion of our work is that it is possible to predict escape velocity profiles based on mock clusters with galaxies which do not interact directly (the only interaction is a global gravitational field created by all the massive objects in the clusters and described by spherically symmetrical models such as Einasto and NFW) as we populate our clusters with random galaxies on Keplerian orbits. This observation potentially leads to the conclusion that most of non-merging clusters are relaxed and

3-body interactions are rare. However, deeper investigation of this argument needs to be done.

4.4 Probing ΛCDM Model with Weak Lensing and Escape Velocity Profiles of Galaxy Clusters

Direct utilization of the suppression derived in the chapter III is done to test standard cosmological model on the set of 38 galaxy clusters, which contains well-sampled radius/velocity phase-space data and weak lensing mass profiles. Our preliminary results are the following: in an accelerating flat ΛCDM universe with fixed equation of state ($\omega = -1$), we constrain the matter energy-density $\Omega_{m,0} = 0.325^{+0.014(stat)+0.003(sys)}_{-0.021(stat)-0.001(sys)}$ and the Hubble constant $h_0 = 0.733^{+0.007(stat)+0.035(sys)}_{-0.006(stat)-0.029(sys)}$ with the systematic error budget coming from ±5% uncertainties on the weak lensing mass calibration and ±5% uncertainties in the density model due to utilization of the NFW model, which significantly overestimates escape velocity profiles. Our preliminary the best-fit results favor the matter energy-density inferred from Plank CMB (*Planck Collaboration et al.*, 2018), while agreeing with the Hubble constant measured by Cepheids (*Riess et al.*, 2019). Alternate techniques, such as the one we present in our work, to independently constrain h_0 are vital to resolve a very significant tension ($> 4.4\sigma$) between observations of the Hubble constant by analyzing Cepheids and from Plank CMB observations.

4.5 Preliminary results of constraining cosmological parameters Ω_m and H_0 using galaxy clusters weak lensing and escape velocity profiles

4.5.1 Abstract

As we showed in the chapter III, one can quantify the level of the suppression of the observed escape velocity profile of galaxy clusters using an analytical representation of Keplerian orbits in a cosmological background. This section is devoted to the application of this suppression function to test cosmology: we apply it to a set of 38 observed galaxy clusters which contain well-sampled radius/velocity phase-space data and weak lensing mass profiles. Our preliminary results are the following: in an accelerating ΛCDM universe, we constrain the matter density $\Omega_{m,0} = 0.325^{+0.014(stat)+0.003(sys)}_{-0.021(stat)-0.001(sys)}$ and the Hubble constant $h_0 = 0.733^{+0.007(stat)+0.035(sys)}_{-0.006(stat)-0.029(sys)}$. The systematic error budget includes $\pm 5\%$ uncertainties on the weak lensing mass calibration and $\pm 5\%$ uncertainties in the density model differences between the NFW and the Einasto functions.

4.5.2 Introduction

In the ΛCDM paradigm, the way our Universe is dynamically evolving is governed by general relativity (GR). There are several cosmological observations which require adjustments to the simplest GR theory such as the requirements for dark matter (DM) and dark energy (DE). These are non-trivial additions, as they not only sum up to around %95 of the total matter density of the universe, but their study has dominated the cosmological research landscape for decades.

While the first indirect proof of the existence of DE came rather recently from the observation of the accelerated expansion of the universe from the supernova Ia (*Riess et al.*, 1998), the first signs of the need for DM came in the first half of the 20th century from deviations from the virial theorem in observations of Coma

cluster (*Zwicky*, 1933). The search for the explanation of DM has continued since then and includes dynamical measurements of galaxy rotation curves (*Rubin and Ford*, 1970), statistical measurements from temperature fluctuations in the Cosmic Microwave Background (CMB) (*Ade et al.*, 2016), and more direct visual evidence from the separation of the weak lensing shear structure compared to the X-ray gas structure in the Bullet cluster (*Clowe et al.*, 2006). In this work, we will present the results of a new probe of DM with high precision.

In addition to DE and DM, the Hubble parameter (H_0) is of equal importance, since it characterizes the expansion speed of the universe. We are beginning to see tension arise between the measurement of H_0 on local scales (e.g., from Cepheid variable distances) and inferences of H_0 in the distant universe (e.g., Planck) (*Riess et al.*, 2019). Alternate techniques to independently constrain H_0 are vital, such as the one we present here.

In this current manuscript we focus on testing the standard ΛCDM cosmological model using a new probe based on data from galaxy clusters. This probe was first discussed in *Miller et al.* (2016) and *Stark et al.* (2016a) and connects the observed escape velocity profile, the weak lensing density profile, and the term qH^2, where q is the classic deceleration parameter. For the probe to be successful, we require well sampled cluster radius/velocity phase-spaces and reasonably precise weak lensing mass profiles.

A key development in this effort was the recent work by Halenka & Miller 2019 (hereafter HM19 and it is referred to the chapter III), which enables an analytical determination of the suppression of the observed maximum velocity profile. This suppression can be calculated numerically and it is a function of the number of galaxies per cluster only. HM19 tested their predictions in simulations and found percent level precision and accuracy. Without this quantification of the 2D projection in the phase-space, the systematic errors associated with the technique would dominate the

error budget. Our data set contains 38 galaxy clusters with enough phase-space data to provide $6-10$ degrees of freedom per cluster depending on a binning procedure applied. Therefore, we have ample data to make statistically precise constraints on the cosmological parameters. We note that unlike the mass function or the spatial correlation function of clusters, this probe and its associated theory does not require calibration to output from N-body simulations.

We start our paper with the section 4.5.3 where the description of the effects of accelerating universe on escape velocity profiles is presented. Section 4.5.4 introduces description of projection effects as well as procedure of measuring escape and observed maximum velocity profiles. Data used in our paper is described in the section 4.5.5. The Bayesian approach used to statistically analyze data is described in the section 4.5.6. Section 4.5.7 presents results of constraining cosmological parameters. We finish with discussion and conclusions in the section 4.5.8.

Similarly to the previous chapters, we refer in this section to the R_{200} and M_{200}, which are the radius and the mass of the clusters at the point when the density drops to $200\rho_{c,z}$, where $\rho_{c,z} = 3H^2(z)/(8\pi G)$ is the critical density of the universe at redshift z and $H^2(z) = H_0^2(\Omega_{\Lambda,0}(1+z)^{3(1+\omega)} + \Omega_{m,0}(1+z)^3)$, where ω is the equation of state (EOS) and superscript $_0$ denotes present values of cosmological parameters. The connection between R_{200} and M_{200} is by definition the following: $M_{200} = \frac{4\pi}{3}(200\rho_{c,z})R_{200}^3$. In addition to that, everywhere in this section a flat standard cosmology is assumed. The weak lensing data provided by *Sereno* (2015) meta catalog uses $\Omega_{m,0} = 0.3$, $\Omega_{\Lambda,0} = 1 - \Omega_{m,0}$ and $H_0 = 100h_0$ km s^{-1} Mpc^{-1} with $h_0 = 0.7$ as a benchmark.

4.5.3 Escape velocity profile in an expanding universe

4.5.3.1 Cosmological effect on escape velocity profile

In general, to infer escape velocity profile in ΛCDM universe one needs to integrate Poisson equation up to infinity which produces result not consistent with observations as the gravity potential at infinity is poorly defined. Instead the integration should be done until equilibrium radius r_{eq} (1.46), which is a function of deceleration parameter (1.47). At this distance gravity pull from matter is equal to the gravity push due to DE which means that to correctly infer dynamical mass from the escape velocity profiles some underlying cosmology should be utilized. This leads to the modification of the connection between escape velocity and gravity (1.48).

In general, deceleration parameter (1.47) is a function of a scale factor

$$q(a) = -\frac{\ddot{a}a}{\dot{a}^2}, \tag{4.1}$$

where dot denotes time derivative. More direct description of the acceleration of the Universe is presented by parameter that combines both deceleration parameter and the square of Hubble parameter ($H(a) = \dot{a}/a$)

$$qH^2 = -\frac{\ddot{a}}{a}. \tag{4.2}$$

While generally speaking v_{esc} (1.48) is a function of several cosmological parameters (for a flat Universe on the late stage of its evolution: energy-densities of matter and DE, Hubble constant and EOS), they all can be combined into only one parameter qH^2 and v_{esc} provides us with direct measure of it (see expressions 1.46 and 1.48). It should be noted that below we use parameter qH^2/H_0^2 instead of (4.2), which is done to account for the present speed of the expansion of the Universe.

4.5.3.2 Correction to the escape velocity profile

While the data are given in the NFW form (1.36), one needs to work with the Einasto model 1.38 instead. Recently, it was shown that the dark matter mass profiles of the galaxy clusters in simulations prefer profile in the Einasto form (1.38) as the NFW form tends to overestimates the matter density in the outskirts of the galaxy clusters (*Diemer and Kravtsov*, 2015) (i.e. the total mass inside some spherical region increases as a function of radius r without converging to any particular number) and this is due to the shape of the NFW model (1.36) which is an inverse power-law and it can not fall as quickly as exponential expression such the one Einasto model uses to correctly describe density profile of galaxy clusters at high radii (i.e. $r > R_{200}$). It should be noted that both of these profiles work great in the inner region up to R_{200} (*Sereno et al.*, 2016) and start to split afterwards, so this does not produce any negative consequence for those who are working with density profiles in the inner regions of galaxy clusters.

The NFW density overestimation leads to the significant overestimation of the escape velocities (*Miller et al.*, 2016) starting from the cores of the clusters. This is due to the gravitational potentials (and v_{esc} subsequently) being derived using Poisson equation by integrating density all the way up to ∞ (or up to r_{eq} in the expanding with the acceleration Universe (*Behroozi et al.*, 2013a))

$$\phi(r) = -4\pi G\Big(\frac{1}{r}\int_0^r \rho(r')(r')^2 dr' + \int_r^\infty \rho(r') r' dr'\Big). \tag{4.3}$$

On the other hand, due to correct prediction of the density profiles by the Einasto model all the way up to $\sim 2.5h^{-1}$Mpc (*Miller et al.*, 2016), v_{esc}, predicted by the Einasto potential (1.43) using parameters from fitting densities of the simulated halos with the Einasto density model (1.38), correctly describes the true measured escape velocity profiles.

The most straightforwards way to solve the NFW overestimation problem is by directly transferring the NFW density to the Einasto and the description of this procedure is done in *Stark et al.* (2019); *Halenka and Miller* (2018). By following these prescriptions we are able to fit the NFW density model with the Einasto model to a high precision ($\sim 0.5\%$ accuracy) in the region $0 \leq r/R_{200} \leq 1$. However, the Einasto model successfully reproduces the NFW density all the way up to several R_{200} without showing any signs of steeper than the NFW model shape. This is due to the fact that the NFW model utilizes the inverse power-law (1.36), which can not be as steep as the exponential form of the Einasto model (1.38) and as the actual density profiles of the galaxy clusters. However, the Einasto model can be as flat as the NFW model. In other words, one can fit the Einasto model to the flatter NFW model, but one can not always fit NFW to the steeper Einasto or simulated density profiles.

To account for the NFW overestimation of v_{esc}, we apply the linear escape velocity correction motivated by the Millennium simulations (*Springel et al.*, 2005) and exported directly from *Miller et al.* (2016)

$$v_{corr} = 0.021 + 0.104 R_{200}, \tag{4.4}$$

which is equal to ~ 0.075 at $0.3R_{200}$ and ~ 0.125 at $0.3R_{200}$. These numbers are measured at $\sim 0.57h^{-1}$ Mpc and $\sim 1.89h^{-1}$ Mpc, so they correspond to $0.3R_{200}$ and R_{200} of the galaxy clusters utilized in the current work (the average R_{200} of the data sample is 1.89 Mpc). The velocity correction suppresses the escape velocity profile

$$v_{esc,corr} = (1 - v_{corr}) v_{esc}. \tag{4.5}$$

We apply $\sim 2-3$ times wider than presented in *Miller et al.* (2016) uncertainty on escape velocity correction ($dv_{corr} = 0.05$) to account for possible mass and cosmology

dependence of the velocity correction. Moreover, we account for 0.05 contribution to the systematic uncertainty due to the escape velocity correction.

Note, to account for cosmology we need not only to use correct expression of the escape velocity (1.48), but also change matter parameters accordingly as they are provided for a fixed cosmology (see last paragraph of the section 4.5.2). As we can see, M_{200} is a function of critical density ($\rho_{c,z}$), which is in turn function of cosmological parameters ($\Omega_{m,0}, h_0$) and redshift (z). Subsequently, concentration parameter (1.37) changes with cosmology as well due to being proportional to M_{200}. Unfortunately, we do not have direct measurements of the matter density profiles in cosmology independent manner, so we need to treat one of three matter parameters ($M_{200}, R_{200}, C_{200}$) as cosmology independent. Our choice is radius R_{200}, which stays unchanged for different cosmological parameters, while both M_{200} and C_{200} account for cosmology. It should be noted, that direct shear measurements of the weak lensing is preferred as it is cosmology independent, so all the cosmological contribution is in qH^2 parameter and not in ($M_{200}, R_{200}, C_{200}$), which would allow us to directly utilize one parameter (qH^2) fit to the data. Moreover, by using shear measurements we can directly fit density profile to the Einasto model, which would dramatically decrease the error contribution from the escape velocity correction (4.4) due to the NFW density overestimation.

[1]The original papers are cited above, but actual weak lensing masses (and their respective errors) we use in our analysis were taken from the *Sereno* (2015) meta catalog. More specifically, *Sereno* (2015) standardizes the M_{200} masses for the clusters shown above (as inferred from each reference listed in the "weak lensing" column) for the fiducial cosmology mentioned in our introduction.

[2]Positions and redshifts of the galaxies from the cluster. The abbreviations in this column refer to the following papers: R13 = *Rines et al.* (2013), M08 = *Maurogordato et al.* (2008), T13 = *Tyler et al.* (2013), OW11 = *Owers et al.* (2011), G08 = *Girardi et al.* (2008), A16 = *Agulli et al.* (2016), T07=*Tran et al.* (2007), T15 = *Treu et al.* (2015), M07 = *Moran et al.* (2007), D10 = *Demarco et al.* (2010), H14 = *Hwang et al.* (2014), G14 = *Geller et al.* (2013), G15 = *Girardi et al.* (2015), E11 = *Edwards and Fadda* (2011), F17 = *Foëx et al.* (2017), B09=*Boschin et al.* (2009).

[3]The abbreviations in this column refer to the following papers: H15= *Hoekstra et al.* (2015), OK08 = *Okabe and Umetsu* (2008), OK10 = *Okabe et al.* (2010), OK15= *Okabe and Smith* (2015), CL00=*Clowe et al.* (2000), S13=*Sereno and Covone* (2013), A14 = *Applegate et al.* (2014), C04 = *Cypriano et al.* (2004), D06 = *Dahle* (2006), H11=*Huang et al.* (2011), P07 = *Pedersen and Dahle* (2007), R08 = *Radovich et al.* (2008), M16 = *Medezinski et al.* (2016), D02 = *Dahle et al.* (2002), F12 = *Foëx et al.* (2012), S97 = *Smail et al.* (1997), H12 = *High et al.* (2012), U15= *Umetsu et al.*

Table 4.1: List of Galaxy Clusters and References

Cluster [1]	z	Galaxies [2]	Weak lensing[3]	M_{200} $(10^{14}M_{\odot})$	dM_{200} $(10^{14}M_{\odot})$	N[4]
A1246	0.192	R13	H15	7.44	1.92	64
A1682	0.227	R13	P07	6.05	3.48	66
A1553	0.167	R13	C04	7.65	4.18	86
A1423	0.214	R13	OK15	6.7	1.59	82
A2163	0.201	M08	H15/R08	16.33	3.04	207
A2034	0.113	R13	OK08	8.09	4.85	102
A2029	0.077	T13	C04	10.28	1.88	284
A2009	0.152	R13	OK10	4.95	1.33	77
A2219	0.226	R13	OK10/OK15/A14	15.33	2.9	183
A2744	0.306	OW11	M16	20.6	4.2	175
A520	0.201	G08	OK15	12.75	2.5	100
A959	0.288	B09	D02	7	2.17	54
A85	0.055	A16	C04	7.24	1.97	296
A773	0.217	R13	OK15/D06	15.45	4.7	79
ZwCl3146	0.289	R13	OK15	7.94	1.53	41
BLOXJ1056	0.831	T07	CL00	5.63	2.25	90
MACSJ0717	0.546	T15	U15	26.57	5.32	228
MCXCJ0454	0.54	M07	F12	14.8	2.8	136
RXJ1720	0.16	OW11	OK15	8.3	2.54	210
RXJ0152	0.837	D10	S13	3.68	1.16	73
A2111	0.229	R13	H15	8.08	1.94	70
ZwCl0024	0.395	M07	S97	4.15	1.68	80
A2259	0.161	R13	H15	6.74	2.08	59
A697	0.281	H14	OK15	13.96	2.86	120
A1689	0.184	R13	OK15	16.39	2.28	109
A1914	0.166	R13	H15	11.2	1.99	133
A1835	0.251	R13	H15	16.88	3.02	107
A267	0.229	R13	OK15	9.07	1.56	108
A1763	0.231	R13	H15	14.13	2.93	97
A963	0.204	H14	OK10	8.64	1.74	117
A383	0.189	G14	H11	7.04	1.94	91
A2142	0.09	OW11	OK08	13.63	5.98	527
RXCJ2129	0.234	R13	OK15	7.24	2.01	59
A2631	0.277	R13	OK15	12.34	3.84	63
MACS1206	0.44	G15	A14	13.67	5.44	146
Coma	0.023	E11	OK14	10.26	2.94	118
RXCJ0516	0.295	F17	H12	9.48	3.42	42
A2537	0.297	F17	OK15	11.36	2.84	128

4.5.4 Connecting theory with the data

Galaxy clusters are positioned on a high distance away from us, which places constraint on our ability to observe clusters only from one position. This limitation distorts the way we observe both the escape velocity profiles and the phase-spaces in general.

(2015). We averaged over multiple weak lensing sources to get M_{200} as well as the errors of the clusters A2163, A2219 and A773.

[4]Number of galaxies in the range $0.3 \leq r/r_{200} \leq 1$.

4.5.4.1 Projection effects

To build phase-space from a given observational data of galaxies and then infer maximum observed velocity profile ($v_{los,esc}$), we follow specific procedure. First, we get v_{los} - galaxy velocities along ling-of-sight (1.50). Besides that, we calculate r_g - the physical projected distance from a galaxy to the center of the galaxy cluster (1.49). Phase space (v_{los} vs. r_g) for each cluster is created by applying these two steps to all the galaxies of the cluster.

To infer maximum observed velocity profiles ($v_{los,esc}$) from the phase-spaces, we find galaxies which have the top 1% velocities in each of the 0.2 Mpc radial bins, which is done by following interloper removal prescription proposed by *Gifford et al.* (2013). It was shown by *Miller et al.* (2016) on N-body simulations that the escape velocity profiles (v_{esc}) can be obtained with approximately 5% accuracy. v_{esc} (black dashed lines on the figure 4.1) describes 3-dimensional escape velocity profile and it is a measure of the effective gravitational potential, while $v_{los,esc}$ (black solid lines on the figure 4.1) is created by galaxies with the maximum velocities on the projected phase-space diagram and it is a suppressed version of v_{esc} due to observing clusters in 2-dimensional perspective. In general, this suppression is significantly larger than the effect due to change in cosmology (compare the difference between red lines and black dashed lines with the difference between black solid and black dashed lines on the figure 4.1).

4.5.4.2 Quantifying the suppression

To connect escape velocity profile and maximum observed velocity profile, we follow HM19 results and the approach which was introduced in the chapter III. A thorough discussion and introduction of the approach is presented in the chapter III, while this subsection aims to provide a brief description of this approach.

The goal of the approach is to produce an easy way to describe $v_{los,esc}$ and the

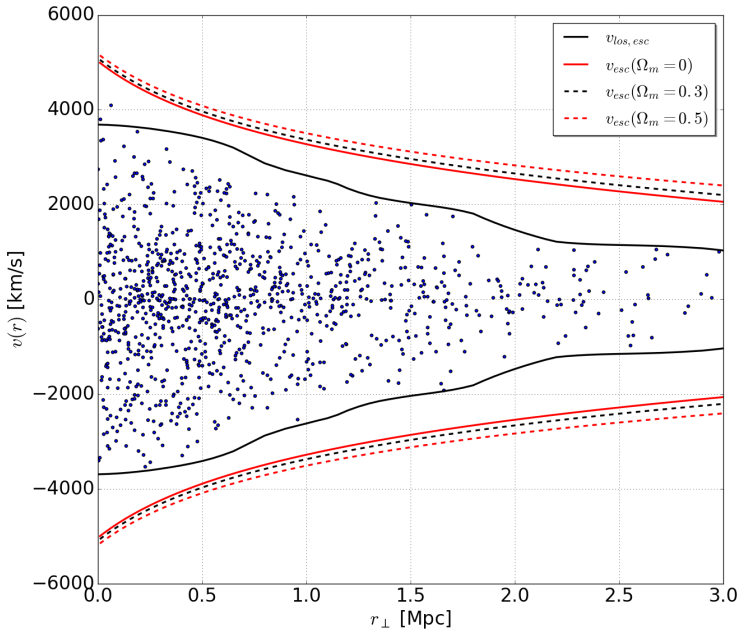

Figure 4.1: An example of a projected phase-space of an individual cluster created by the approach with a measured maximum observed velocity $v_{los,esc}$ (black solid) and the unsuppressed 3-dimensional escape velocity profile v_{esc} (black dashed). Red solid (dashed) lines correspond to the cosmology with $\Omega_{m,0} = 0, \Omega_{\Lambda,0} = 1$ ($\Omega_{m,0} = 0.5, \Omega_{\Lambda,0} = 0.5$). One can see a significant difference between $v_{los,esc}$ and v_{esc} due to the projected suppression (4.7).

ratio between the escape velocity profile and the maximum observed velocity profile

$$Z_v(r) = \frac{v_{esc}(r)}{v_{los,esc}(r)}. \tag{4.6}$$

This is done by creating clusters which are populated by galaxies on Keplerian orbits in a vicinity of gravitational potential created by a galaxy cluster and modified due to cosmological background. While the procedure is done randomly, all together these galaxies has to satisfy several conditions such as they need to be on Keplerian orbits on which galaxies do not have $r > r_{eq}$ at any point on their orbit, galaxies should be distributed so they create a density profile which mimics weak lensing profile and in total there should be the same number of galaxies in the range $0.3 \times R_{200} - R_{200}$ as

in a given system.

This analytical approach allows us to have a controlled environment, so we can create a cluster which would precisely mimic needed requirements of a given system (this is in contrast to a traditional N-body simulations where a lot of computational power is required to simulate such cluster and it is hard to create systems with the same characteristics as given clusters, which in turn leads to a high level of uncertainty in quantifying v_{esc} suppression due to the projection effects).

By applying this approach, the independence of the velocity ratio Z_v (4.6) from cosmology $(\Omega_{m,0}, h_0)$ and cluster masses was shown in the chapter III as well as that Z_v is a function of the number of galaxies per cluster (N) only and with a high enough number of galaxies, one can potentially reconstruct actual escape velocity profile even in projected phase-space, i.e. $Z_v \to 1$ for $N \to \infty$. The functional form can be fitted with a simple power-law (3.49)

$$Z_v(N) = 1 + \Big(\frac{N_0}{N}\Big)^{\lambda}, \tag{4.7}$$

where N_0 and λ are the parameters of the model, N represents the number of galaxies in the range $0.3 \leq r/R_{200} \leq 1$ and the best-fit parameters, which were derived by analyzing simulated data set as well as by using the analytical approach, are $N_0 = 14.205, \lambda = 0.467$ (the bottom error bar line: $N_0 = 3.213, \lambda = 0.392$, the top error bar line: $N_0 = 35.822, \lambda = 0.454$). These are the main results of the analytical approach which we directly utilize to place constraints on cosmological parameters.

4.5.5 Data

In this section we present the data we are using in our analysis. We start with describing matter density content of the galaxy clusters measured by using weak lensing, then we move to the description of the positions and redshifts of the galaxies

and we finish with the description of the data selection criteria.

4.5.5.1 Total mass

In our analysis we utilize inferred total mass profiles for a set of 38 galaxy clusters. The weak lensing data are given in the NFW formulism (1.36). The weak lensing data give us the information about the size and the total mass of the clusters: M_{200} and uncertainty dM_{200} of individual clusters are listed in the table 4.1. Most of the weak lensing data are taken from Sereno meta catalog (*Sereno*, 2015) which lists results from other works. Names of the clusters together with the initial references are listed in the table 4.1 (see footnotes for the meanings of the abbreviations). Note, all the weak lensing parameters are presented for a fixed cosmology $\Omega_{m,0} = 0.3$, $\Omega_{\Lambda,0} = 1 - \Omega_{m,0}$ and $H_0 = 100h_0$ km s^{-1} Mpc^{-1} with $h_0 = 0.7$. We change weak lensing parameters to account for cosmology change (see section 4.5.3).

The weak lensing masses (radii) of the 38 galaxy clusters are spread in the wide region $3.68 \times 10^{14} M_\odot \leqslant M_{200} \leqslant 2.66 \times 10^{15} M_\odot$ (1.08 Mpc $\leqslant R_{200} \leqslant$ 2.36 Mpc) with the mean mass (radius) $< M_{200} >= 1.07 \times 10^{15} M_\odot$ ($< R_{200} >=$ 1.89 Mpc). Most of the clusters have redshifts withing a tight range around $z = 0.2$ while individual cluster redshifts are ranged $0.023 \leqslant z \leqslant 0.837$ with the mean redshift $< z >= 0.26$. Number of galaxies of individual clusters cover a very wide range $[41; 527]$ with the mean (median) number of galaxies 127 (101). While the total number of galaxies provided by the data catalogs are actually higher, the above numbers describe number of galaxies in the range $0.3 \leq r/R_{200} \leq 1$ to comply with the definition of the suppression function.

4.5.5.2 Galaxy positions and redshifts

Positions and redshifts of individual galaxies were taken from various sources which are listed in the table 4.1 (see footnotes for the meanings of the abbreviations).

The data transformation procedure to the phase spaces as well as the way escape velocity profiles are inferred from the phase spaces against which theoretical models are tested are described in the section 4.5.4.

4.5.5.3 Data selection criteria

The following selection procedure was followed to create a list of the galaxy clusters (see table 4.1):

1. Only clusters with the available in the Sereno meta catalog (*Sereno*, 2015) weak lensing profiles were selected.

2. By using "SIMBAD Astronomical Database - CDS (Strasbourg)", only clusters with high enough total number of galaxies (50+) were further selected.

3. By visually inspecting phase-spaces, the galaxy clusters which exhibit a significant drop in the measured $v_{los,esc}$ at high radii due to a small number of galaxies in the outskirts ($\sim 0.6 < r/r_{200} < 1$) were dropped. Merging systems were dropped as well.

While the selection procedure was not very strict, it allowed, nevertheless, to create a high quality data set of 38 galaxy clusters.

4.5.6 The Bayesian approach

For our statistical analysis, we will be comparing the observed line-of-sight escape velocity measured for our 38 clusters against the predicted $v_{los,esc}$ given some cosmological parameters, a cluster redshift (z), and the number phase-space projected galaxies within $0.3 \leq r/r_{200} \leq 1$ (N). The predicted $v_{los,esc}$ is:

$$v_{los,esc} = (1 - v_{corr}) v_{esc}(M_{200}, qH^2, z)/Z_v(N), \tag{4.8}$$

where M_{200} comes from the measured weak lensing mass, v_{corr} is the NFW correction term and $Z_v(N)$ is the suppression term which is based on N. For a flat ΛCDM universe, equation 4.8 becomes:

$$v_{los,esc} = (1 - v_{corr})v_{esc}(M_{200}, \Omega_{m,0}, h_0, z)/Z_v(N), \tag{4.9}$$

We specifically choose a Bayesian analysis so that we can incorporate the statistical and systematic error on the weak lensing masses, the statistical error on the suppression term, and the statistical and systematic error on the NFW correction term. For equation 4.9, we choose a Gaussian likelihood for each radially observed measurement of $v_{los,esc}$. We treat each measurement as independent with binning of $0.1 \times r_{200}$. This binning is wide enough so that we expect very little correlations between the bins, which would be caused by mis-identified interlopers (see *Stark et al.* (2017) for more details). We then maximize the sum of the log-likelihoods. We treat the other observables as random variables and simultaneously constrain the values of M_{200}, the suppression Z_v and the velocity correction v_{corr}. However, unlike the observed $v_{los,esc}$, these other parameters have priors as described below. We then examine the posterior distributions of the interesting free parameters $\Omega_{m,0}$ and h_0 and infer the best-fit values and their uncertainties.

The measured maximum observed velocity at any given radius is treated as a normally distributed observable

$$a_{0i} \sim \mathcal{N}(a_i, \sigma_{a_i}^2), \tag{4.10}$$

where a_i is the underlying true maximum observed velocity profile and $\sigma_{a_i} = 50$ km/s is the uncertainty on the measurement. This error corresponds to a typical redshift uncertainty with modern instruments like HECTOSPEC, which is used for much or our data (*Rines et al.*, 2013).

Each cluster's weak lensing M_{200} is treated as being a normally distributed observable

$$b_{0i} \sim \mathcal{N}(b_i, \sigma_{b_i}^2), \tag{4.11}$$

where σ_{b_i} is the observed M_{200} uncertainty and b_i is the underlying cluster M_{200} mass. Since in practice b_i is an observed property, we treat it statistically for each cluster by modeling it as a Gaussian drawn from the full underlying distribution of our weak lensing masses

$$b_i \sim \mathcal{N}(\mu_{b_i}, \sigma_{\mu_{b_i}}^2), \tag{4.12}$$

where $\mu_{b_i} = 1.07 \times 10^{15} M_\odot$ ($\sigma_{\mu_{b_i}} = 4 \times 10^{14} M_\odot$) and equal to the mean (variance) of the masses of the galaxy clusters in our sample, which fits our dataset well. By treating M_{200} as a random variable, we then constrain it as a nuisance parameter in the final analysis.

The suppression function is treated as being normally distributed observable

$$d_{0i} \sim \mathcal{N}(d_i, \sigma_{d_i}^2), \tag{4.13}$$

where σ_{d_i} is the uncertainty of the suppression Z_v and d_i is the underlying Z_v suppression. The suppression function and its error is calculated analytically for each cluster as described in HM19. This function depends on the observed projected phase-space galaxy count within $0.3 \leq r/r_{200} \leq 1$. This functional representation of the edge suppression has cluster-cluster variance which is also modeled in HM19 and confirmed against N-body simulations. Since this suppression is based on the observed properties of the clusters, we treat it as a random variable drawn from a Gaussian:

$$d_i \sim \mathcal{N}(\mu_{d_i}, \sigma_{\mu_{d_i}}^2), \tag{4.14}$$

where $\mu_{d_i} = 1.41$ ($\sigma_{\mu_{d_i}} = 0.15$) and equal to the mean (variance) of the values

of the suppression of the galaxy clusters in our sample. As with M_{200}, we treat the suppression term as a nuisance parameter which is constrained against the "observed" corrections based on the richness for each cluster.

Finally, we also use a normal distribution to define the NFW velocity correction

$$f_{0i} \sim \mathcal{N}(f_i, \sigma^2_{f_i}), \tag{4.15}$$

where the uncertainty is fixed $\sigma_{f_i} = 0.05$ and μ_{f_i} is modeled as uniformly distributed in the range $[0.025; 0.0175]$, which is 0.05 wider than the range of the values we work with (see description to the 4.4). These values are taken from simulations (*Miller et al.*, 2016).

Overall, the Bayesian model regresses against the 4 observed quantities: observed maximum velocity profile, M_{200} masses, suppression function and velocity correction. The parameters of our interest are $\Omega_{m,0}$ and h_0, while the rest of the parameters are marginalized over for presenting posterior probability distributions. We treat the parameters we are interested in as uniformly distributed in wide ranges

$$h_0 = [0.5; 0.9] \tag{4.16}$$

$$\Omega_{m,0} = [0; 0.6]. \tag{4.17}$$

Overall, we utilize in our analysis 36 clusters. We drop 2 clusters for this analysis due to their high redshifts which is discussed in the subsection 4.5.7.1. We are using 8 radial bins per cluster from $0.3 \leq r/r_{200} \leq 1$ (see blue error bars on the projected phase-spaces of each of 38 galaxy cluster in Appendix A), summing to $N_{d.o.f.} = 288$ degrees of freedom before accounting for the parameters.

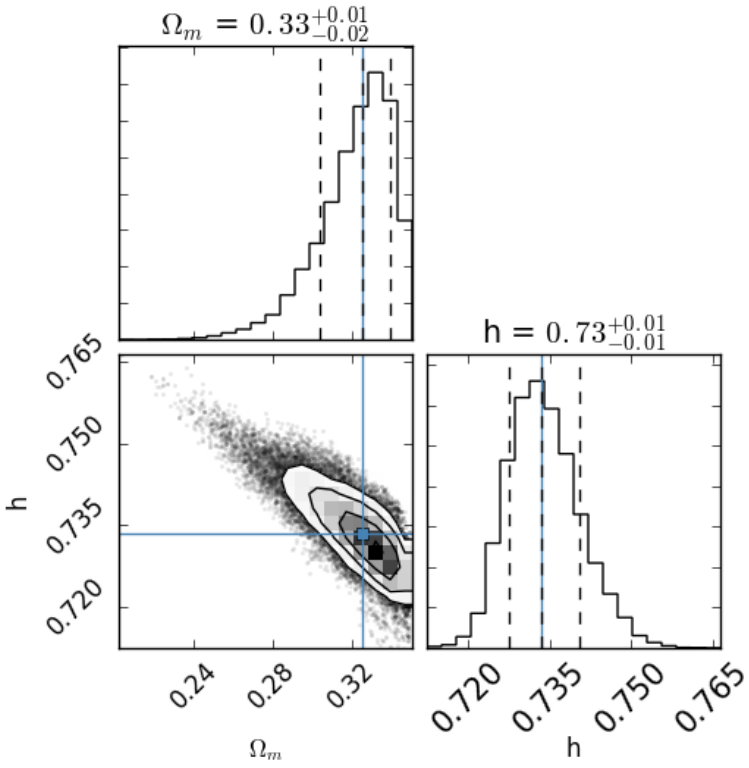

Figure 4.2: The posterior distribution function for $\Omega_{m,0}$ and h_0 for the data sample of 36 galaxy clusters.

4.5.7 Results

Both escape velocity profile v_{esc} and maximum observed velocity profile $v_{los,esc}$ change with cosmology. However, as it was pointed out in section 4.5.4, they do it in synchronized way leading to their ratio staying without change for different cosmologies while only changing with the number of galaxies. This creates a room for us to probe cosmology, as we know $v_{los,esc}$ from measured phase-space and can vary v_{esc} based on cosmology to match the true velocity ratio Z_v (4.7) with the best-fit parameters $N_0 = 14.205, \lambda = 0.467$ (the bottom error bar line: $N_0 = 3.213, \lambda = 0.392$, the top error bar line: $N_0 = 35.822, \lambda = 0.454$).

4.5.7.1 $\Omega_{m,0}, h_0$ statistical analysis

As it was discussed in the previous section, we probe cosmology by using Bayesian statistical approach. We make a two parameters fit: $\Omega_{m,0}$ and Hubble constant h_0. Equation of state parameter is fixed ($\omega = 1$) and we neglect curvature of the Universe ($\Omega_c = 1$), which allows us to connect the energy densities of dark energy and matter ($\Omega_{\Lambda,0} = 1 - \Omega_{m,0}$).

Note, two clusters (BLOXJ1056 and RXJ0152) have redshifts higher than the redshift when the Universe started to expand with an acceleration. For the standard cosmology (i.e. $\Omega_{m,0} = 0.3$) it is equal to $z_{eq} \approx 0.67$ and for the higher redshifts there is no defined equilibrium radius r_{eq}. For this reason, escape velocity profile of these two clusters has simplified expression $v_{esc}(r) = \sqrt{-2\phi(r)}$ as we need to integrate up until infinity, where potential is equal to zero. However, these two clusters still exhibit cosmology dependence through mass profile parameters, since M_{200}, C_{200} and R_{200} change with cosmology. These two clusters are not used in this subsection, but they will be used in the next subsection.

In general, due to the transition from the deceleration to the accelerated expansion, we need to apply a step function, which defines transition of v_{esc} at different acceleration stages of the Universe, i.e. for the case when $qH^2 < 0$ we use the full version of v_{esc} (1.48), while for $qH^2 > 0$ the simple version $v_{esc} = \sqrt{-2\phi}$ should be utilized. The redshift of the transition is calculated for each set of cosmological parameters individually by setting l.h.s. of the expression 1.47 to zero (i.e. $\Omega_m(z) - 2\Omega_\Lambda(z) = 0$ in the case $\omega = -1$), which in general is a function of $\Omega_{m,0}$ and ω

$$\Omega_{m,0}(1+z)^3 + (1+3\omega)(1-\Omega_{m,0})(1+z)^{3(1+w)} = 0. \tag{4.18}$$

Solving above equation leads to the functional expression of the redshift of the tran-

sition

$$z_{tr} = -\Big(\frac{\Omega_{m,0}}{(1+3\omega)(1-\Omega_{m,0})}\Big)^{1/(3\omega)} - 1, \tag{4.19}$$

which is in the case $\omega = -1$ simplifies to

$$z_{tr} = \Big(\frac{2(1-\Omega_{m,0})}{\Omega_{m,0}}\Big)^{1/3} - 1. \tag{4.20}$$

Statistical analysis of 36 clusters (without 2 high redshift clusters) provides the best-fit values

$$\Omega_{m,0} = 0.325^{+0.014(stat)+0.003(sys)}_{-0.021(stat)-0.001(sys)} \tag{4.21}$$

$$h_0 = 0.733^{+0.007(stat)+0.035(sys)}_{-0.006(stat)-0.029(sys)}. \tag{4.22}$$

The best-fit cosmological parameters posterior distributions are presented on the figure 4.2. Systematic error contribution comes from $\pm 5\%$ systematic uncertainty on the weak lensing mass calibration and extra $\pm 5\%$ systematic uncertainty is due to the uncertainties brought by velocity correction due to the NFW density overestimation (see subsection 4.5.3.2). One can notice an edge in the posterior distribution of the matter energy-density ($\Omega_{m,0}$). This is due to the acceleration transition redshift (4.20) discussed in the previous paragraph. It appears that at the redshifts close to z_{tr} the absolute values of the last 3 terms in 1.48 quickly drop to zero due to being proportional to qH^2, which approaches zero. This quick change in the functional behaviour of v_{esc} effectively leads to the extra prior on the upper limit of the uniform distribution of $\Omega_{m,0}$ (4.16). However, the analysis of the data sub samples with lower upper cuts on the range of allowed cluster redshifts does not produce significantly different results as they are withing $\sim 1\sigma$ standard deviation away from each other.

We note that the Plank constraints from cosmic microwave background are $\Omega_{m,0} =$

$0.315 \pm 0.007, h_0 = 0.674 \pm 0.005$ (*Planck Collaboration et al.*, 2018), Cepheids produce $h_0 = 0.7403 \pm 0.0142$ (*Riess et al.*, 2019) and SNIa $\Omega_m = 0.295 \pm 0.034$ (*Betoule et al.*, 2014a). Our results of fitting 36 galaxy clusters (4.21, 4.22) support Hubble constant from Cepheids, while agree with $\Omega_{m,0}$ from CMB. This potentially leads to the contradiction of decaying DM models, which are devised to easing the tension between observations of Hubble constant from CMB and Cepheids (*Berezhiani et al.*, 2015).

4.5.7.2 qH^2 statistical analysis

Statistical analysis in the previous subsection significantly supports acceleration expansion of the Universe and supports non-zero magnitude of the energy density of the dark energy with $> 5\sigma$ certainty. This result can be explicitly seen on Figure 4.3, where the value $q(z)H^2(z)/H_0^2$ is plotted. This figure is done by fitting cosmology for individual clusters and then individual magnitudes of $q(z)H^2(z)/H_0^2$ are combined into redshift bins. While similar to the described in section 4.5.6 Bayesian approach is utilized here, it is simplified as we analyze each cluster individually. The only observable is the maximum observed velocity, which we treat with the same distribution as in 4.10, but with the bigger uncertainty on the measurements ($\sigma_{a_i} = 100$ km/s) to partially account for dropping uncertainties of other observables, since M_{200}, Z_v and the velocity correction v_{corr} are all kept as fixed values provided by the data.

We analyze two sets of free parameters to reconstruct $q(z)H^2(z)/H_0^2$: $\Omega_{m,0}, h_0$ and $\Omega_{m,0}, h_0, \omega$ (ω is added to the list of free parameters in 4.9). Note, that in principle we can actually reduce number of parameter to one free parameter qH^2 in 1.48, but due to the weak lensing data being presented for the fixed cosmology, we need to have more free parameters, which in turn increases uncertainties and widens error bars. Ideally, by utilizing cosmology independent shear measurements, one can apply fitting procedure with one free parameter qH^2 and use H_0 from the analysis of the

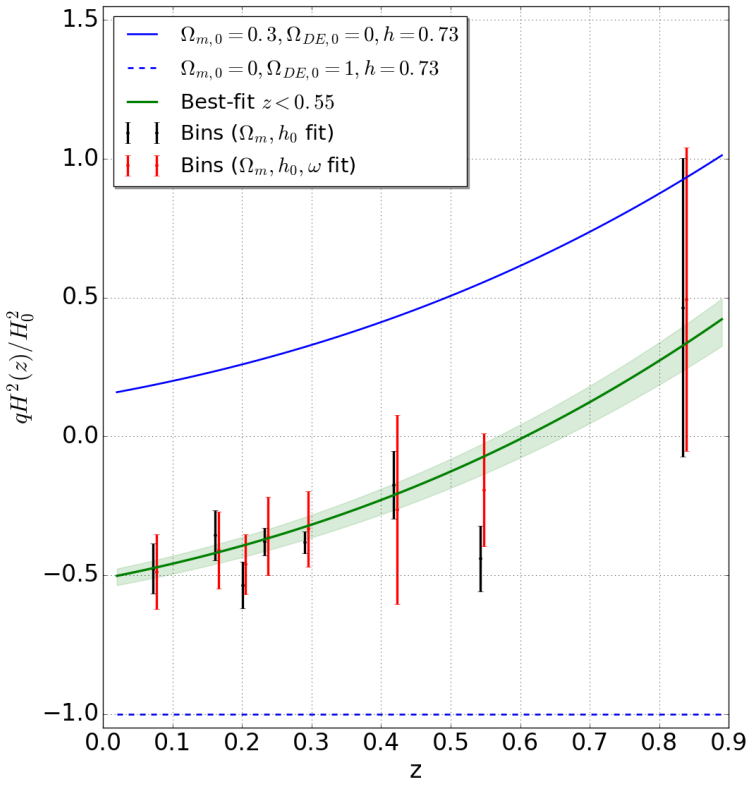

Figure 4.3: $q(z)H^2(z)/H_0^2$ as a function of redshift. Individual clusters are fitted and resulted values are combined into 8 redshift bins. Green solid line and shaded region around it correspond to the best-fit cosmology (4.21, 4.22). Black error bars correspond to the 2 free parameters fit $(\Omega_{m,0}, h_0)$ and red error bars to 3 free parameters analysis $(\Omega_{m,0}, h_0, \omega)$. Individual bins are the weighted means and the weighted error bars of several galaxy clusters, which are binned to account for possible splits in redshifts while having approximately equal number of galaxy clusters per bin. Solid (dashed) blue lines correspond to individual cosmologies with cosmological parameters described in the legend. Overall, we see very good agreement between individual bins (black and red error bars) and the best-fit cosmology from fitting 36 clusters (green line).

previous subsection to reconstruct (qH^2/H_0^2 vs. z) plot.

Overall, both 2 and 3 free parameters fitting approaches agree well with $q(z)H^2(z)/H_0^2$ plotted using best-fit parameters (4.21, 4.22), while 3 free parameters analysis produces better overall agreement having wider error bars due to the extra free parameter (see Figure 4.3). Moreover, we see good agreement of two very high redshift clusters (which were not included in the analysis in the subsection 4.5.7.1) with the best-fit parameters (see the tall error bar at $z \sim 0.84$).

4.5.7.3 Velocity ratio as a function of the number of galaxies per cluster

Individual escape velocity profiles for the best-fit cosmology (4.21, 4.22) of each of the 38 galaxy clusters together with measured $v_{los,esc}$ and later adjusted due to the suppression function (4.7) and the velocity correction (4.5) are presented in the Appendix A. We can follow HM19 steps and analyze results of the velocity ratio (Z_v) as a function of the number of galaxies. Figure 4.4 shows individual velocity ratios $Z_v = \frac{v_{esc}}{v_{los,esc}}$ of all 38 galaxy clusters provided by our data sample measured at $0.5R_{200}$ by using the best-fit cosmology for calculating v_{esc}, which was subsequently adjusted due to the velocity correction (see the subsection 4.5.3.2). Overall, we can see good agreement with the theoretically predicted by HM19 Z_v (black line and shaded region on Figure 4.4).

The second way to compare our results with the HM19 predictions is to split our data into 4 bins by number of galaxies. We calculate the velocity ratio Z_v for the best-fit cosmology obtained by analyzing 36 clusters (4.21, 4.22). Overall, we see correlation with the HM19 results, as for the higher number of galaxies the velocity ratio moves closer to being equal to one (figure 4.5).

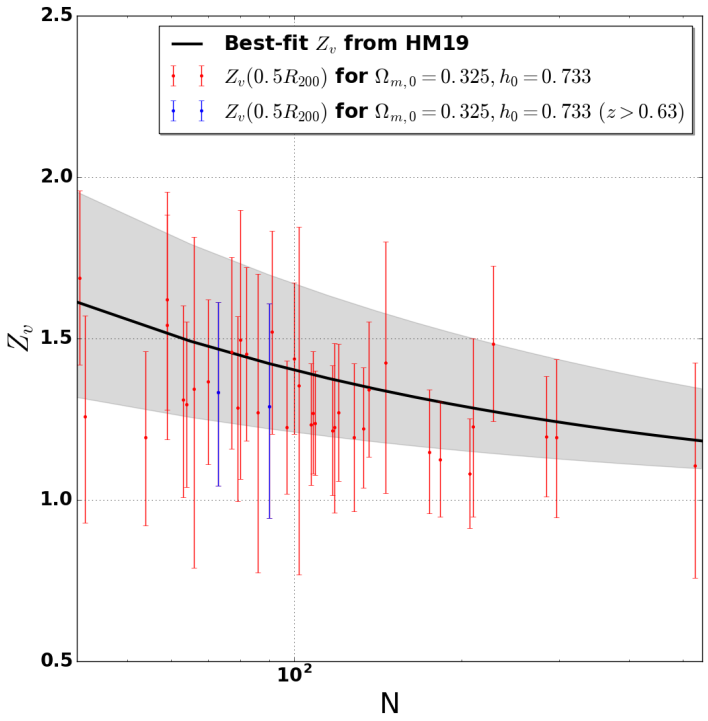

Figure 4.4: Z_v (measured at $0.5R_{200}$) vs. richness (i.e. number of galaxies in the range $0.3 \leq r/R_{200} \leq 1$). Black solid lines and corresponding shaded region are the best-fit model (4.7) from HM19. Individual error bars correspond to individual clusters from our data sample and they represent the measured Z_v at $0.5R_{200}$ vs. richness, where to calculate Z_v of individual clusters the best-fit cosmology (4.21, 4.22) of fitting 36 clusters was used. Two blue error bars correspond to the two high redshift clusters. Error budget comes from the velocity correction (4.4) and uncertainties of M_{200}.

4.5.8 Discussion and conclusions

Galaxy clusters have a lot of unrealized potential as a tool to probe cosmological and gravitational models. In principle, we can measure potentials by analyzing phase-spaces of individual clusters as the galaxies with the highest velocities provide tool of observing gravitational potentials directly through a simple expression: $v_{esc}(r) = \sqrt{-2\Phi(r)}$, where gravitational potential $\Phi(r)$ is generally a cosmology dependent function (see the expression 1.48). Unfortunately, we are able to observe clusters only from one position, which provides us only with a limited information about

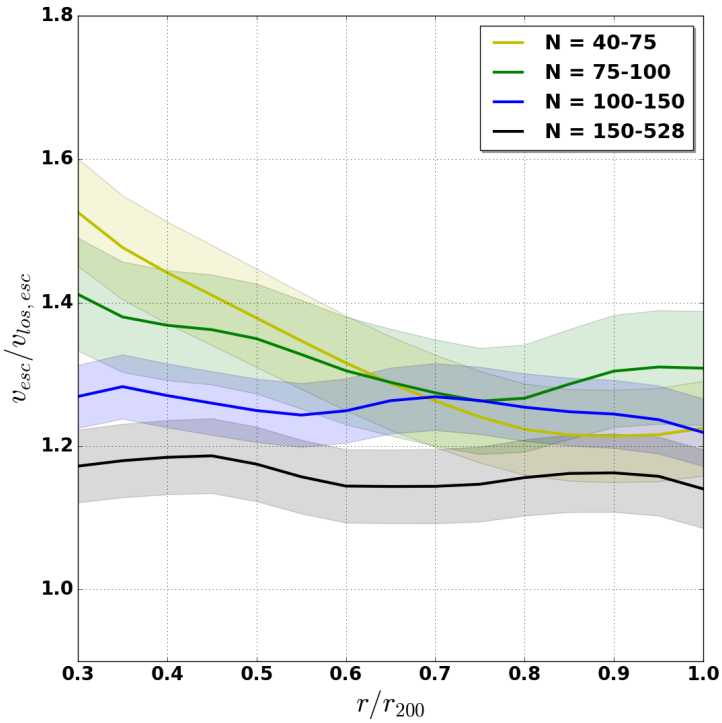

Figure 4.5: Velocity ratio as a function of the number of galaxies. Best-fit cosmology (4.21, 4.22) of fitting 36 clusters is utilized to calculate v_{esc} and later adjusted to account for the velocity correction due to the NFW density overestimation (see the subsection 4.5.3.2). $v_{los,esc}$ are directly measured by utilizing removal prescription proposed by *Gifford et al.* (2013). The galaxy clusters are split by the richness N as described in the legend. Solid lines and shaded regions correspond to the median and 67% scatter calculated from individual velocity ratios.

the phase-spaces, which effectively leads to a suppression of the true 3-dimensional escape velocity profile. However, the magnitude of this suppression is mass and cosmology independent (HM19), which provides us with all the needed information to connect maximum observed velocity profile ($v_{los,esc}$) with gravitational potential profile through v_{esc}. The suppression derived by HM19 is indeed nicely predicts v_{esc} on a cluster-by-cluster basis (compare red lines and shaded regions with blue error bars on the phase-spaces of individual clusters in Appendix A). In should be noted, that this is done only by using the inferred from the projected phases-space $v_{los,esc}$

and the richness (the number of galaxies in the radial range $0.3 \leq r/r_{200} \leq 1$).

Miller et al. (2016) and *Stark et al.* (2016a) discussed this approach of probing cosmology and in the second of these works, the Fisher matrix formalism was used to predict the constraining power on cosmological parameters by utilizing the escape velocity profiles as a cosmology probe in different cosmological scenarios. The authors came to the conclusion that constraints can be improved by reducing errors in the weak lensing mass and in the anisotropy parameter (which is the suppression function in our case) as well as by increasing the number of the galaxy clusters analyzed (N_{cl}). The authors looked at two cases with $N_{cl} = 100$ (1000) and came to the conclusion that the uncertainties on the matter energy-density and the EOS can be as low as $\sigma_{\Omega_{m,0}} = 0.007(0.025)$ and $\sigma_{\omega} = 0.138(0.431)$ after marginalizing over h_0. Due to our sample having only 38 galaxy clusters and because we had to utilize extra statistical uncertainty due to the velocity correction (see the subsection 4.5.3.2), we were able to place sensible constraints only on a set of two cosmological parameters $(\Omega_{m,0}, h_0)$, while fixing the EOS $\omega = -1$.

Currently, there is a very significant tension ($> 4.4\sigma$) between observations of the Hubble constant by analyzing Cepheids (*Riess et al.*, 2019) and from CMB observations (*Planck Collaboration et al.*, 2018). Our approach could be a necessary brick in the construction of the building of the understanding the discrepancy between CMB and Cepheids results of measuring Hubble constant. Our best-fit results (4.21, 4.22) favor the matter energy-density inferred from Plank CMB, while agreeing with the Hubble constant measured by Cepheids. This result places question mark on the models of decaying dark matter (*Berezhiani et al.*, 2015), which are one of the ways of easing tension in the Hubble constant observations.

While this section provides a preliminary results as well as an introduction to the novel approach of testing cosmology and gravity using phase-spaces of galaxy clusters, there is a room for improvements. First, we need the galaxy clusters with

higher number of galaxies per cluster, which would allow us to measure $v_{los,esc}$ from a projected phase-space more accurately, while also decreasing uncertainty produced by the suppression (4.7). Secondly, we can use direct shear measurements of the weak lensing data as in this work we utilized modeled matter density distributions. Additionally, this would allow us to utilize the Einasto model 1.38, which does not overestimate v_{esc} and it would allow us to drop the need to utilize the velocity correction (4.5), which is currently required due to the overestimation of the escape velocity by the NFW model (1.36). Moreover, the weak lensing data can be combined with the strong lensing data to increase precision of the weak lensing data (*Umetsu*, 2013).

4.6 Future Work

The precision of the analysis presented in this work will greatly improve with better data samples of the weak lensing and the measurements of positions and redshifts of the higher number of galaxies in the higher number of the galaxy clusters. However, even with the current level of the data significant future progress can be made. First, Emergent Gravity model theory should be improved to solve many assumptions it currently employs. The approach developed in the chapter III can be utilized to probe EG as well as other modified theories of gravity (see section 1.4) as it is able to predict the observed maximum velocity profiles with $\sim 2\%$ accuracy. The approach provides us with a controlled environment to simulate galaxy clusters with a given requirements in the framework of any gravity and cosmology model. The natural step is to use the approach to predict the suppression function for a given richness and projected dispersion in application to the models such as EG and f(R) with subsequent utilization of derived suppression on the real galaxy clusters data in a similar fashion as we tested standard ΛCDM cosmological model. Moreover, our results show that knowing richness and dispersion profile in addition to the matter density distribution allow us to provide high accuracy ($\sim 2\%$) mass estimate of the

galaxy clusters using the approach developed in the chapter III, which means that by using phase-spaces the approach is capable of estimating masses of galaxy clusters with high precision. The level of accuracy of constraining cosmological parameters presented in the chapter 4.5 can be greatly improved with current data by using direct shear measurements of the weak lensing data, which provide cosmology independent mass distribution profile. Moreover, it can be modelled using Einasto profile, which in turn does not require introduction of any velocity correction function used in the chapter 4.5. Finally, the current approach can be combined with the existing probes to provide even higher precision in constraining cosmological parameters and alternative theories of gravity.

APPENDIX

APPENDIX A

Individual phase-spaces

Projected phase-spaces of individual galaxy clusters. Black solid lines are the measured (by applying removal prescription proposed by *Gifford et al.* (2013) on the galaxies on the projected phase-spaces) maximum velocity profiles $v_{los,esc}$. Red lines and red shaded regions around them are v_{esc} with the best-fit cosmology (4.21, 4.22) and uncertainty around it due to the uncertainty of the weak lensing masses. Blue error bars correspond to the 8 radial bins of the adjusted measured maximum velocity profile due to the suppression function (4.7) and the velocity correction (4.5), i.e. $v_{los,esc} \times Z_v/(1-v_{corr})$. Binning is done in the range $[0.3; 1] \times R_{200}$ with the $0.1R_{200}$ steps.

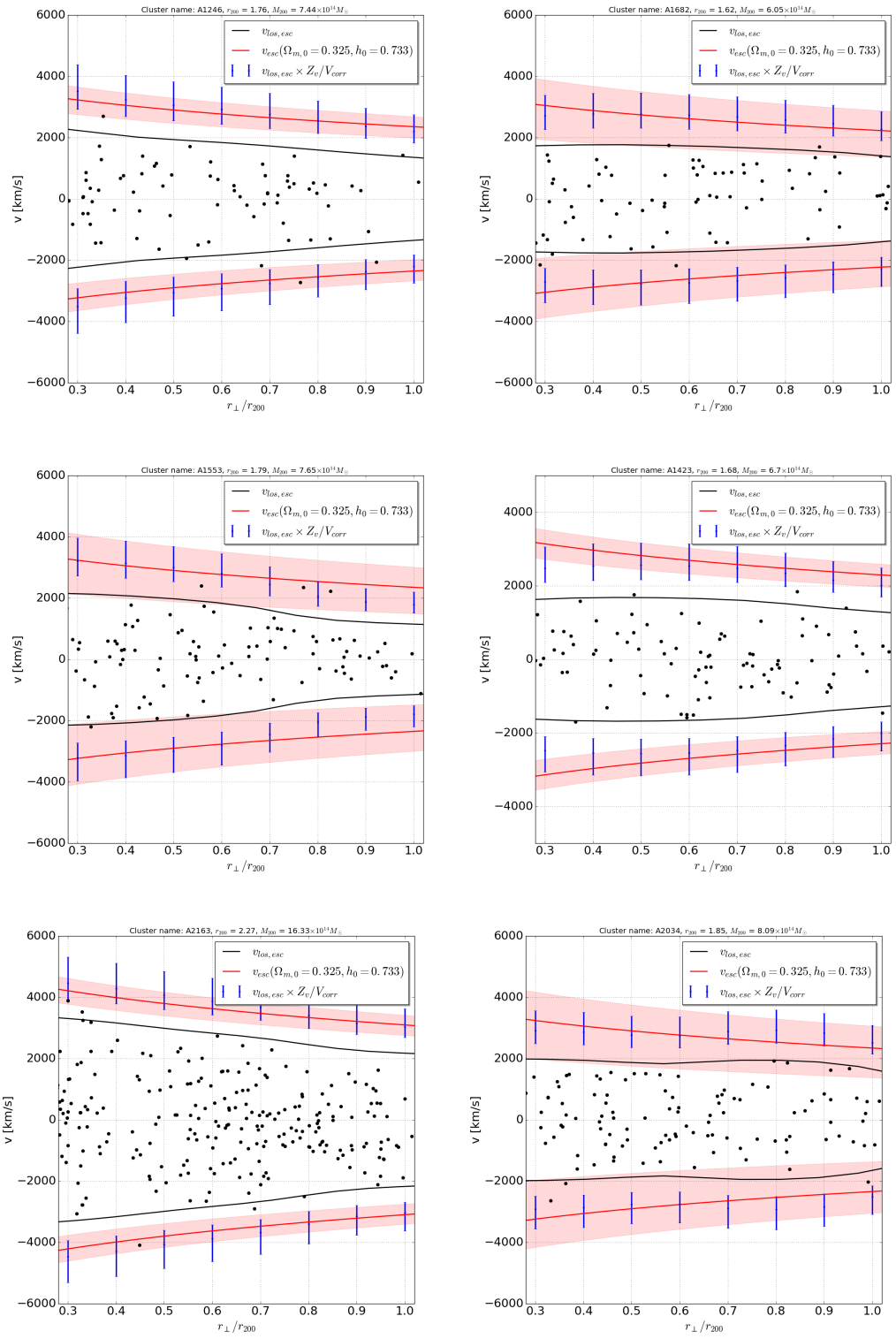

Figure A.1: Projected phase-spaces of individual galaxy clusters. The meaning of individual lines and error bars is described in the text of Appendix A.

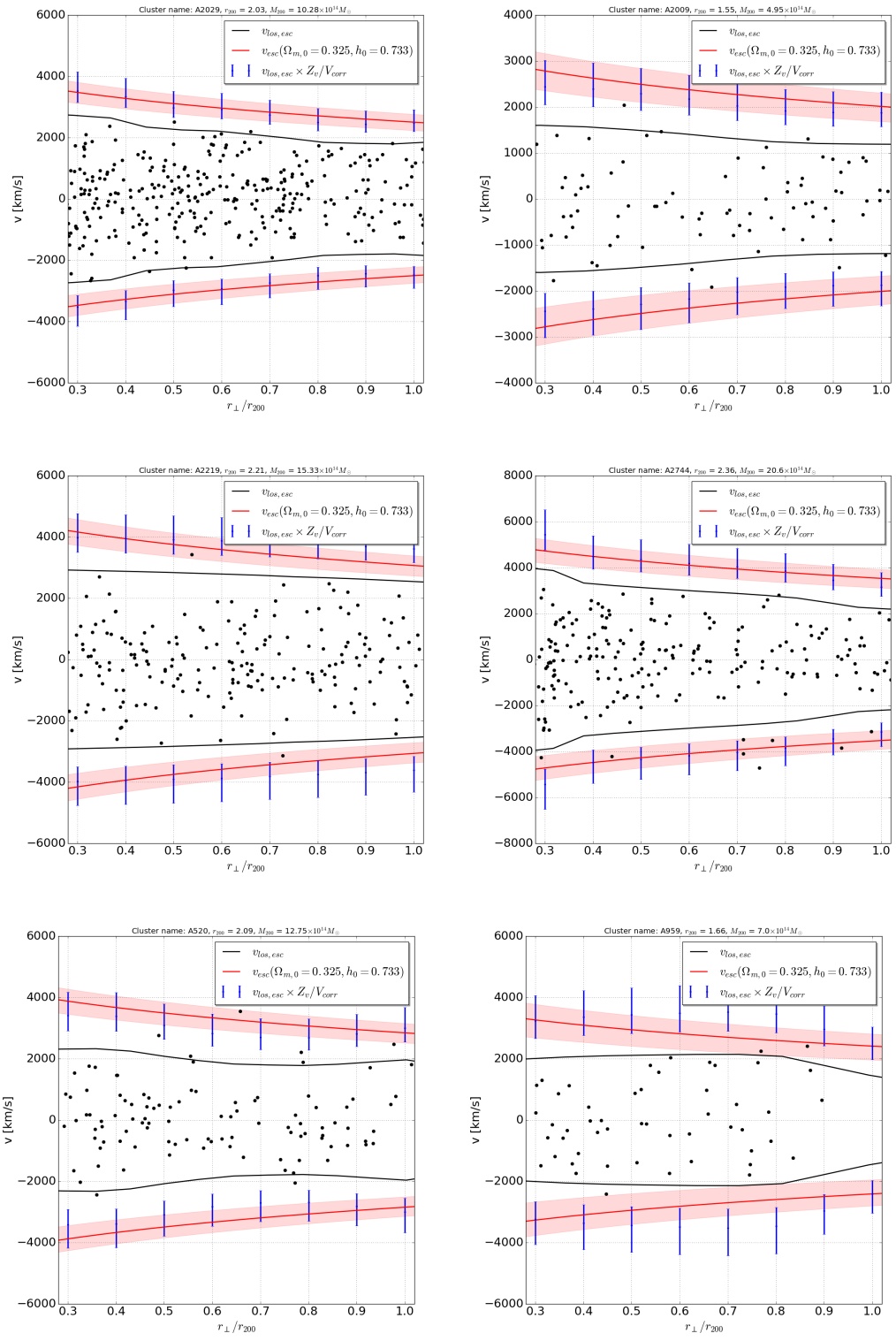

Figure A.2: Projected phase-spaces of individual galaxy clusters. The meaning of individual lines and error bars is described in the text of Appendix A.

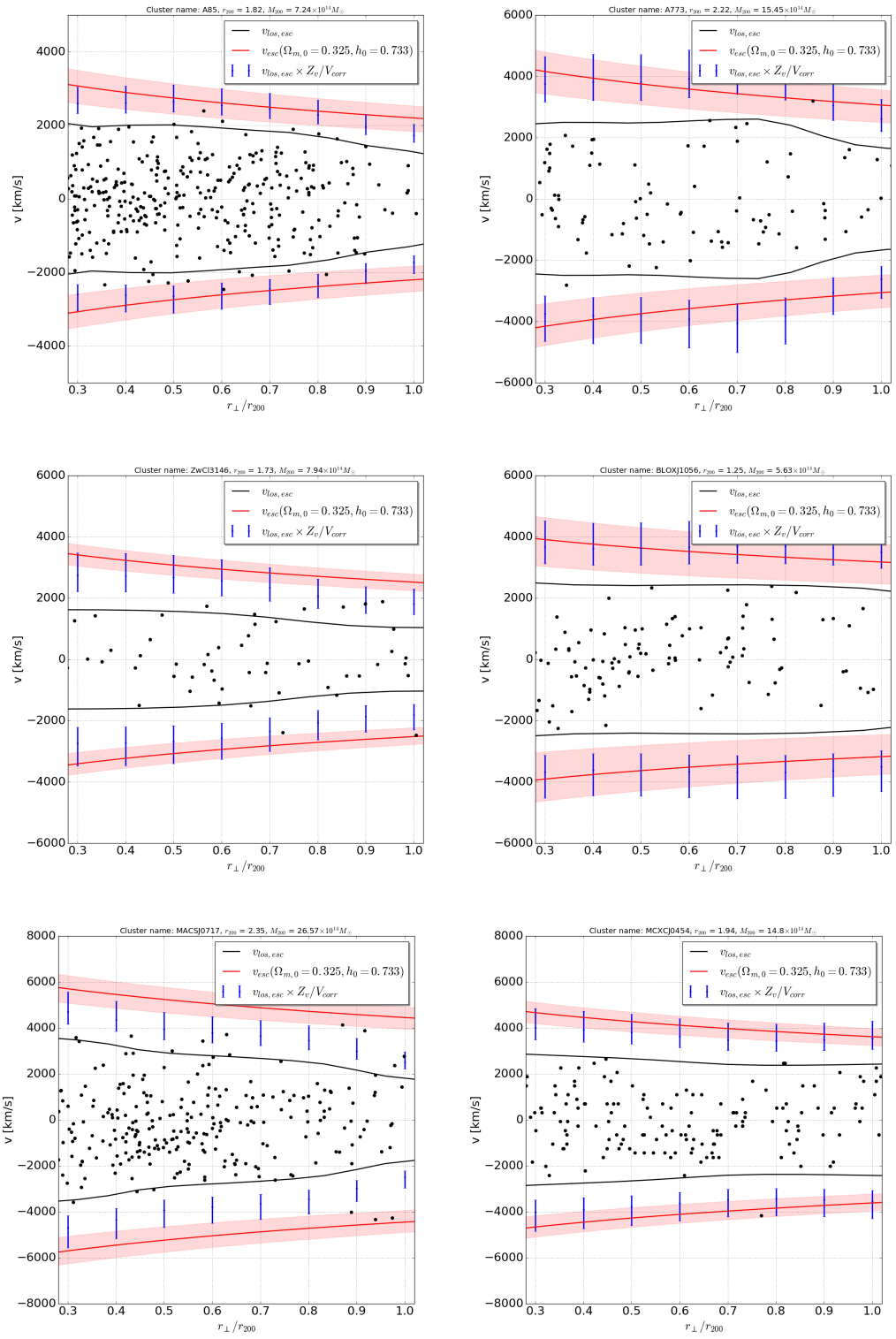

Figure A.3: Projected phase-spaces of individual galaxy clusters. The meaning of individual lines and error bars is described in the text of Appendix A.

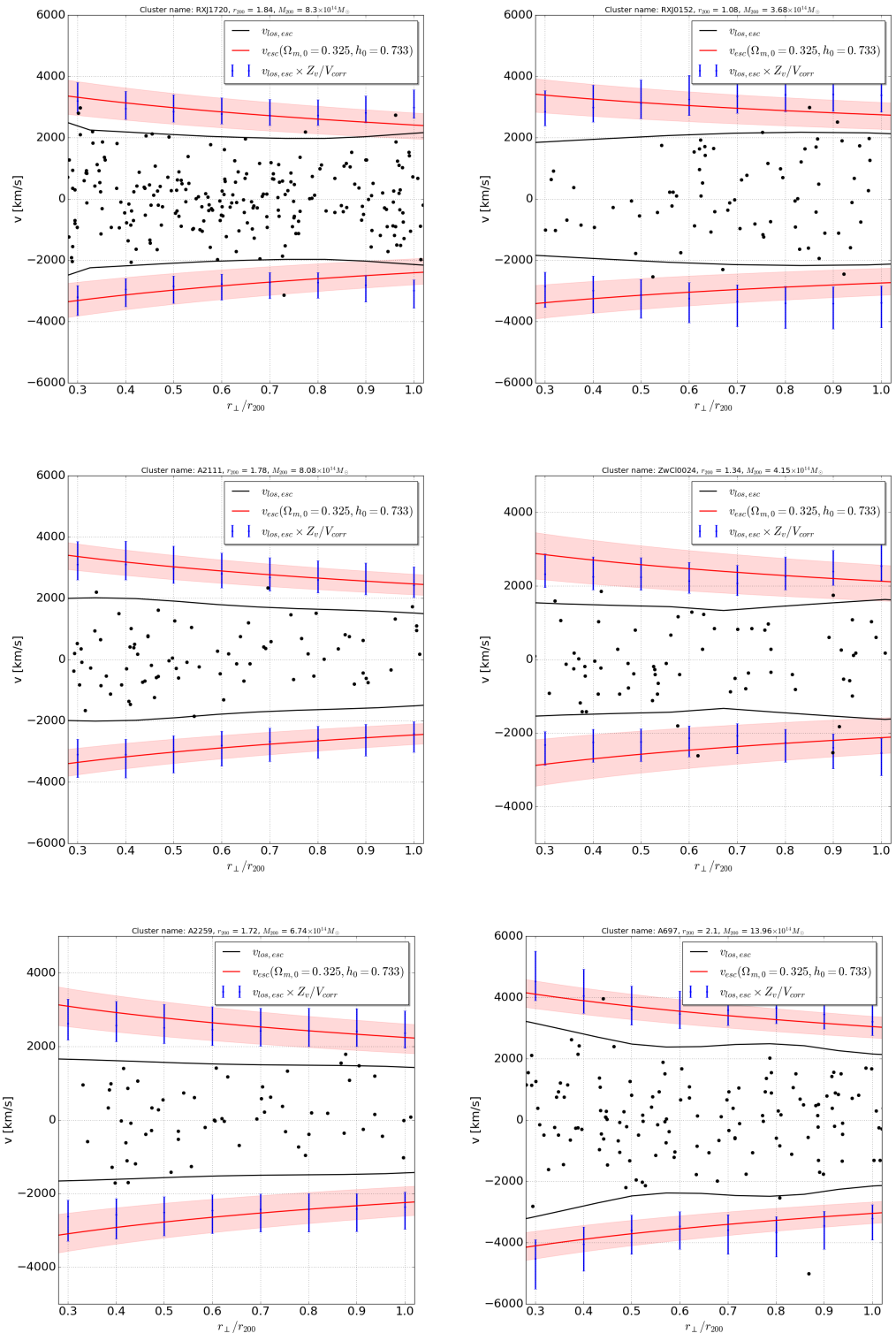

Figure A.4: Projected phase-spaces of individual galaxy clusters. The meaning of individual lines and error bars is described in the text of Appendix A.

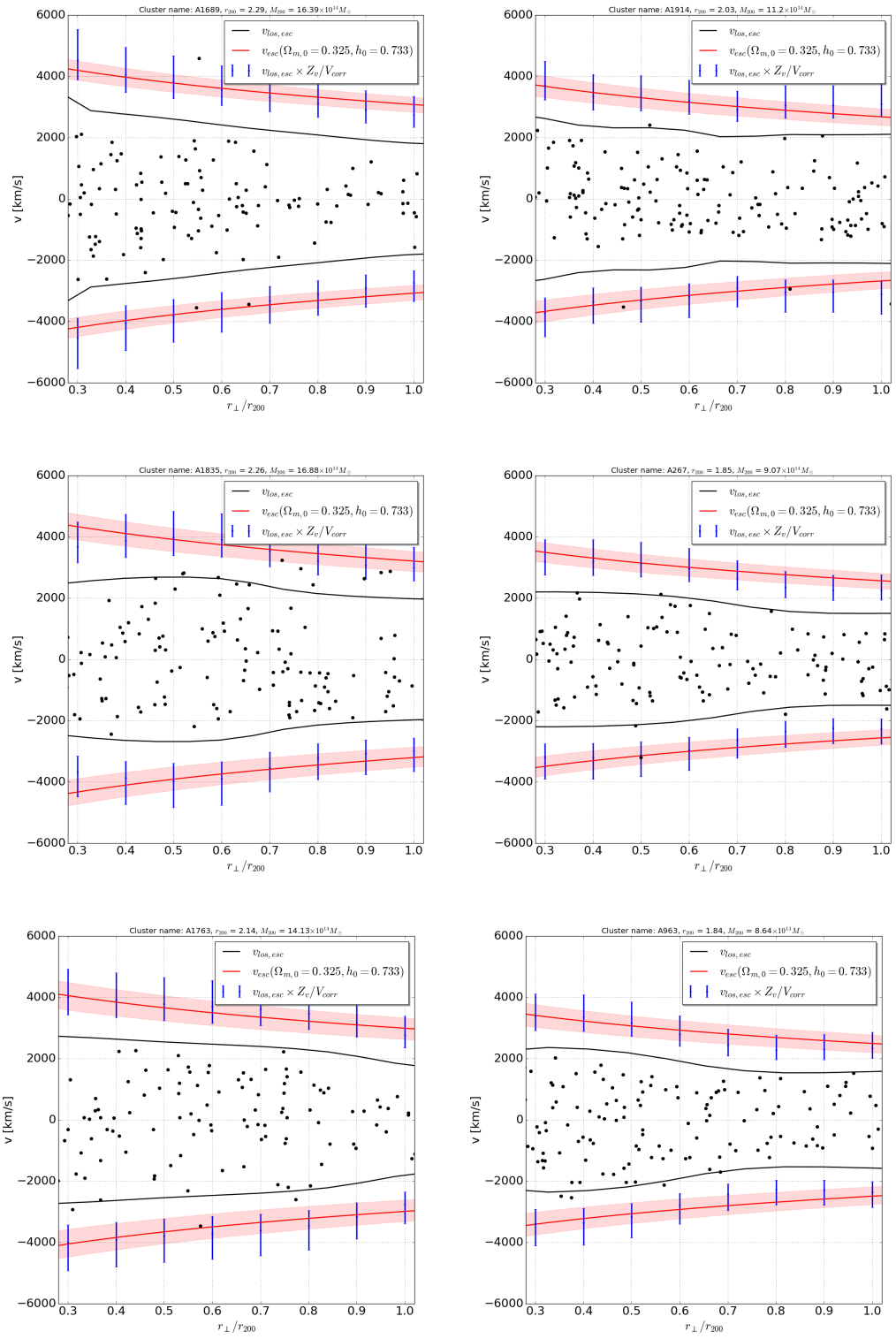

Figure A.5: Projected phase-spaces of individual galaxy clusters. The meaning of individual lines and error bars is described in the text of Appendix A.

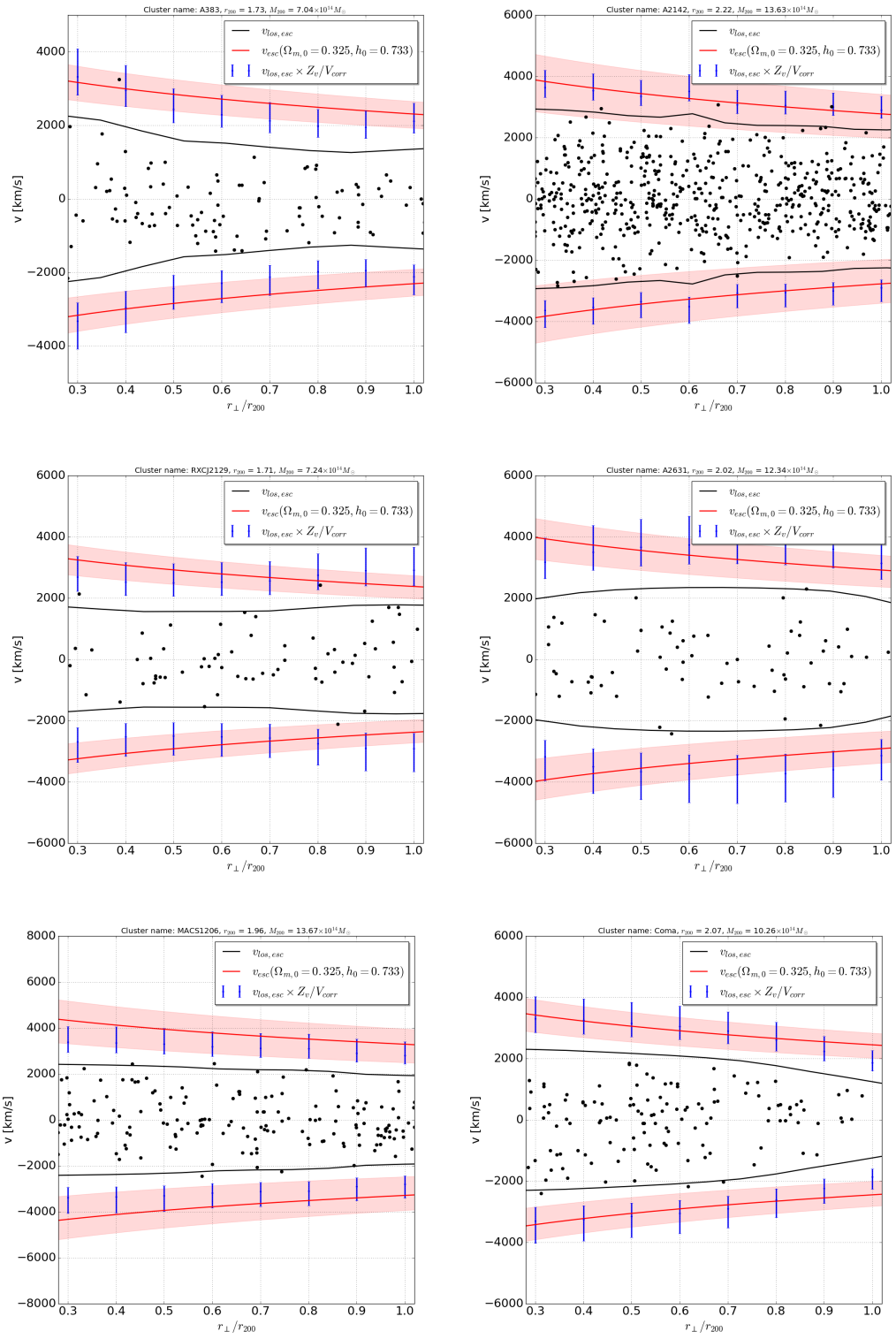

Figure A.6: Projected phase-spaces of individual galaxy clusters. The meaning of individual lines and error bars is described in the text of Appendix A.

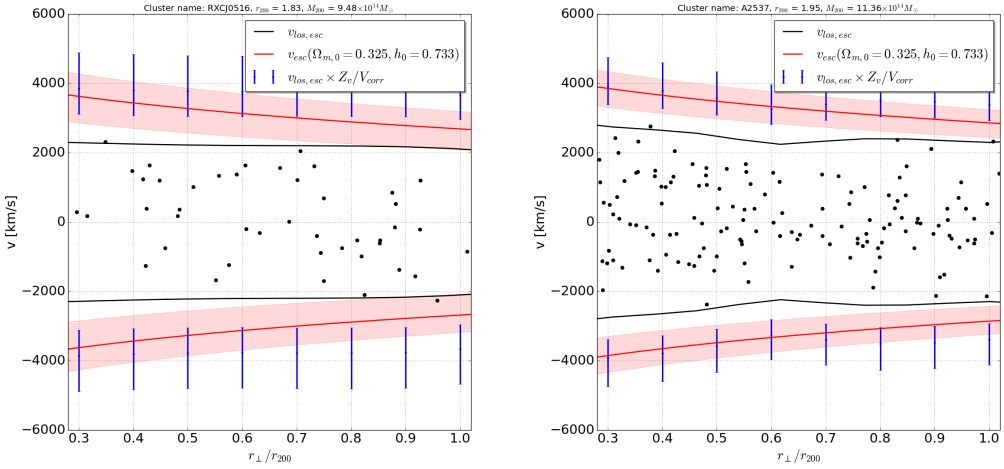

Figure A.7: Projected phase-spaces of individual galaxy clusters. The meaning of individual lines and error bars is described in the text of Appendix A.

BIBLIOGRAPHY

BIBLIOGRAPHY

Ade, P. A. R., et al. (2016), Planck 2015 results. XIII. Cosmological parameters, *Astron. Astrophys.*, *594*, A13, doi:10.1051/0004-6361/201525830.

Aguilar, L. A. (2008), *Dynamics of Galaxies and Clusters of Galaxies*, pp. 71–118, Springer Netherlands, Dordrecht, doi:10.1007/978-1-4020-6941-3_3.

Agulli, I., J. A. L. Aguerri, R. Sánchez-Janssen, C. Dalla Vecchia, A. Diaferio, R. Barrena, L. Dominguez Palmero, and H. Yu (2016), Deep spectroscopy of nearby galaxy clusters - I. Spectroscopic luminosity function of Abell 85, *MNRAS*, *458*, 1590–1603, doi:10.1093/mnras/stw422.

Amanullah, R., et al. (2010), Spectra and Hubble Space Telescope Light Curves of Six Type Ia Supernovae at 0.511 < z < 1.12 and the Union2 Compilation, *ApJ*, *716*(1), 712–738, doi:10.1088/0004-637X/716/1/712.

Andreon, S. (2010), The stellar mass fraction and baryon content of galaxy clusters and groups, *MNRAS*, *407*, 263–276, doi:10.1111/j.1365-2966.2010.16856.x.

Applegate, D. E., et al. (2014), Weighing the Giants - III. Methods and measurements of accurate galaxy cluster weak-lensing masses, *MNRAS*, *439*, 48–72, doi:10.1093/mnras/stt2129.

Behroozi, P. S., A. Loeb, and R. H. Wechsler (2013a), Unbound Particles in Dark Matter Halos, *JCAP*, *1306*, 019, doi:10.1088/1475-7516/2013/06/019.

Behroozi, P. S., A. Loeb, and R. H. Wechsler (2013b), Unbound Particles in Dark Matter Halos, *JCAP*, *1306*, 019, doi:10.1088/1475-7516/2013/06/019.

Berezhiani, Z., A. D. Dolgov, and I. I. Tkachev (2015), Reconciling Planck results with low redshift astronomical measurements, *Phys. Rev.*, *D92*(6), 061,303, doi:10.1103/PhysRevD.92.061303.

Betoule, M., et al. (2014a), Improved cosmological constraints from a joint analysis of the SDSS-II and SNLS supernova samples, *A&A*, *568*, A22, doi:10.1051/0004-6361/201423413.

Betoule, M., et al. (2014b), Improved cosmological constraints from a joint analysis of the SDSS-II and SNLS supernova samples, *A&A*, *568*, A22, doi:10.1051/0004-6361/201423413.

Blanton, M. R., et al. (2017), Sloan Digital Sky Survey IV: Mapping the Milky Way, Nearby Galaxies, and the Distant Universe, *AJ*, *154*(1), 28, doi:10.3847/1538-3881/aa7567.

Boschin, W., R. Barrena, and M. Girardi (2009), Internal dynamics of the galaxy cluster Abell 959, *A&A*, *495*(1), 15–26, doi:10.1051/0004-6361:200811043.

Broadhurst, T. J., M. Takada, K. Umetsu, X. Kong, N. Arimoto, M. Chiba, and T. Futamase (2005), The Surprisingly steep mass profile of Abell 1689, from a lensing analysis of Subaru images, *Astrophys. J.*, *619*, L143, doi:10.1086/428122.

Brouwer, M. M., et al. (2017), First test of Verlinde's theory of Emergent Gravity using Weak Gravitational Lensing measurements, *Mon. Not. Roy. Astron. Soc.*, *466*(3), 2547–2559, doi:10.1093/mnras/stw3192.

Calder, L., and O. Lahav (2008), Dark energy: back to Newton?, *Astronomy and Geophysics*, *49*(1), 1.13–1.18, doi:10.1111/j.1468-4004.2008.49113.x.

Carroll, S. M. (2001), The Cosmological constant, *Living Rev. Rel.*, *4*, 1, doi:10.12942/lrr-2001-1.

Cavaliere, A., and R. Fusco-Femiano (1978), The Distribution of Hot Gas in Clusters of Galaxies, *A&A*, *70*, 677.

Chung, D. J. H., and K. Freese (2000), Can geodesics in extra dimensions solve the cosmological horizon problem?, *Phys. Rev.*, *D62*, 063,513, doi:10.1103/PhysRevD.62.063513.

Clifton, T., P. G. Ferreira, A. Padilla, and C. Skordis (2012), Modified Gravity and Cosmology, *Phys. Rept.*, *513*, 1–189, doi:10.1016/j.physrep.2012.01.001.

Clowe, D., G. A. Luppino, N. Kaiser, and I. M. Gioia (2000), Weak Lensing by High-Redshift Clusters of Galaxies. I. Cluster Mass Reconstruction, *ApJ*, *539*, 540–560, doi:10.1086/309242.

Clowe, D., M. Bradac, A. H. Gonzalez, M. Markevitch, S. W. Randall, C. Jones, and D. Zaritsky (2006), A direct empirical proof of the existence of dark matter, *Astrophys. J.*, *648*, L109–L113, doi:10.1086/508162.

Cooray, A., W. Hu, D. Huterer, and M. Joffre (2001), Measuring angular diameter distances through halo clustering, *Astrophys. J.*, *557*, L7, doi:10.1086/323323.

Copeland, E. J., M. Sami, and S. Tsujikawa (2006), Dynamics of dark energy, *Int. J. Mod. Phys.*, *D15*, 1753–1936, doi:10.1142/S021827180600942X.

Correa, C. A., J. S. B. Wyithe, J. Schaye, and A. R. Duffy (2015), The accretion history of dark matter haloes III. A physical model for the concentrationmass relation, *Mon. Not. Roy. Astron. Soc.*, *452*(2), 1217–1232, doi:10.1093/mnras/stv1363.

Cypriano, E. S., L. Sodré, Jr., J.-P. Kneib, and L. E. Campusano (2004), Weak-Lensing Mass Distributions for 24 X-Ray Abell Clusters, *ApJ*, *613*, 95–108, doi:10.1086/422896.

Dahle, H. (2006), The Cluster Mass Function from Weak Gravitational Lensing, *Astrophys. J.*, *653*, 954–962, doi:10.1086/508654.

Dahle, H., N. Kaiser, R. J. Irgens, P. B. Lilje, and S. J. Maddox (2002), Weak Gravitational Lensing by a Sample of X-Ray Luminous Clusters of Galaxies. I. The Data Set, *ApJS*, *139*, 313–368, doi:10.1086/338678.

Dehnen, W. (1993), A Family of Potential-Density Pairs for Spherical Galaxies and Bulges, *Mon. Not. Roy. Astron. Soc.*, *265*, 250.

Demarco, R., et al. (2010), Star Formation Histories in a Cluster Environment at z ˜ 0.84, *ApJ*, *725*, 1252–1276, doi:10.1088/0004-637X/725/1/1252.

Diaferio, A. (1999), Mass estimation in the outer regions of galaxy clusters, *Mon. Not. Roy. Astron. Soc.*, *309*, 610, doi:10.1046/j.1365-8711.1999.02864.x.

Diaferio, A., and M. J. Geller (1997), Infall regions of galaxy clusters, *Astrophys. J.*, *481*, 633–643, doi:10.1086/304075.

Diemer, B., and A. V. Kravtsov (2015), A Universal Model for Halo Concentrations, *ApJ*, *799*(1), 108, doi:10.1088/0004-637X/799/1/108.

Diemer, B., and A. V. Kravtsov (2015), A universal model for halo concentrations, *Astrophys. J.*, *799*(1), 108, doi:10.1088/0004-637X/799/1/108.

Dolgov, A., V. Halenka, and I. Tkachev (2014), Power-law cosmology, SN Ia, and BAO, *JCAP*, *1410*(10), 047, doi:10.1088/1475-7516/2014/10/047.

Duffy, A. R., J. Schaye, S. T. Kay, and C. Dalla Vecchia (2008), Dark matter halo concentrations in the Wilkinson Microwave Anisotropy Probe year 5 cosmology, *MNRAS*, *390*, L64–L68, doi:10.1111/j.1745-3933.2008.00537.x.

Dvali, G. R., G. Gabadadze, and M. Porrati (2000), 4-D gravity on a brane in 5-D Minkowski space, *Phys. Lett.*, *B485*, 208–214, doi:10.1016/S0370-2693(00)00669-9.

Eckert, D., et al. (2012), The gas distribution in the outer regions of galaxy clusters, *A&A*, *541*, A57, doi:10.1051/0004-6361/201118281.

Eddington, A. S. (1916), The kinetic energy of a star-clusters, *MNRAS*, *76*, 525–528, doi:10.1093/mnras/76.6.525.

Edwards, L. O. V., and D. Fadda (2011), A Multi-wavelength Analysis of Spitzer Selected Coma Cluster Galaxies: Star Formation Rates and Masses, *AJ*, *142*, 148, doi:10.1088/0004-6256/142/5/148.

Einasto, J. (1965), , *Trudy Astrofizicheskogo Instituta Alma-Ata*, *5*, 87–100.

Enqvist, K. (2008), Lemaitre-Tolman-Bondi model and accelerating expansion, *Gen. Rel. Grav.*, *40*, 451–466, doi:10.1007/s10714-007-0553-9.

Ettori, S., and I. Balestra (2009), The outer regions of galaxy clusters: Chandra constraints on the X-ray surface brightness, *A&A*, *496*, 343–349, doi:10.1051/0004-6361:200811177.

Ettori, S., et al. (2019), Hydrostatic mass profiles in X-COP galaxy clusters, *Astron. Astrophys.*, *621*, A39, doi:10.1051/0004-6361/201833323.

Evrard, A. E., et al. (2008), Virial Scaling of Massive Dark Matter Halos: Why Clusters Prefer a High Normalization Cosmology, *ApJ*, *672*(1), 122–137, doi:10.1086/521616.

Famaey, B., and S. McGaugh (2012), Modified Newtonian Dynamics (MOND): Observational Phenomenology and Relativistic Extensions, *Living Rev. Rel.*, *15*, 10, doi:10.12942/lrr-2012-10.

Foëx, G., G. Soucail, E. Pointecouteau, M. Arnaud, M. Limousin, and G. W. Pratt (2012), The dark matter distribution in z ˜ 0.5 clusters of galaxies. I. Determining scaling relations with weak lensing masses, *A&A*, *546*, A106, doi:10.1051/0004-6361/201218973.

Foëx, G., H. Böhringer, and G. Chon (2017), Comparison of hydrostatic and dynamical masses of distant X-ray luminous galaxy clusters, *A&A*, *606*, A122, doi:10.1051/0004-6361/201731104.

Freese, K. (2017), Status of dark matter in the universe, *International Journal of Modern Physics D*, *26*(6), 1730012-223, doi:10.1142/S0218271817300129.

Freese, K., and M. Lewis (2002), Cardassian expansion: A Model in which the universe is flat, matter dominated, and accelerating, *Phys. Lett.*, *B540*, 1–8, doi:10.1016/S0370-2693(02)02122-6.

Frieman, J., M. Turner, and D. Huterer (2008), Dark Energy and the Accelerating Universe, *Ann. Rev. Astron. Astrophys.*, *46*, 385–432, doi:10.1146/annurev.astro.46.060407.145243.

Geller, M. J., A. Diaferio, K. J. Rines, and A. L. Serra (2013), Measuring the Mass Distribution in Galaxy Clusters, *ApJ*, *764*, 58, doi:10.1088/0004-637X/764/1/58.

Giacintucci, S., M. Markevitch, R. Cassano, T. Venturi, T. E. Clarke, and G. Brunetti (2017), Occurrence of radio minihalos in a mass-limited sample of galaxy clusters, *Astrophys. J.*, *841*(2), 71, doi:10.3847/1538-4357/aa7069.

Gifford, D., and C. J. Miller (2013), Velocity Anisotropy and Shape Bias in the Caustic Technique, *ApJ*, *768*(2), L32, doi:10.1088/2041-8205/768/2/L32.

Gifford, D., C. J. Miller, and N. Kern (2013), A Systematic Analysis of Caustic Methods for Galaxy Cluster Masses, *Astrophys. J.*, *773*, 116, doi:10.1088/0004-637X/773/2/116.

Giles, P. A., B. J. Maughan, H. Dahle, M. Bonamente, D. Landry, C. Jones, M. Joy, S. S. Murray, and N. van der Pyl (2017), Chandra measurements of a complete sample of X-ray luminous galaxy clusters: the luminositymass relation, *Mon. Not. Roy. Astron. Soc.*, *465*(1), 858–884, doi:10.1093/mnras/stw2621.

Giodini, S., et al. (2009), Stellar and Total Baryon Mass Fractions in Groups and Clusters Since Redshift 1, *ApJ*, *703*, 982–993, doi:10.1088/0004-637X/703/1/982.

Girardi, M., R. Barrena, W. Boschin, and E. Ellingson (2008), Cluster Abell 520: a perspective based on member galaxies. A cluster forming at the crossing of three filaments?, *A&A*, *491*, 379–395, doi:10.1051/0004-6361:200810549.

Girardi, M., et al. (2015), CLASH-VLT: Substructure in the galaxy cluster MACS J1206.2-0847 from kinematics of galaxy populations, *A&A*, *579*, A4, doi:10.1051/0004-6361/201425599.

Groener, A. M., D. M. Goldberg, and M. Sereno (2016), The galaxy cluster concentrationmass scaling relation, *Mon. Not. Roy. Astron. Soc.*, *455*(1), 892–919, doi:10.1093/mnras/stv2341.

Guo, Q., S. White, M. Boylan-Kolchin, G. De Lucia, G. Kauffmann, G. Lemson, C. Li, V. Springel, and S. Weinmann (2011), From dwarf spheroidals to cD galaxies: simulating the galaxy population in a ΛCDM cosmology, *MNRAS*, *413*, 101–131, doi:10.1111/j.1365-2966.2010.18114.x.

Halenka, V., and C. J. Miller (2018), Testing Emergent Gravity with mass densities of galaxy clusters, *arXiv e-prints*, arXiv:1807.01689.

Hassan, S. F., and R. A. Rosen (2012a), Resolving the Ghost Problem in non-Linear Massive Gravity, *Phys. Rev. Lett.*, *108*, 041,101, doi:10.1103/PhysRevLett.108.041101.

Hassan, S. F., and R. A. Rosen (2012b), Bimetric Gravity from Ghost-free Massive Gravity, *JHEP*, *02*, 126, doi:10.1007/JHEP02(2012)126.

High, F. W., et al. (2012), Weak-lensing Mass Measurements of Five Galaxy Clusters in the South Pole Telescope Survey Using Magellan/Megacam, *ApJ*, *758*, 68, doi:10.1088/0004-637X/758/1/68.

Hinshaw, G., et al. (2013), Nine-year Wilkinson Microwave Anisotropy Probe (WMAP) Observations: Cosmological Parameter Results, *ApJS*, *208*(2), 19, doi:10.1088/0067-0049/208/2/19.

Hoekstra, H., R. Herbonnet, A. Muzzin, A. Babul, A. Mahdavi, M. Viola, and M. Cacciato (2015), The Canadian Cluster Comparison Project: detailed study of systematics and updated weak lensing masses, *MNRAS*, *449*, 685–714, doi:10.1093/mnras/stv275.

Hossenfelder, S. (2017), Covariant version of Verlindes emergent gravity, *Phys. Rev.*, *D95*(12), 124,018, doi:10.1103/PhysRevD.95.124018.

Huang, Z., M. Radovich, A. Grado, E. Puddu, A. Romano, L. Limatola, and L. Fu (2011), A weak-lensing analysis of the Abell 383 cluster, *A&A*, *529*, A93, doi:10.1051/0004-6361/201015955.

Hwang, H. S., M. J. Geller, A. Diaferio, K. J. Rines, and H. J. Zahid (2014), Comparing Dense Galaxy Cluster Redshift Surveys with Weak-lensing Maps, *ApJ*, *797*, 106, doi:10.1088/0004-637X/797/2/106.

Jacobson, T. (1995a), Thermodynamics of space-time: The Einstein equation of state, *Phys. Rev. Lett.*, *75*, 1260–1263, doi:10.1103/PhysRevLett.75.1260.

Jacobson, T. (1995b), Thermodynamics of space-time: The Einstein equation of state, *Phys. Rev. Lett.*, *75*, 1260–1263, doi:10.1103/PhysRevLett.75.1260.

Kapteyn, J. C. (1922), First Attempt at a Theory of the Arrangement and Motion of the Sidereal System, *ApJ*, *55*, 302, doi:10.1086/142670.

Khoury, J., and A. Weltman (2004), Chameleon fields: Awaiting surprises for tests of gravity in space, *Phys. Rev. Lett.*, *93*, 171,104, doi:10.1103/PhysRevLett.93.171104.

Klypin, A., G. Yepes, S. Gottlober, F. Prada, and S. Hess (2016), MultiDark simulations: the story of dark matter halo concentrations and density profiles, *Mon. Not. Roy. Astron. Soc.*, *457*(4), 4340–4359, doi:10.1093/mnras/stw248.

Laganá, T. F., N. Martinet, F. Durret, G. B. Lima Neto, B. Maughan, and Y.-Y. Zhang (2013), A comprehensive picture of baryons in groups and clusters of galaxies, *A&A*, *555*, A66, doi:10.1051/0004-6361/201220423.

Łokas, E. L., and G. A. Mamon (2001), Properties of spherical galaxies and clusters with an NFW density profile, *MNRAS*, *321*, 155–166, doi:10.1046/j.1365-8711.2001.04007.x.

Lovelock, D. (1971), The Einstein tensor and its generalizations, *J. Math. Phys.*, *12*, 498–501, doi:10.1063/1.1665613.

Lovelock, D. (1972), The Four-Dimensionality of Space and the Einstein Tensor, *Journal of Mathematical Physics*, *13*, 874–876, doi:10.1063/1.1666069.

Martin, J. (2012), Everything You Always Wanted To Know About The Cosmological Constant Problem (But Were Afraid To Ask), *Comptes Rendus Physique*, *13*, 566–665, doi:10.1016/j.crhy.2012.04.008.

Maurogordato, S., et al. (2008), A 2163: Merger events in the hottest Abell galaxy cluster. I. Dynamical analysis from optical data, *A&A*, *481*, 593–613, doi: 10.1051/0004-6361:20077614.

Medezinski, E., K. Umetsu, N. Okabe, M. Nonino, S. Molnar, R. Massey, R. Dupke, and J. Merten (2016), Frontier Fields: Subaru Weak-Lensing Analysis of the Merging Galaxy Cluster A2744, *ApJ*, *817*, 24, doi:10.3847/0004-637X/817/1/24.

Merritt, D., A. W. Graham, B. Moore, J. Diemand, and B. Terzić (2006), Empirical Models for Dark Matter Halos. I. Nonparametric Construction of Density Profiles and Comparison with Parametric Models, *AJ*, *132*, 2685–2700, doi:10.1086/508988.

Milgrom, M. (1983), A Modification of the Newtonian dynamics as a possible alternative to the hidden mass hypothesis, *Astrophys. J.*, *270*, 365–370, doi: 10.1086/161130.

Milgrom, M. (2008), The MOND paradigm, *arXiv e-prints*, arXiv:0801.3133.

Milgrom, M. (2009), Bimetric MOND gravity, *Phys. Rev.*, *D80*, 123,536, doi: 10.1103/PhysRevD.80.123536.

Miller, C. J., A. Stark, D. Gifford, and N. Kern (2016), Inferring Gravitational Potentials From Mass Densities in Cluster-sized Halos, *Astrophys. J.*, *822*(1), 41, doi:10.3847/0004-637X/822/1/41.

Moran, S. M., R. S. Ellis, T. Treu, G. P. Smith, R. M. Rich, and I. Smail (2007), A Wide-Field Survey of Two z ˜ 0.5 Galaxy Clusters: Identifying the Physical Processes Responsible for the Observed Transformation of Spirals into S0s, *ApJ*, *671*, 1503–1522, doi:10.1086/522303.

Nandra, R., A. N. Lasenby, and M. P. Hobson (2012), The effect of an expanding universe on massive objects, *MNRAS*, *422*(4), 2945–2959, doi:10.1111/j.1365-2966.2012.20617.x.

Natarajan, P., et al. (2017), Mapping substructure in the HST Frontier Fields cluster lenses and in cosmological simulations, *Mon. Not. Roy. Astron. Soc.*, *468*(2), 1962–1980, doi:10.1093/mnras/stw3385.

Navarro, J. F., C. S. Frenk, and S. D. M. White (1996), The Structure of cold dark matter halos, *Astrophys. J.*, *462*, 563–575, doi:10.1086/177173.

Navarro, J. F., C. S. Frenk, and S. D. M. White (1997), A Universal density profile from hierarchical clustering, *Astrophys. J.*, *490*, 493–508, doi:10.1086/304888.

Nieuwenhuizen, T. M. (2017), How Zwicky already ruled out modified gravity theories without dark matter, *Fortsch. Phys.*, *65*(6-8), 1600,050, doi: 10.1002/prop.201600050.

Okabe, N., and G. P. Smith (2015), LoCuSS: Weak-lensing mass calibration of galaxy clusters, *ArXiv e-prints*.

Okabe, N., and K. Umetsu (2008), Subaru Weak Lensing Study of Seven Merging Clusters: Distributions of Mass and Baryons, *PASJ*, *60*, 345–375, doi: 10.1093/pasj/60.2.345.

Okabe, N., M. Takada, K. Umetsu, T. Futamase, and G. P. Smith (2010), LoCuSS: Subaru Weak Lensing Study of 30 Galaxy Clusters, *PASJ*, *62*, 811–870, doi:10.1093/pasj/62.3.811.

Owers, M. S., S. W. Randall, P. E. J. Nulsen, W. J. Couch, L. P. David, and J. C. Kempner (2011), The Dissection of Abell 2744: A Rich Cluster Growing Through Major and Minor Mergers, *ApJ*, *728*, 27, doi:10.1088/0004-637X/728/1/27.

Pedersen, K., and H. Dahle (2007), Calibration of the Mass-Temperature Relation for Clusters of Galaxies Using Weak Gravitational Lensing, *ApJ*, *667*, 26–34, doi: 10.1086/520945.

Perlmutter, S., et al. (1999), Measurements of Omega and Lambda from 42 high redshift supernovae, *Astrophys. J.*, *517*, 565–586, doi:10.1086/307221.

Planck Collaboration, et al. (2013), Planck intermediate results. V. Pressure profiles of galaxy clusters from the Sunyaev-Zeldovich effect, *A&A*, *550*, A131, doi: 10.1051/0004-6361/201220040.

Planck Collaboration, et al. (2018), Planck 2018 results. VI. Cosmological parameters, *arXiv e-prints*, arXiv:1807.06209.

Radovich, M., E. Puddu, A. Romano, A. Grado, and F. Getman (2008), A weak lensing analysis of the Abell 2163 cluster, *Astron. Astrophys.*, *487*, 55, doi: 10.1051/0004-6361:200809731.

Rasia, E., G. Tormen, and L. Moscardini (2004), A dynamical model for the distribution of dark matter and gas in galaxy clusters, *MNRAS*, *351*(1), 237–252, doi:10.1111/j.1365-2966.2004.07775.x.

Retana-Montenegro, E., E. Van Hese, G. Gentile, M. Baes, and F. Frutos-Alfaro (2012), Analytical properties of Einasto dark matter haloes, *Astron. Astrophys.*, *540*, A70, doi:10.1051/0004-6361/201118543.

Riess, A. G., S. Casertano, W. Yuan, L. M. Macri, and D. Scolnic (2019), Large Magellanic Cloud Cepheid Standards Provide a 1% Foundation for the Determination of the Hubble Constant and Stronger Evidence for Physics beyond ΛCDM, *ApJ*, *876*(1), 85, doi:10.3847/1538-4357/ab1422.

Riess, A. G., et al. (1998), Observational evidence from supernovae for an accelerating universe and a cosmological constant, *Astron. J.*, *116*, 1009–1038, doi: 10.1086/300499.

Rines, K., M. J. Geller, A. Diaferio, and M. J. Kurtz (2013), Measuring the Ultimate Halo Mass of Galaxy Clusters: Redshifts and Mass Profiles from the Hectospec Cluster Survey (HeCS), *ApJ*, *767*, 15, doi:10.1088/0004-637X/767/1/15.

Rubin, V. C., and W. K. Ford, Jr. (1970), Rotation of the Andromeda Nebula from a Spectroscopic Survey of Emission Regions, *Astrophys. J.*, *159*, 379–403, doi:10.1086/150317.

Schellenberger, G., and T. H. Reiprich (2017), HICOSMO cosmology with a complete sample of galaxy clusters I. Data analysis, sample selection and luminositymass scaling relation, *Mon. Not. Roy. Astron. Soc.*, *469*(3), 3738–3761, doi:10.1093/mnras/stx1022.

Sereno, M. (2015), CoMaLit III. Literature catalogues of weak lensing clusters of galaxies (LC^2), *Mon. Not. Roy. Astron. Soc.*, *450*(4), 3665–3674, doi:10.1093/mnras/stu2505.

Sereno, M., and G. Covone (2013), The mass-concentration relation in massive galaxy clusters at redshift 1, *Mon. Not. Roy. Astron. Soc.*, *434*, 878, doi:10.1093/mnras/stt1086.

Sereno, M., S. Ettori, and A. Baldi (2012), Shape and orientation of the gas distribution in A1689, *Mon. Not. Roy. Astron. Soc.*, *419*, 2646, doi:10.1111/j.1365-2966.2011.19914.x.

Sereno, M., C. Fedeli, and L. Moscardini (2016), Comparison of weak lensing by NFW and Einasto halos and systematic errors, *JCAP*, *1601*(01), 042, doi:10.1088/1475-7516/2016/01/042.

Serra, A. L., A. Diaferio, G. Murante, and S. Borgani (2011), Measuring the escape velocity and mass profiles of galaxy clusters beyond their virial radius, *MNRAS*, *412*(2), 800–816, doi:10.1111/j.1365-2966.2010.17946.x.

Smail, I., R. S. Ellis, A. Dressler, W. J. Couch, A. Oemler, R. M. Sharples, and H. Butcher (1997), A Comparison of Direct and Indirect Mass Estimates for Distant Clusters of Galaxies, *ApJ*, *479*, 70–81, doi:10.1086/303844.

Springel, V., et al. (2005), Simulating the joint evolution of quasars, galaxies and their large-scale distribution, *Nature*, *435*, 629–636, doi:10.1038/nature03597.

Stark, A., C. J. Miller, and D. Gifford (2016a), On Escaping a Galaxy Cluster in an Accelerating Universe, *Astrophys. J.*, *830*, 109, doi:10.3847/0004-637X/830/2/109.

Stark, A., C. J. Miller, N. Kern, D. Gifford, G.-B. Zhao, B. Li, K. Koyama, and R. C. Nichol (2016b), Probing Theories of Gravity with Phase Space-Inferred Potentials of Galaxy Clusters, *Phys. Rev.*, *D93*(8), 084,036, doi:10.1103/PhysRevD.93.084036.

Stark, A., C. J. Miller, and D. Huterer (2017), Cosmology with galaxy cluster phase spaces, *Phys. Rev. D*, *96*(2), 023543, doi:10.1103/PhysRevD.96.023543.

Stark, A., C. J. Miller, and V. Halenka (2019), Deriving galaxy cluster velocity anisotropy profiles from a joint analysis of dynamical and weak lensing data, *Astrophys. J.*, *874*(1), 33, doi:10.3847/1538-4357/ab06fa.

Tortora, C., L. V. E. Koopmans, N. R. Napolitano, and E. A. Valentijn (2018), Testing Verlinde's emergent gravity in early-type galaxies, *Mon. Not. Roy. Astron. Soc.*, *473*(2), 2324–2334, doi:10.1093/mnras/stx2432.

Tran, K.-V. H., M. Franx, G. D. Illingworth, P. van Dokkum, D. D. Kelson, J. P. Blakeslee, and M. Postman (2007), A Keck Spectroscopic Survey of MS 1054-03 (z = 0.83): Forming the Red Sequence, *ApJ*, *661*(2), 750–767, doi:10.1086/513738.

Treu, T., et al. (2015), The Grism Lens-Amplified Survey from Space (GLASS). I. Survey Overview and First Data Release, *ApJ*, *812*, 114, doi:10.1088/0004-637X/812/2/114.

Tsujikawa, S. (2010), Modified gravity models of dark energy, *Lect. Notes Phys.*, *800*, 99–145, doi:10.1007/978-3-642-10598-2_3.

Tsujikawa, S. (2011), Dark Energy: Investigation and Modeling, in *Astrophysics and Space Science Library*, *Astrophysics and Space Science Library*, vol. 370, edited by S. Matarrese, M. Colpi, V. Gorini, and U. Moschella, p. 331, doi:10.1007/978-90-481-8685-3_8.

Tyler, K. D., G. H. Rieke, and L. Bai (2013), Star-forming Galaxy Evolution in Nearby Rich Clusters, *ApJ*, *773*, 86, doi:10.1088/0004-637X/773/2/86.

Umetsu, K. (2013), Model-Free Multi-Probe Lensing Reconstruction of Cluster Mass Profiles, *Astrophys. J.*, *769*, 13, doi:10.1088/0004-637X/769/1/13.

Umetsu, K., et al. (2015), Three-dimensional Multi-probe Analysis of the Galaxy Cluster A1689, *ApJ*, *806*, 207, doi:10.1088/0004-637X/806/2/207.

Vainshtein, A. I. (1972), To the problem of nonvanishing gravitation mass, *Phys. Lett.*, *39B*, 393–394, doi:10.1016/0370-2693(72)90147-5.

Verlinde, E. P. (2011), On the Origin of Gravity and the Laws of Newton, *JHEP*, *04*, 029, doi:10.1007/JHEP04(2011)029.

Verlinde, E. P. (2017), Emergent Gravity and the Dark Universe, *SciPost Phys.*, *2*(3), 016, doi:10.21468/SciPostPhys.2.3.016.

Vikhlinin, A., A. Kravtsov, W. Forman, C. Jones, M. Markevitch, S. S. Murray, and L. Van Speybroeck (2006), Chandra sample of nearby relaxed galaxy clusters: Mass, gas fraction, and mass-temperature relation, *Astrophys. J.*, *640*, 691–709, doi:10.1086/500288.

Yoo, J., and Y. Watanabe (2012), Theoretical Models of Dark Energy, *Int. J. Mod. Phys.*, *D21*, 1230,002, doi:10.1142/S0218271812300029.

ZuHone, J. A., and J. R. Sims (2019), Testing Emergent Gravity with Optical, X-ray, and Weak Lensing Measurements in Massive, Relaxed Galaxy Clusters, *Astrophys. J.*, *880*, 145, doi:10.3847/1538-4357/ab2b34.

Zwicky, F. (1933), Die Rotverschiebung von extragalaktischen Nebeln, *Helv. Phys. Acta*, *6*, 110–127, doi:10.1007/s10714-008-0707-4, [Gen. Rel. Grav.41,207(2009)].